Ollscoil na hÉireann, Corcaigh

National University of Ireland, Cork

Smart Marine Sensing Systems for Integrated Multi-Trophic Aquaculture (IMTA)

Thesis presented by

Caroline Peres da Silva

ORCID 0000-0002-3403-8125

for the degree of

M.Eng.Sc. - Masters in Electrical and Electronic Engineering Science by Research

University College Cork

Tyndall National Institute

Head of School/Department: Dr. Jorge Oliveira

Supervisor(s): Dr. Brendan O'Flynn, M.Eng. Marco Belcastro

2021

TABLE OF CONTENTS

LIST OF TABLES

LIST OF ACRONYMS

ADC	Analog-Digital Converter
ADCP	Acoustic Doppler Current Profiler
AFE	Analog Front-End
AI	Artificial Intelligence
ASK	Amplitude Shift-Keying
BAP	Battery Assisted Power
BGA	Ball Grid Array
BW	Brackish Water
COTS	Commercial off-the-shelf
CPU	Central Processing Unit
CRC	Cyclic Redundancy Check
DC	Direct Current
DSP	Digital Signal Processing
DW	Distilled Water
EEPROM	Electrically erasable programmable read-only memory
EM	Electromagnetic
FDX	Full duplex
FFC	Flexible flat cable
FIFO	First-in first-out
FPC	Flexible printed circuit
FPS	Frames per second
FPU	Floating-point unit
FW	Freshwater
GPIO	General purpose input/output
HDX	Half duplex
HF	High-frequency

IC	Integrated circuit
IMS	IMPAQT monitoring system
IMTA	Integrated multi-trophic aquaculture
IMU	Inertial measurement unit
IP	Ingress protected
IR	Infrared
LDO	Low dropout
LF	Low-frequency
LFS	Low Force Stereolithography
LiDAR	Light detection and ranging
MCU	Microcontroller unit
MI	Magnetic induction
NFC	Near-Field Communication
PAR	Photosynthetically active radiation
PCB	Printed circuit board
PIT	Passive integrated transponder
PLA	Polylactic acid
PLL	Phase-locked loop
PUR	Polyurethane resin
PVC	Polyvinyl chloride
RAM	Random-access memory
RF	Radio-Frequency
RFID	Radio-Frequency Identification
RMSE	Root Mean Squared Error
RTC	Real-time clock
SDK	Software Development Kit
SMD	Surface-mount device
SONAR	Sound navigation and ranging

SPI	Serial peripheral interface
SW	Saline water
UART	Universal asynchronous receiver-transmitter
UAV	Unmanned aerial vehicle
UHF	Ultra-high frequency
USB	Universal serial bus
VNA	Vector network analyser
WRB	Wave-rider buoy

DECLARATION

I hereby declare that this thesis is my own work and certify to the best of my knowledge it contains no materials previously published or written by another person, or substantial proportions of material which have been accepted for the award of any other degree or diploma at University College Cork or any other educational institution, except where due acknowledgement is made in the thesis in accordance with the standard referencing practices. Any contribution made to the research by others, with whom I have worked directly at Tyndall National Institute – University College Cork or elsewhere, is explicitly acknowledged in the thesis. I also declare that the intellectual content of this thesis is the product of my own work, except to the extent that assistance from others in the project's design and conception or in style, presentation and linguistic expression is acknowledged.

I declare that this is a true copy of my thesis, including any final revisions, as approved by my thesis committee and the Graduate Studies office, and that this thesis has not been submitted to any other University or Institution.

Caroline Peres da Silva

ACKNOWLEDGEMENTS

Well, this has been a year. This thesis marks the end of three hard years – especially the last 18 months. Although challenging, I am grateful for all the experiences, good or bad and everything in between. These experiences will shape me, and I hope I can do everyone proud.

Firstly I would like to thank my supervisor Brendan O'Flynn for giving me this opportunity and for all the support he has given me during this time. Thank you, Brendan, for all your patience and the great advice you have given me. Thank you also for enabling me to achieve my dream of doing a Masters degree in another country.

The next thanks goes to my other supervisor, Marco Belcastro, for all the immense help he provided in both the hardware development and for the device design in general. Without your knowledge this would not be possible.

I would like to thank Masoud Emam and Hamed Jafarzadeh for their extensive support, for their help with firmware development, tests and deployment, and their immense patience and support. This really would not have been possible without you. I am eternally grateful.

I want to extend my thanks to all the WSN group in Tyndall for all the help, advice, and technical knowledge, in particular: Melusine Pigeon, Matteo Menolotto, Omid Talebi, Alessandra La Rocca, Sanjeev Kumar, Salvatore Tedesco, Nadeem Rather, Dinesh Gawade, and Sokratis Komaris.

My sincere thanks to the folks working in the IMPAQT project that have greatly helped me – in particular: Joanne Casserly, Kati Michalek, and Frank Kane.

I would also like to thank the funding agencies for the financial support. This work was carried out as part of the IMPAQT project. This project has received

funding from the European Union's Horizon 2020 research and innovation programme under grant agreement No. 774109. Aspects of this work were supported in part by Science Foundation Ireland (SFI) under Grant numbers 12/RC/2289-P2 (INSIGHT), 16/RC/3835 (VISTAMILK), 13/RC/2077 (CONNECT), and 16/RC/3918 (CONFIRM), which are co-funded under the European Regional Development Fund (ERDF).

To all the new friends I made in Tyndall that brightened my days with coffee breaks – Liudmila, Melusine, Alessandra, Luiza, Fernando, Marco Sica, Andrea R., Andrea F., Andrea B., Andrea P., Matteo, Sokratis, Davide, Pasqualino, Fabio, Jean, and many more – thank you!

To all my amazing friends that heard me complain, cry and laugh many times – the best housemates in the entire world Marinara and Larissa M., and my long long time friends Amanda, Larissa H., Isabella, Thais, Thiago, and Filipe – I am grateful from the bottom of my heart. Thanks for being close even if we are far away.

Last but not least, to my family – thank you all for the love and support all these years.

"So long, and thanks for all the fish!" –
Douglas Adams

ABSTRACT

Aquaculture farming faces challenges to increase production whilst maintaining sustainability by reducing environmental impact and ensuring efficient resource usage. One solution is to use an Integrated Multi-Trophic Aquaculture (IMTA) approach, where a variety of different species are grown in the same site, taking advantage of by-products (such as waste and uneaten food) from one species as inputs (fertilizer, food, and energy) for the growth of other species. However, the remote monitoring of environmental and biological conditions is crucial to understand how the species interact with each other and with the environment, and to optimise the IMTA production and management system.

Environmental monitoring of aquatic environments is already well supplied by commercial off-the-shelf sensors, but these sensors often measure only one parameter, which increases the power consumption and cost when monitoring multiple environmental variables with a fine-scale resolution. Current monitoring solutions for seaweed and kelp also include satellite and aerial sensing, which cover large areas effectively. However, these methods do not offer high-resolution, specific local data for growing sites, and are usually limited by turbidity and weather conditions.

Another limitation of available commercial systems is data recovery. Most of them require that the sensor be retrieved to download data directly, increasing cost of maintenance. Radio Frequency Identification (RFID) systems that transmit in the near field (Near Field Communication – NFC) are less attenuated by the seawater environment than higher-frequency communications, and thus potentially provide a more viable alternative for underwater data transmission.

In this work, we present a novel miniature low-power multi-sensor modality NFC-enabled data acquisition system to monitor a variety of farmed aquaculture species. This sensor system monitors temperature, light intensity, depth, and motion, logging the data collected internally. The sensor device can communicate with NFC-enabled readers (such as smartphones) to configure the sensors with custom sampling frequencies, communicate status, and to download data. It also has an internal machine learning enabled microcontroller, which can be used to perform data analysis internally. The device is designed to be attachable to seaweed and kelp blades or stipes.

The system designed was tested in lab to characterise its sensors and to determine its battery lifetime. The sensor device was then deployed in an IMTA farm in Bertraghboy Bay, Connemara, Ireland, with the help of the Marine Institute. The data collected from the device was then correlated with environmental sensors placed in the site.

Future work involves incorporating data analytics and machine learning algorithms to process data internally, allowing for lower transmission requirements.

1 INTRODUCTION

In aquaculture, maintaining the health and welfare of livestock, optimising resources, and ensuring sustainability aspects as regards the environment, are among the current challenges in the continued efforts to balance economics and environmental sustainability in the farming practices of the future.

One promising solution is to adopt the practice of Integrated Multi-Trophic Aquaculture (IMTA) where farmers cultivate different marine species in the same site, taking advantage of using by-products (such as waste and uneaten food) from one species as inputs (fertilizer, food, and energy) for the growth of other species (e.g., fish, molluscs, seaweed, etc.) co-existing on the same site. This is more sustainable than monocultures, due to its lower environmental impact, product diversification, spatial optimisation, and better management practices [1], [2]. However, to optimise the production and management system, and to understand how the species interact with each other and with their environment, technology to remotely monitor environmental and biological conditions is needed to provide IMTA owners to make informed decisions regarding their stock management.

A review of optical remote monitoring techniques for kelp done by Schroeder et al. [3] describes methods that are useful for determining biomass and temporal trends of kelp communities. These techniques involve image acquisition of an area to detect floating macroalgae as an indicator of plant biomass growth. Different species have different spectral responses to image sensors due to their different morphology and colour. The authors highlight the need for ground-truthing the data and the need for image processing algorithms that can be computationally expensive to assist in health diagnosis of the plant species. Another review of remote monitoring methods done by

Bennion et al. [4] also includes other techniques such as monitoring via LiDAR and SONAR.

The sensing techniques described in these papers are useful to monitor large areas for macro-algae distribution and to indirectly derive the biomass in the area. While it can cover large areas efficiently and can be used to estimate biomass, such solutions do not offer high-resolution data for growing sites, and are usually limited by turbidity and weather conditions [3], [4] .

In the context of IMTA, more detailed and fine resolution scale methods for species monitoring are needed. As the current challenge of IMTA is in understanding how the species interact with each other and the environment, ecosystem models such as Fan et al. [5] need to be designed and validated. To validate these models, environmental sensors – such as temperature, light, pH, water quality, nutrient (dissolved nitrogen) availability, and water motion – are needed.

Monitoring of water quality and environmental parameters in an IMTA/aquaculture setting is well supplied by commercial off-the-shelf sensors. Their measurement parameters include temperature, light radiation, and water quality (dissolved oxygen, pH, salinity, nitrogen). However, these sensors are expensive and usually are not co-located with the seaweed growth site, depending on wires and modes of deployment. Also, these sensors usually measure only one parameter, which increases the power consumption, maintenance and cost as multiple sensors are needed [6], [7].

Different abiotic and biotic factors affect the aquaculture farm production. In particular, wave exposure and water motion affect the growth of seaweed, but the effect is not completely understood [8]–[11]. Since most studies of this research topic use non-direct measurements of wave exposure, such as wave exposure index [12] derived by wind speed and incidence, they do not provide

good correlation with actual wave measurements being experienced by the seaweed [13]. It follows that there is a need for measurement of wave exposure and water motion rates from sensors such as Acoustic Doppler Current Profilers (ADCP) or water buoys. However, these sensors are bulky and expensive and do not allow for multiple point deployments. Some cheaper solutions were developed by various research groups using accelerometers [7], [13]–[16], but none of them provide a complete sensor integrated solution. In addition, wave sensors (such as wave-rider buoys) can be prohibitively expensive for some projects, which results in researchers and farm operators using computer modelling to estimate wave conditions that are not accurate [17].

Electronic tags can be used as attached sensors for marine species (Fish, seaweed bivalves etc.) that log behavioural, physiological and/or environmental data. They can store data internally and be later recovered or transmit data in real-time [18], [19]. The tag can be attached to a fish in different ways: externally attached, via gastric insertion, surgically implanted into the fish, or injected into the fish's body cavity if the tag is small enough (as is the case with PIT tags) [20]. For seaweed, the attachable sensor can be either attached to the seaweed itself on its blades or stipes, or on the support lines used in seaweed farms [21], [22]. For bivalves, attachable sensors are typically glued to the shell to monitor opening closing and other movement patterns which can be used to monitor the health and growth of shellfish [23].

Propagating signals from submerged sensor systems in water pose some challenges, especially in shallow water. Dissolved salts in water increase its conductivity, which causes strong attenuation in electromagnetic waves. This attenuation increases with the frequency of the signal, which limits radio communication to very low frequencies that require large antennas and have lower bandwidth [24]. Other issues such as multipath propagation and signal

fading also have an adverse impact on communications based on EM waves [24], [25]. Optical communication can achieve high data rates, but are also rapidly absorbed by water, and suffer scattering due to dissolved particles and interference from ambient light [25], [26]. Acoustic waves are commonly used as the physical transmission medium for underwater communications [25], [27]. However, they suffer absorption, refraction in deep water and reflections in shallow water. Water temperature gradients can change the speed of the signal, causing large propagation delays and reduce the communication efficiencies of this method. Multipath propagation and ambient noise interference are also problems for acoustic transmission [28].

RFID systems that transmit in the near-field are less affected by the seawater environment, and thus a more viable alternative for transmission of small packets of data [29]. Another benefit of these systems is the very low power required for transmission, as RFID tags harvest energy from the receiving signal sent by the reader. Although the transmission range is small for both near and far-field RFID (on the order of 10 to 20 cm), the power required for transmission on the tag is on the range of μA. These characteristics make RFID a great solution for data download in the field for marine applications. Near-field RFID based systems are currently used in the aquaculture setting for fish counting and identification through the use of PIT tags [20], [30], [31]. Although Near Field Communications are not affected by multipath propagation and reflections, its range and data transmission rate are small. To aid in this, embedded data analytics algorithms run on the electronic sensor tag could perform data analytics internally, only transmitting the results, making the amount of data to be transmitted smaller [32]–[34].

Far-field RFID systems, on the other hand, have better data transmission rates with a similar power consumption, but suffer from the same issues as EM

waves transmission: high attenuation due to water salinity, multipath propagation, and fading.

Current commercial electronic tags use different sensors, including accelerometers, to monitor fish [19], [31]. However, they usually transmit the average value for acceleration, with sampling frequencies that are too low to detect fast-start behaviour (such as feeding and escape) [35]. Most of them do not allow for customisation of sensor sampling frequency, nor provide raw data for data analytics – they usually only transmit or save mean values of acceleration which are not as useful as raw values [32], [36]–[38]. None of these commercial tags use RFID.

In this work, we present a novel integrated miniature low-power NFC-enabled data acquisition system to monitor IMTA species – hereafter called "Aquabit". This sensor system monitors temperature, light intensity, depth, and motion, logs the data internally, and can transmit the data wirelessly via NFC or through a wired USB connection. It also has an internal machine learning enabled microcontroller, which can be used to analyse data internally. This is the first time such a device has been reported in literature to the best knowledge of the author. During the literature review, no other device was identified with different sensor modalities integrated with NFC communication in a single miniaturised enclosure for marine applications.

The mechanical enclosure design allows it to be attached to either seaweed or other IMTA species commonly farmed in such settings. The primary design objective of the device is that it be attachable to seaweed and kelp blades or stipes: it has a texture on the bottom side for gluing onto the blades; it also has holes for threading safety threads to secure the device to the mooring line or to tie it to the stipe. Due to the small size, it can also potentially be externally attached to fish or molluscs to monitor their welfare.

The sensor device can communicate with NFC-enabled readers (such as smartphones) to configure the sensors with custom sampling frequencies, communicate status, and to download data. As the NFC communications protocol is designed for small packet size a wired USB connection is also designed in the system to transfer large amounts of data.

A waterproof enclosure for the multi modal sensing system was developed, and the device was characterised in lab experiments to verify if it complies with the requirements outlined above and to determine its battery lifetime with different sensor sampling conditions prior to deployment.

As an IMTA evaluation tool to develop the optimum growth parameters for seaweed growth, the sensor device was deployed in a working IMTA research demonstrator site as part of a longitudinal study: Lehanagh Pool (Bertraghboy Bay, Connemara, Ireland) with the help of the Marine Institute. The site is coastal, producing mainly Atlantic salmon (*Salmo salar*) and Brown seaweed (*Laminaria spp.*). The data collected from the Aquabit was correlated with environmental sensors placed in the site.

Future work involves incorporating data analytics and machine learning algorithms to process data internally, allowing for lower transmission requirements. The device also needs to be validated for other IMTA species of interest, as the deployment focus for this work was on seaweed. In future iterations of the design, additional wireless communication mechanisms will be included to enable high speed wireless transmission of data.

This thesis is organised as follows: chapter 2 reviews the current monitoring technology trends and sensors for aquaculture farms. It describes the relevant parameters which are useful to be measured in the IMTA deployments, and how the species grown can be remotely monitored to establish optimum

growth parameters. We also discuss what are the current monitoring technologies and the gaps in the state of the art.

Chapter 3 describes in detail the various underwater wireless transmission mechanisms investigated to establish a data communications path from the underwater sensors. In particular, the opportunities associated with a Radio Frequency Identification (RFID) data transmission system for underwater communications are investigated, as such RFID systems are currently in use in the aquaculture ecosystem. The theoretical model for path loss underwater is expanded to account for the salinity of the water and preliminary experimental measurements were done to examine the impact of the salinity of the water medium in the RFID transmissions.

In chapter 4, we present the requirements for the novel sensor device developed which are compiled from the literature and from end-users associated with IMTA research. The design process of the hardware, firmware and software are detailed, and each component of the system (NFC communications, sensor interface electronics, PCB, antenna, software flow, etc) is explained in detail.

Chapter 5 describes the laboratory characterisation of the device according to its specifications, and the deployment tests carried out to validate the device sensors, correlating the outputs with COTS sensors. The results of this analysis are shown in this chapter.

Chapter 6 concludes the thesis, summarizing the device design and the results of the tests and deployments. We also discuss improvements for the device, recommendations, and future work for the project.

Novelty Statement: this work presents the development of a novel integrated miniature low-power NFC-enabled data acquisition system to monitor IMTA

species. This is the first time such a device has been reported in literature to the best knowledge of the author. During the literature review, no other device was identified with different sensor modalities integrated with NFC communication in a single miniaturised enclosure for marine applications.

The key novelties identified and associated contribution to the state of the art described in this thesis are:

- Development of a novel marine sensor system that monitors temperature, light intensity, depth, and motion, logs the data internally, and can transmit the data via NFC. Its sensors parameters and sampling frequencies are configurable to enable custom deployments. It also has an internal machine learning enabled microcontroller, which can be used to analyse data internally.
- Mechanical design of a waterproof enclosure for attachment to seaweed blades or stipes.
- Analysis of underwater RF communication channel characteristics and the influence of seawater on the path loss for near-field RF and far-field RF.

Publications associated with this work include:

- Peres, C., Emam, M., Jafarzadeh, H., Belcastro, M. And O'Flynn B. (2021) 'Development of a low-power underwater NFC-enabled sensor device for seaweed monitoring', Sensors 2021, 21. https://doi.org/10.3390/s21144649
- Emam, M., Peres, C., Jafarzadeh, H., Belcastro, M., Casserly, J., Kane, F., and O'Flynn, B. (2021) 'Development of a low-power underwater NFC-enabled data acquisition for seaweed monitoring', Aquaculture Europe 2021.

- Peres, C., Pigeon, M., Rather, N., Gawade, D., Buckley, J., Jafarzadeh, H. and O'Flynn, B. (2020) 'Theoretical Models for Underwater RFID and the Impact of Water Salinity on the Design of Wireless Systems', International Journal on Advances in Networks and Services, 13 (34), pp. 45-59.
- Peres, C., Buckley, J., Rather, N. and O'Flynn, B. (2019) 'Theoretical Models for Underwater RFID', SENSORCOMM 2019: The Thirteenth International Conference on Sensor Technologies and Applications, Nice, France, 27-31 October, pp. 80-88.
- Peres, C., O'Flynn, B. (2019) 'Development of a low-power underwater RFID-enabled data acquisition system to classify fish behaviour', OCEANS 2019 MTS/IEEE Seattle, IEEE.
- Peres, C., O'Flynn, B. (2019) 'Development of a low-power underwater RFID-enabled data acquisition system to classify fish behaviour', Aquaculture Europe 2019.

2 LITERATURE REVIEW

2.1 INTRODUCTION

According to the Food and Agriculture Organisation (FAO) [39], the contribution from aquaculture to the total fish production has increased from 25.7% in 2000 to 46.0% in 2018. As of 2018, aquaculture accounts for 54.1% of total aquaculture and fisheries production, with seaweed production accounting for 55.2% of the total world production [40]. This rapid growth in the farming activity causes concerns over environmental sustainability when balanced against increasing production to meet growing demands and maintaining safety and profitability [41].

One promising solution is to adopt the practice of Integrated Multi-trophic Aquaculture (IMTA) [1], [2]. IMTA is an aquaculture farming method where the by-products of one aquatic species is used as resource (feed) for another species. In general, this is done by combining fed species (finfish, shrimp) with extractive species (seaweed and shellfish) on the same aquaculture site. This approach increases economic diversification, increases sustainability and reduces the environmental impact [1], [2]. However, IMTA has been tested only at a small scale in Europe. Even in regions where IMTA is already an established practice, the management of large-scale IMTA is difficult, due to the limited understanding of how the different species interact with each other and the impact of IMTA farming practices on the marine environment as a whole [42]. New approaches such as those being developed by the IMPAQT project [43] aim to progress this understanding and integrate into the IMTA model sensors and smart systems for monitoring, data modelling and intelligent management systems [44].

To aid in the aquaculture operations and management, environmental and biologic conditions of the farm need to be monitored. Environmental factors

such as temperature, solar radiation, pH, dissolved oxygen, chlorophyll, salinity, water movement and nutrient availability have great impact on the growth rate of species and production efficiency [6]. Biotic factors such as biomass, health and welfare of the species need to be monitored for normal farm operations. Direct observation of these variables is not always possible, and manual recording can be time-consuming and prone to errors.

Recent technological innovations such as the Internet of Things (IoT), new sensor technology and big data can supply aquaculture farms with the means to monitor and operate the farm remotely and automatically. It can also provide data to increase the farm sustainability and gather insight into the relationship between the cultivated species and the environment [41], [45]. Other key benefits of monitoring technology and IoT for aquaculture are the possibility of farm automation to reduce maintenance costs, early warning about problems, and modelling and prediction of farm indicators.

Improvements in monitoring tools, and the provision of low cost, efficient, robust monitoring devices will improve aquaculture production methodologies providing better understanding of the resilience of crops and facilitate improvements in best-practise on the farms, and on the sustainability of the sector [6], [45]. Enabling the efficient farming of seaweeds and other lower-trophic aquaculture products will promote the efficient use of the available marine space, improve productivity, provide high quality, nutritional food products and products to support other industries, ensure the welfare of the products and, and enable efficient use of sites to increase productivity [2], [6], [40]. Seaweed farming is in its infancy and the development of the industry needs low cost, effective technologies, and information to enable it to prosper. The potential to use seaweeds as alternatives in animal feeds is being explored, including its ability to cut methane emissions from cattle by inclusion of seaweeds in their diets [46]. The

farming of seaweeds offers significant potential as a tool to mitigate the effects of climate change [47]. As seaweed absorbs carbon at a similar or higher rate to land plants but are a significantly faster growing crop, this gives them potential as rapid and effective tools to provide carbon sinks and to remove carbon from the system [47]. Seaweed can also contribute to food security by providing nutritional food sources from a product that can be produced in a sustainable and scalable way [40].

2.2 THE STRATEGIC IMPORTANCE OF SEAWEED AND IMTA

Ireland is one of the top seaweed producers in Europe, primarily supported by a strong tradition of seaweed harvesting [48]. The world production of aquatic plants (mostly seaweeds) reached 33.3 million tonnes in 2018 [39]. In Ireland in 2020, 80,600 tonnes of seaweed worth €31 million were exported and 64,700 tonnes (worth €10 million) were imported for reprocessing and export markets [49]. Seaweed is increasingly used as a resource for food, bio fertilizer, feed, bioenergy production, chemicals, and the pharmaceutical industry [6], [50]. Coupled with changes in consumer attitudes to natural foods and ingredients, production is expected to further increase.

Sites can be located in a variety of locations and environments from sheltered coastal areas to offshore multi use platforms [6]. Key to determining suitable locations for macroalgae culture is:

a) understanding of the growing environment and

b) understanding the conditions the macroalgae may be exposed to.

The collection of data monitoring hydrodynamics and abiotic conditions combined with crop yield and crop quality throughout the growing cycle will help to maximize yields, best use of space, site selection and orientation, species selection, planting time and harvest dates [51].

As the demand for seaweed increases the natural populations become inadequate to meet requirements and harvesting natural stocks becomes less sustainable [6]. This is reflected by the fact that current global seaweed harvest consists mainly of farmed aquaculture seaweed instead of wild harvest [39], [40]. Efforts are being made to increase production by farming using different and novel techniques. To do this effectively detailed knowledge of the biology and lifecycle of the plants, of the environment that they grow in, and the interactions between the two, is required. Monitoring of the environment, the interaction of species within the environment and the understanding of how external factors affect performance and welfare are important to and improve production technologies, and to optimise production [51]–[53].

The EU Blue Growth strategy encourages the use of biotechnology to unlock high-value compounds from marine bioresources. Blue Growth, Common Fisheries Policy (CFP) and the European Maritime and Fisheries Fund (EMFF) Operational Programme stress the importance of safeguarding biodiversity and protecting the marine environment in cultivating marine bioresources. Integrated Multi-Trophic Aquaculture (IMTA), particularly seaweed production supports these aims.

As discussed in the previous section, IMTA is an aquaculture farming method where multiple species are grown in the same site, using the by-products of one species as resource (feed) for another species [1]. The main driver behind this technique is that traditional fish aquaculture methods create a lot of nitrogen-derived waste that is discharged into the environment [54]. To reduce the possible harm to the environment and diversify production, this nitrogen-based waste can be used as nutrients for seaweed growth [55]. Thus the seaweeds become a biofilter that restores water quality. This approach increases economic diversification, sustainability and reduces the environmental impact [1], [2]. Therefore, IMTA and seaweed aquaculture

support the UN sustainable development goals of responsible consumption and production, ensuring careful management of resources.

However, IMTA has been tested only in small scale in Europe. Even in regions where it is already an established practice, the management of large-scale IMTA is difficult, due to the limited knowledge of how the different species interact with each other and the impact on the environment as a whole [42]. Researchers and farm managers have increasingly created and used modelling techniques to assess or predict farm performance and species interaction [56]. These models range from simple empirical observations to complex growth and energy budget models. The common factor of all these is the need for observed data to create or validate such models.

2.3 ENVIRONMENTAL PARAMETERS AND SEAWEED CULTIVATION

Different abiotic and biotic factors affect the aquaculture farm production, and therefore are parameters of importance to be monitored. For seaweed, environmental factors such as temperature, solar radiation, pH, dissolved oxygen, chlorophyll, salinity, water movement and nutrient availability have great impact on the growth rate, harvested biomass and production efficiency of seaweed farms [51], [53]. The primary method for measuring quantity of harvest is the biomass – the total weight of the produced seaweed on site.

According to Kerrison et al. [51], there are ideal cultivation environmental conditions for each seaweed species. One such condition is the water temperature which has a direct effect on the metabolic rate of seaweeds and on their reproducibility. A temperature rise of a few degrees above the optimum could lead to reduced growth rate, fragmentation, or death.

The depth of growth is also meaningful as it affects the water temperature and the amount of light radiation that arrives to the seaweed surface. For photosynthesis to happen in the seaweed, it needs to receive

photosynthetically active radiation (PAR) from light. PAR is the spectral range of light radiation with wavelengths between 400 and 700 nm that photosynthetic organisms use for photosynthesis [57]. The amount of PAR absorbed needs to be delicately balanced to achieve maximum biomass: too much light absorbed can inhibit photosynthesis and lead to cell damage or death; too little light inhibits growth [51].

Water salinity is another important factor that affects the osmotic pressure balance in seaweeds. The concentration of some types of carbohydrates inside the seaweed is dependent on the environmental water salinity [51]. Water quality, including the concentration of essential nutrients for seaweed (such as nitrites), dissolved CO2, pH, are also of great importance. For example, a water pH level outside of the 8 – 8.5 range can lead to reduced growth or tissue damage.

Water motion and flow rate considerably affect seaweed growth rates. Low levels of water motion limit the supply of nutrients and CO2 which the seaweed absorbs, limiting growth. However, high movement rates can cause dislodgement of kelps and reduced productivity by forcing the plant to develop larger holdfasts [51]. Visch et al. [9] found that the growth of *Saccharina latissima* decreases with more wave exposure. A study by Kregting et al. [10] concluded, however, that for *Laminaria digitata* the growth rates were lower for both the more wave-exposed and the less wave-exposed areas, indicating that an optimum point exists. Bekkby et al. [11] found that the morphology of the kelp is changed depending on wave and current conditions, in which a high water flow increases strength related morphological attributes.

However, a common characteristic of these studies is that the wave exposure and water motion rates are not directly measured with wave sensors, such as

Acoustic Doppler Current Profilers (ADCP), wave buoys, or other related sensors. The method usually employed is to use wind speed and incidence, and distance to coastline to calculate the wave exposure index [12], and then classify large geographical locations as "high exposure" or "low exposure". Lindegarth and Gamfeldt [17] argue that using this categorical variable method instead of a continuous-type variable leads to very different interpretations of the importance of environmental factors.

Hurd [8] agrees with this conclusion, by explaining that the current understanding of how water motion affects macroalgae growth is based on experiments that verify water motion indirectly. Thus, the understanding of "higher rates of production in moderately wave-exposed environments" is hard to verify. They also argue that another difficulty in correlating water motion and macroalgal production comes from the fact that it is unknown which specific facet of water motion (mean velocities, flow, drag forces and mechanical stress) is causing the effect. They highlight that the influence from other environmental factors need to be measured and accounted for a complete understanding of how water motion affects growth.

Further, Focht and Shima [13] found that the correspondence between a priori assessments of wave exposure and in situ acceleration measurements done by accelerometers and a wave-rider buoy is limited.

All the parameters mentioned are of great importance for farm productivity. Multiple models of growth and biomass created with environmental data, such as the model by Broch and Slagstad [53] which utilises water temperature, speed, PAR, nitrogen and carbon reserves and nutrient concentration to predict growth and biomass. Reid et al. [56] review various models for IMTA farms created from environmental parameters observation. These models are of critical importance when selecting an appropriate site,

operating the farm, and making sure the production is as efficient and environment-friendly as possible.

2.4 REMOTE MONITORING AND SENSOR TELEMETRY IN AQUACULTURE

For all these environmental and biological parameters explored previously, direct observation is challenging due to the great time and personnel cost to manually sample and collect data on the farm. Further, if the farm site is in a hard-to-reach location, manual monitoring might not be possible. A possible solution is to remotely monitor the environment using sensors deployed on site or remotely that communicate back to the farm operators [6], [45].

Monitoring of water quality and environmental parameters in an aquaculture setting is well supplied by commercial off-the-shelf sensors. Their measurement parameters include temperature, light radiation, and water quality (dissolved oxygen, pH, salinity, nitrogen). However, these sensors are expensive and usually not co-located with the seaweed growth site.

Bennion et al. (2019) [4] and Schroeder et al. (2019) [3] carried out a review of optical remote monitoring techniques for kelp that are useful for determining biomass and temporal trends of kelp communities. These techniques involve image acquisition of an area to detect floating macroalgae, and different species have different spectral responses to image sensors due to their different morphology and colour. The authors highlight the need for ground-truthing the data and image processing algorithms that can be computationally expensive. Satellite multispectral imagers achieve a high spatial coverage and cover multiple spectra, which is useful to identify the different species and submerged vegetation. It is cost effective due to the large availability of open-source images. However, these images are negatively affected by atmospheric conditions and water turbidity [4]. However, the

spatial resolution of these techniques is limited, as an aquaculture site can be covered by just a few pixels in the image [58].

Aerial images collected by aircrafts (planes, UAVs, and drones) can also cover multiple spectra, and the images are in a finer resolution than satellite images. By adding other sensors in the aircraft, it is possible to associate the image with environmental data. Nonetheless, gathering the data can be time consuming and expensive. The recent drone technology evolution is, however, decreasing costs [4].

Underwater imagery, gathered by Autonomous Underwater Vehicles, ships and divers, are useful to collect high-resolution images of the seafloor and the underwater habitats. The spatial scale covered is small in comparison to aerial and satellite images, however the resolution is bigger. On the other hand, this technique is very time consuming and expensive, and it is also negatively affected by water turbidity. In addition to that, converting images into quantitative data is slow and difficult, requiring expert knowledge [3], [4].

Another technique to remotely monitor macroalgae is LiDAR, using a pulsed laser and measure the time and wavelength of the reflections of the laser light. This can be used then to create environmental layers to detect and classify the underwater vegetation. It can cover large areas quickly, with different wavelengths, generating a quantitative information. However, temperature, tides, and turbidity negatively affect the results, and LiDAR is restricted in temperate regions due to that [4].

In a similar technique, Sonar uses sound and its backscatter to create a 3D visualisation of the seafloor and the underwater environmental layers. The advantage over LiDAR is that sound can travel much further underwater, and thus a multibeam sonar can cover large areas. However, the data processing is also labour intensive and time consuming, also requiring large storage of

data. Another drawback is that sonar is ineffective in shallow waters due to the reflection and refraction of the sound wave when interacting with the seafloor and the sea-air layer [4].

All the sensing techniques outlined above are useful to monitor large areas for macroalgae distribution and indirectly derive the biomass in the area. However, in the context of IMTA, more detailed and fine resolution scale methods are needed. Ottinger, Clauss and Kuenzer [58] argue that very high resolution sensors are better suited for aquaculture site mapping and monitoring. Another potential issue with these optical remote monitoring techniques is the over or underestimation of the monitored variables. For example, Meneghesso et al. [59] identified a mismatch between the remote monitoring and deployed in-situ temperature loggers. Other studies from Woo and Park [60] and Brewin et al. [61] found the same problem. This highlights the need for an in-situ deployed sensor to accurately monitor variables such as temperature.

As the current challenge of IMTA is understanding how the species interact with each other and the environment, ecosystem models such as Fan et al. 2020 [5] need to be designed and validated. To validate these models, environmental sensors – such as temperature, light, pH, water quality, nutrient (dissolved nitrogen) availability, and water motion – need to be deployed to measure small-scale areas and variations.

2.5 MERGING IOT AND AQUACULTURE

As O'Donncha and Grant [45] argue, there are great production benefits in the use of in situ sensors to sample environmental variables, integrating the aquaculture farms into the Internet of Things (IoT). The data collected by multiple sensors in the farm that continuously and remotely monitor

environmental parameters can be aggregated and used to create AI-driven, predictive models.

Monitoring of water quality and some environmental parameters – such as temperature – in an aquaculture setting is well supplied by commercial off-the-shelf sensors, such as LI-COR light sensors, HOBO temperature loggers, etc [62], [63]. Common measurement parameters include temperature, light radiation, and water characteristics (dissolved oxygen, pH, salinity, nitrogen concentration). However, these sensors are expensive and usually not co-located with the seaweed growth site. Also, these sensors are usually big, require cables and a power supply, and measure only one parameter, which increases the power consumption, maintenance and cost [6], [7]. For example, Visch, Nylund and Pavia [9] used Onset HOBO Pendant UA-002-64 loggers [63] to monitor and log temperature. However, this commercial sensor is big, only measures temperature and light, and needs to be wired which limits the deployment in areas where the accessibility is hard or there is no power.

Added to that is the problem that most of these sensors are wired – cannot wirelessly transmit data – which makes them harder to deploy.

Judge, Choi and Helmut [64] review the current logger technology for intertidal environments. Although not the same application, the environment is similar to the one seaweed is cultivated and the loggers used to monitor are the same. They argue that the current loggers available are limited in: (1) construction – as the attachment requires large amounts of epoxy that interfere with temperature readings; (2) lack of real -time data due to the wireless communications constraints of underwater environments and hard to download data; and (3) miniaturization. The dataloggers used in the studies compiled by Judge, Choi and Helmut [64] are: (a) iButton devices by Maxim Integrated [65] that, although developed for harsh marine environment,

require a cable to transmit data to a receptor; and (b) HOBO TidbiT by Onset [66] that is small and waterproof. Both solutions, however, only log temperature.

Other sensors to monitor aquaculture species were developed using easy-to-use platforms such as Arduino [67], [68]. The device developed by Beddows and Mallon [68] is able to log only temperature with an operational lifetime of up to 1 year in non-rechargeable batteries. The device is housed in a big enclosure that is able to withstand the harsh marine environment. The data collected needs to be downloaded by recovering the device.

In the case of water motion, commercial sensors generally used are wave rider buoys and ADCPs, which are accurate and can generate long term datasets, but are expensive. Low cost devices such as dynamometers, clod cards and slow-dissolving plaster standards are commonly used, but they are limited to a single point of measurement, and can have variability in results due to manufacturing, water temperature, and salinity [7]. Due to this, multiple studies use wave exposure index [12] or similar mathematical models that aggregate data from wind and tides to get broad-scale predictions about the water movement. However, these models do not provide fine scale information, and uncertainties in the input data can result in inaccuracies in the model and incomplete models [13].

Various authors, such as Evans and Abdo [7], Focht and Shima [13], and Lyman et al. [14] present solutions to the problem of finely determining water motion by using inexpensive sensors developed with common materials. Lyman et al. [14] developed an inexpensive open-source pressure transducer to log wave height using a PVC pipe as housing. Focht and Shima in [13] used accelerometers to measure fine-scale wave exposure in different locations, compared with a nearby deployed wave rider buoy. Their analysis indicates

that there was a significant fine-scale variation in the wave movement, due to changes in acceleration, timing, and frequency of wave events. They argue that a priori assessment of wave exposure (such as wave exposure index) have limited correspondence with water motion.

The study by Evans and Abdo in [7] uses a HOBO Pendant G acceleration data logger attached to a structure designed by them, moored to the seafloor, and deployed adjacent to a wave rider buoy. They correlated the wave motion data collected by the accelerometer with the daily average and maximum WRB (wave-rider buoy) and tidal data and found it to be significantly correlated with daily average total wave height. The authors argue that higher accelerometer sampling rates (with increased data storage) would enable researchers to measure and determine more detailed water movement parameters, such as velocities, forces, and wave periods. It would also allow a more detailed analysis of the data using spectral analysis. They conclude that, while the solution developed does not replace a more advanced device, it allows researchers to gather additional water movement where more advanced devices are not available or too costly.

The authors Stevens, Hurd and Smith in [21] attached a data logger package consisting of an accelerometer, and displacement and force transducers to seaweed blade and stipe. The objective of the investigation was to study the hydrodynamics of kelp, estimating forces and bending moments due to wave motion. To estimate the wave field, they used video, pressure sensors and resistance wave gauges. The study in [69] was also interested in analysing the hydrodynamics of macroalgae. They used a force transducer at the attachment point between the seabed and the seaweed.

Another study by Mullarney and Pilditch [22] attached the accelerometer logger directly to the kelp stipe by tying HOBO Pendant G Accelerometers at

fixed intervals up the stipe bundle [22]. Pressure and water velocities were measured by an ADCP for this study. The objective was to determine the response of the kelp regarding the wave movement.

For wave measurement, Knight et al. [67] developed an IoT-enabled tide gauge with a pressure sensor and an Arduino. This sensor is designed to be placed in a fixed position and requires cables to a power source. Kennedy et al. [15] developed a miniature wave measurement device as a replacement for wave buoys. It has a 6 Degree of Freedom (DoF) Inertial Measurement Unit (IMU) and a Zigbee wireless connection.

2.6 DATA RECOVERY AND TRANSMISSION

All the monitoring methods discussed previously require data to be collected and stored inside the sensor device or transmitted to a receiver that stores the data. In general, stationary sensors, such as environmental sensors, underwater cameras, and acoustic sensors, are placed in a predetermined locale and wired to a data aggregator. Bigger devices such as wave rider buoys can also have on-board memory card for storing data to be collected later [70].

In general, devices that monitor parameters in real time need to transmit the data collected to a receiver. The devices that are moored or fixed to a location can be wired to a data aggregator, however, some wired sensors are not confined to a single location, but can be attached to biological systems that have movement, such as the study by Mullarney and Pilditch (2017) [22], where they attached wired acceleration loggers to seaweed. In these cases, the wires can interfere with the movement measurements. Ideally, the sensors that are attached to individuals or free to move in space need to transmit data wirelessly. Wireless underwater communication is usually done via acoustic, electromagnetic (radiofrequency), or optical transmissions [25].

Acoustic transmission is based on pressure waves that propagate omni-directionally through water, but not air. Therefore, the receiver (called hydrophone) must be submerged. This method is more demanding than radio transmission due to the bigger energy requirement. It is suitable for deep water environments, but is ineffective in shallow or turbulent water, and can suffer from noise interference (rain, boats, etc.) [28]. The range of reception depends on the size of the transmitter, as lower transmission frequencies that result in greater range require an acoustic piezoelectric emitter with larger diameter. The attenuation to the acoustic waves is low, but the speed of transmission is also low as it is the speed of sound underwater (approximately 1480 m/s). This can cause multiple problems in the transmission, such as high multipath (the phenomenon where multiple signals from the same source are received by the same antenna at different times) due to the reflection and refraction of the transmission waves and high propagation delay due to the slow speed of the carrier [25]. Other problems are also caused by the water temperature gradients that change the speed of the sound [71].

Radio signals propagate omni-directionally in water and in air, but only wave vectors at a certain orientation can cross the air-water interface to emerge into the air to be detected by a receiving antenna in free space. The signal detection range decreases with increasing water depth and water conductivity (determined by its salinity) [25], [71]. Therefore, freshwater and seawater environments must be analysed separately. For both cases, the absorption is greater for higher frequencies, which limits the transmission frequency for the system, and therefore the bandwidth. Another problem in electromagnetic transmission in seawater is that the electric conductivity is also dependent on the frequency of the wave. For example, at 10 kHz the conductivity is 4.3 S/m, while at 10 MHz the conductivity is 5.4 S/m [71]. Low frequency signals have less attenuation with increasing depth and water conductivity but require

large antennas. Higher frequency signals demand more transmission power to reach the same range as lower frequency systems, which translates into a bigger battery and associated system size. The conclusion is that radio transmissions are suitable underwater for short-range communication with lower frequencies than the commonly used frequencies for air transmissions [24].

A potential alternative communications mechanism is to use optical waves to transmit data wirelessly underwater. They can achieve high data rates but are also rapidly absorbed by water. Added to that, the optical signal is significantly scattered due to the presence of dissolved particles in the water [26].

Another promising alternative is to use magnetic induction (MI) to transmit the data, the same principle that Near-Field Communication (NFC) and low-frequency RFID devices utilize, as it is not affected by multipath propagation and fading [72]. MI communications systems rely on the transmitter (also called reader) generating an electromagnetic field from its loop antenna, that induces a voltage in the coupled circuit (the receiver or tag) inside this field (another loop antenna). The system then works like two coupled inductors, and a change in current in one side induces a change in voltage in the other side [73], which is how the data is transmitted. An added benefit of this system is that the induced voltage in the tag can be rectified and used to power up the tag, effectively harvesting energy from the field. This is the same working principle of the PIT tags that are used in aquaculture and fisheries production and research [20].

2.7 CONCLUSION

All the solutions discussed previously in this chapter have similar issues in common, with varying degrees: big size that limits the deployment method;

power requirements such as cables, non-rechargeable batteries, external power supplies; data recovery, as most do not transmit data wirelessly (requiring cable loggers that store data for transmission) or limit deployment in hard-to-reach locations as the device recovery is challenging; devices limited to one sensor type per enclosure – **based on the literature review carried out, to date no miniaturised multi sensor modality solution for seaweed monitoring has been reported.**

From the literature review presented in this chapter, a list of specifications for the sensor device was compiled and is as follows:

- The device should be able to measure in-situ multiple different environmental variables, so that they can enable fine-scale resolution monitoring of the status of the farm. The main parameters that affect seaweed growth were identified from the literature [51] and are: temperature, depth, light intensity, and wave motion.
- The device must be as small as possible as to not disturb the seaweed physiology; be reusable to reduce environmental waste and pollution; waterproof and resistant to the marine environment.
- The sensors should be configurable regarding sampling frequency and other relevant parameters to allow greater customisation in the deployment.
- The device should be able to communicate wirelessly underwater to transmit the logged data. It also needs to log the raw data collected internally to be downloaded later.

The development of a novel low-power consumption, miniaturised data acquisition systems, supported by efficient novel underwater communication technologies, offer the potential for smaller producers and farmers to monitor their environment and their farmed stock in ways that are beyond their current

budgets and capabilities. This can facilitate a better understanding of their operations and improve their ability to be more efficient and effective in their farming practises. These technologies offer advantages to help progress seaweed cultivation but also have significant potential with other species and aquaculture situations, and indeed in the broader marine sector where a deeper understanding of the micro-environment is critical to operations.

To this effect, we developed a novel miniature low-power Near Field Communication (NFC) enabled data acquisition system to monitor aquaculture species. This sensor system monitors temperature, light intensity, depth, and motion, logs the data internally, and can transmit the logged data via NFC (to a smartphone, for example). The NFC communications system can also be used for system setup at deployment stage using a Smartphone application to configure and turn on the device. The system also has an internal machine learning enabled microcontroller, which can be used to analyse data internally.

The waterproof mechanical enclosure design which was developed allows it to be attached to IMTA species for data acquisition. The device is designed to be attachable to seaweed and kelp blades or stipes: it has a texture on the bottom side for gluing onto the blades; it also has holes for threading safety threads to secure the device to the mooring line or to tie it to the stipe. The temperature and depth sensor has a direct interface with water, which allows the sensor to accurately measure water temperature even with glue or epoxy attachments. The waterproof enclosure for the multi-modal sensing system was characterised in experiments to verify if it complies with the requirements outlined above and the sensing system was characterised in lab experiments prior to deployment to determine its battery lifetime with different sensor sampling conditions and to verify sensing accuracy.

3 THEORETICAL MODELS FOR UNDERWATER RFID AND THE IMPACT OF WATER SALINITY ON THE DESIGN OF WIRELESS SYSTEMS

This chapter is a slightly modified version of "Peres, C., Pigeon, M., Rather, N., Gawade, D., Buckley, J., Jafarzadeh, H. and O'Flynn, B. (2020) 'Theoretical Models for Underwater RFID and the Impact of Water Salinity on the Design of Wireless Systems', International Journal on Advances in Networks and Services, 13 (34), pp. 45-59."

One of the requirements for the Aquabit sensor device is to be able to wirelessly transmit data underwater. As discussed in section 2.6, we have identified RFID technology as a potential solution to short-range underwater communications in marine farm environments. Although the transmission range is small for both near and far-field RFID (on the order of 10 to 20 cm), the power required for transmission on the tag is on the range of μA. These characteristics make RFID a great solution for data download in the field for marine applications. However, little is known about the effect of sea water in RFID communications.

This chapter presents an exploration of the effect of water salinity on wireless communications underwater, in particular RFID systems, both in the near and far-field. We aim to understand and better predict the applicability, power budget, and transmission range of RFID systems for an underwater sensor tag.

By understanding the underlying physics of the transmission channel, our objective is to better design the system to the defined application. Design parameters for the RFID transmission system, such as operating frequency, antenna size and impedance, number of coil turns, and power delivered to the antenna, are dependent on the channel parameters and desired range of transmission.

In this chapter, we confirm that lower frequency systems indeed suffer less attenuation in marine underwater settings, and this informs the initial decision in Chapter 4 of using 134.3 kHz for the operating frequency of the system, as it suffers less attenuation and is the frequency used in PIT tag systems.

3.1 INTRODUCTION

Underwater wireless communications present some challenges due to the characteristics of the channel medium. The underwater environment has different characteristics and phenomena compared to those typical for terrestrial radio propagation channel [25]. Despite these difficulties, underwater wireless communications are needed for a variety of underwater systems. Practical applications include seismic activity monitoring, equipment monitoring and control, underwater wireless sensor networks, underwater robots and Underwater Autonomous Vehicles (UAVs), aquaculture, fish stock management and underwater environmental monitoring [27], [74].

There are three commonly used technologies for underwater communications [24]–[26]. Radio-frequency (RF) communication consists of propagating electromagnetic waves, and it has high data rates but suffers from multipath propagation, strong attenuation and Doppler effect [25], which greatly limit the transmission range. Due to the increasing attenuation for higher frequencies, it requires that systems operate at lower frequencies to achieve longer ranges of transmission, which in turn demands the use of large antennas making it unsuitable for some miniaturised applications. Acoustic communication makes use of propagating sound waves, which have low attenuation underwater, achieving the longest range [25]. However, this type of communication exhibits a large propagation delay due to the speed of sound underwater, suffers from multipath propagation, and is affected by a large delay spread that leads to inter-symbol interference [28]. Temperature

gradients and ambient noise are also problems for acoustic communications. Another technology that can be used for underwater use is optical communication, which uses electromagnetic waves in the visible spectrum to transmit data. Such technologies have large data rates with low propagation delay. However, they suffer significant absorption in water and strong backscatter due to turbidity (e.g., suspended particles in the medium) [25].

Underwater Radio-Frequency Identification (RFID) is not an extensively explored topic due to the problems outlined above for underwater RF communications, specifically strong attenuation, and multipath propagation [24]. However, some RFID systems communicate via Magnetic Induction (MI), which could provide an alternative for the existing technologies [27], [75]. In this chapter, we want to explore the potential for such technology to be used in the marine environment. We examine the different methods of communication that different RFID systems employ, separating them into two categories: namely, near-field communication and far-field communication. Theoretical mathematical models exist for terrestrial RFID systems, from which the system functionality, communication properties and link budget can be derived. This chapter aims to derive similar models for underwater RFID communications, by describing the underwater channel physical properties for near-field and far-field electromagnetic fields by presenting the path loss for each. This can then be used to predict communication range, link budget and channel capacity.

This chapter is organised as follows. Section 3.2 discusses the related work. In Section 3.3, we give a brief overview of an RFID system and its components. Section 3.4 then presents the model for underwater RFID for near-field and far-field communications. In Section 3.4.1, we present preliminary results of measurements done of magnetic field strength in various water solutions of

different salinity values. Section 3.4.2 discusses underwater RFID in light of the theory presented and the measurement results. We conclude the chapter in Section 3.5.

3.2 RELATED WORK

Underwater RFID is not a common topic of marine research due to the challenges that the underwater environment poses to RF communications described in section 3.1. However, some preliminary work has been done. For example, Pozzebon in [76] explores the use of Near-Field Communication (NFC) underwater. Using smartphones and smart cards operating at 13.56 MHz, the authors tested the read range achieved and the influence of dissolved salts in water in the read range. Another group led by Bertoni used Low-Frequency (LF) RFID to track the sediment movements in a beach as described in [77]. Here, RFID transponders were coupled to pebbles, creating "smart" pebbles that could be detected at up to 50 cm underwater. They were then released into the beach and tracked to map the movement of sediment. Systems that use LF RFID underwater can also typically be found in Passive Integrated Transponder (PIT) tags used to uniquely identify fish in fisheries and research [19], [31].

The authors in [29] summarised the current understanding of underwater RFID, examining the penetration depth in freshwater and seawater. However, the model presented is simplified and accounts only for the far-field operation. They also showcase other uses of RFID underwater, such as underwater pipeline monitoring. In addition, other authors such as Akyildiz in [78], have explored MI communications underwater using inductive coupling and provide an overview of the current research findings and challenges for MI. Models for MI in lossy environments (such as underwater and underground) and air environments can be found in [72], [79]–[82].

3.3 RFID SYSTEM

A typical sensor RFID system is comprised of a tag (transponder) and a reader (initiator). The tag is used to identify or measure ambient parameters, typically temperature for instance [83]. Furthermore, a reader is used to read and write data from or into a tag located within its proximity or vicinity. The tag consists of a coupling or backscatter element such as a conductor loop or an antenna, and an RFID radio that stores the sensed data or ultra-low-power embedded system to measure various ambient parameters and store relevant metadata. The reader also comprises similar antennas as a coupling element along with a control unit and an RFID radio. Generally, near-field RFID uses inductive coupling between the reader and tag loop antennas to communicate with each other when located within each other's proximity or vicinity. RFID operates at 120–135 kHz low frequency (LF) unregulated band and high frequency (HF) 13.56 MHz Industrial, Scientific, and Medical (ISM) band. LF RFID follows the ISO/IEC 18000-2 standard [84] and HF RFID follows ISO/IEC 18000-3 standard [85] along with additional smart cards ISO/IEC 15693 [86], ISO/IEC 14443A and 14443B standard [87]. Additional NFC standards such as the NFC Forum [88] ensure the interoperability of NFC-enabled devices and enable communication between them. The NFC standard defines the data rate (26.48 to 424 kbit/s), data frame formats such as NFC Data Exchange Format (NDEF), modulation, initialization, and collision control during initialization [89].

In Figure 1 the block diagram of a typical RFID sensing system is shown. The conductor loop antenna of the reader generates the magnetic alternating field. The magnetic flux (Φ) generated by the reader loop antenna is used as a power supply for the sensor tag. This is achieved by utilising the voltage which is induced in the tag antenna by mutual inductance (M) between the transmitter and receiver antenna. Due to this induced voltage, a current starts flowing in the tag antenna and its value can be theoretically calculated from the quotient

of the voltage divided by the impedance of the tag antenna [73]. Furthermore, the NFC radio Analog Front End (AFE) consists of an RF interface and the energy harvesting circuitry, which connects to the loop antenna. The harvested voltage is further regulated using a low dropout regulator and is used to power up an ultra-low-power Microcontroller Unit (MCU), as well as a sensor [73]. The NFC radio consists of an Amplitude Shift Keying (ASK) demodulator which demodulates the messages from the reader and responds to the reader with the help of load modulation. The load modulation is achieved by varying the impedance of the tag antenna [73]. The NFC radio and sensor is interfaced with MCU using the Inter-Integrated Circuit (I2C) Protocol. On power up, the sensor starts sensing a parameter and its raw value is transmitted to the MCU through the I2C connection from the sensor to the MCU. The MCU then generates an NDEF message with the sensed value and forwards it to the NFC radio [83], [90].

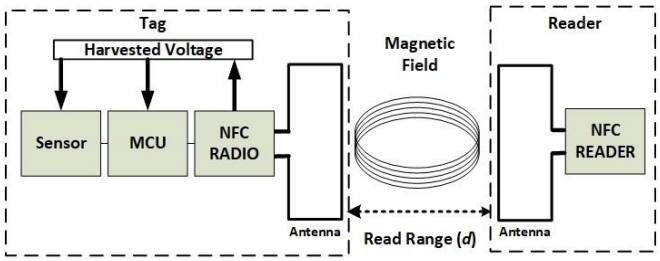

Figure 1 - Block diagram of a RFID sensing system.

The tag receives the signal via the coupling element and utilises the induced voltage to power up the tag's RFID radio and other electronics. The RFID radio then sends data back to the reader via load modulation or backscatter. In general, such a tag is battery-less, and it is powered by the Magnetic flux (Φ) generated by the reader. Other battery assisted power (BAP) system models exist incorporating an active RFID device that consist of a battery as a power source. The added battery is used to power up additional tag electronics or

sensors and can also be used to extend the communication distance range between the transmitter and receiver.

Equation 1 shows the relationship between the quality factor of the antenna *Q*, the bandwidth (*BW*) and the resonant frequency (*f*) for the system. For example, larger bandwidth is required to cover the sidebands of communication for the ISO/IEC 14443B standard and is particularly important to have if using higher data rates such as 424 or 848 kbps. In addition, for other applications based on the ISO/IEC15693 standard, the Q factor can be significantly higher, as the sidebands do not need such a wide bandwidth [91].

$$Q = f / BW \tag{1}$$

3.4 RFID CHANNEL PHYSICAL CHARACTERISTICS

The antenna or coil of the RFID reader generates an electromagnetic field. These fields can be described as time-harmonic fields in a lossy medium and are described in Equations 2 and 3 below [92]:

$$\nabla^2 \boldsymbol{E} = \gamma \boldsymbol{E} \tag{2}$$

$$\nabla^2 \boldsymbol{H} = \gamma \boldsymbol{H} \tag{3}$$

where γ is the propagation wave number (defined in Equation 4), with α as the attenuation (defined in Equation 5) and β as the phase variables (defined in Equation 6). The wavelength λ of the wave propagating from the electromagnetic field is $\lambda=2\pi/\beta$.

$$\gamma = \alpha + j\beta = \sqrt{j\omega\mu(\sigma + j\omega\varepsilon)} \tag{4}$$

$$\alpha = \omega\sqrt{\mu\varepsilon}\left[\frac{1}{2}\left(\sqrt{1+\left(\frac{\sigma}{\omega\varepsilon}\right)^2}-1\right)\right]^{1/2} \quad \left(\frac{Np}{m}\right) \tag{5}$$

$$\beta = \omega\sqrt{\mu\varepsilon}\left[\frac{1}{2}\left(\sqrt{1+\left(\frac{\sigma}{\omega\varepsilon}\right)^2}+1\right)\right]^{1/2} \qquad \left(\frac{rad}{m}\right) \qquad 6$$

The magnetic permeability $\mu = \mu_0 = 4\pi \cdot 10^{-7}\text{H/m}$ of the medium does not change for non-magnetic media. σ is the conductivity of the medium, which in this case is dependent on the salinity of the water, its temperature and pressure. The salinity of the water is proportional to the concentration of dissolved salts (chloride, sodium, sulphate, etc.). In marine water, the conductivity ranges from 2 S/m to 6 S/m for frequencies lower than 10 GHz, being considered constant 4 S/m in most cases [29]. In freshwater, the considerations are the same. However, the salinity is lower, which means that the conductivity of the water is lower (typically ranging from 30 to 2000 μS/cm) [29]. The Figure 2 shows the conductivity for the different water salinities. Due to the conductivity, Eddy currents are induced within the water, caused by the propagating magnetic field [93]. These Eddy currents are a source of attenuation of the magnetic field.

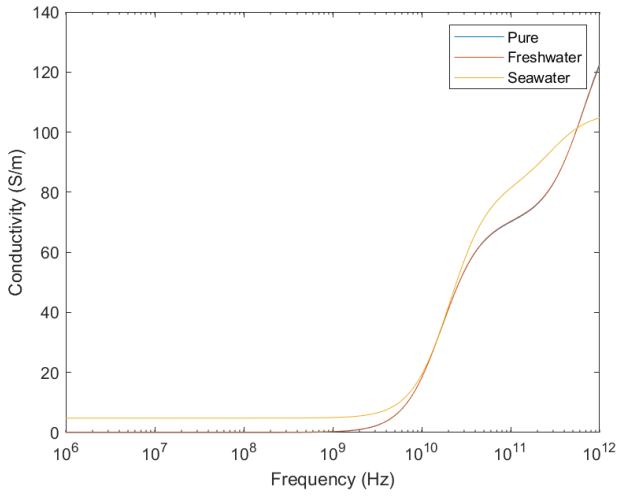

Figure 2 - Conductivity of pure, freshwater and seawater for different values of propagating frequencies.

The conversion between salinity and conductivity for seawater has been defined in the practical-salinity-scale PSS-78 [94]. This scale defines a standard ratio between any measured combination of salinity, conductivity, and temperature in relation to a standard value of conductivity and temperature for seawater of salinity 35 g/Kg.

The dielectric permittivity of the medium ε is defined by $\varepsilon = \varepsilon_r \varepsilon_0$, $\varepsilon_0 = 8.854 \times 10^{-12}\mathrm{F/m}$ being the permittivity in free-space and ε_r the relative permittivity of the medium. This relative permittivity is dependent on the composition of the medium that is polarised when placed under an electric field [95], [96]. Equation 7 shows the relationship between the relative permittivity and the frequency of the propagating electromagnetic wave for pure water as modelled by Debye [96].

$$\varepsilon_r(\omega) = \varepsilon_\infty + \frac{\varepsilon_s - \varepsilon_\infty}{1 + j\omega\tau} \qquad 7$$

In this equation, τ is a time constant of the exponentially increasing orientation polarisation called relaxation time, and ε_s and ε_∞ are the static and infinite frequency relative permittivities of the medium. All these parameters are dependent on the temperature of the water under test, as shown in Equations 9 - 19.

However, for freshwater and seawater, due to the interaction between molecules and the presence of ions that increase the conductivity of the medium, the simple model is not enough to accurately predict the permittivity [95].

For freshwater, there are extensive experimental studies and various models that predict the dielectric permittivity [97]–[101].

Work has been described by Stogryn et al., Meissner and Wentz, and Klein and Swift in [99], [102]–[104] to empirically determine a model for the relative permittivity of seawater, but the results are inconclusive. The International Telecommunication Union released a recommendation [105] that advises on the most accurate model to use when calculating the dielectric permittivity and conductivity of seawater based on its salinity, which will be used in this thesis. Equation 8 shows how to calculate the relative dielectric permittivity based on this model.

$$\varepsilon_r = \frac{\varepsilon_{SS} - \varepsilon_{1S}}{1 + (f_{GHz}/f_{1S})^2} + \frac{\varepsilon_{1S} - \varepsilon_{\infty S}}{1 + (f_{GHz}/f_{2S})^2} + \varepsilon_{\infty S} \quad (8)$$

The following equations 9-19 show the calculations for each of the parameters from Equation 8.

$$\varepsilon_{SS} = \varepsilon_S exp(-3.33330 \times 10^{-3} S + 4.74868 \times 10^{-6} S^2) \quad (9)$$

$$f_{1S} = f_1\big(1 + S(2.3232 \times 10^{-3} - 7.9208 \times 10^{-5} T + 3.6764 \times 10^{-6} T^2 + 3.5594 \times 10^{-7} T^3 + 8.9795 \times 10^{-9} T^4)\big) \quad (10)$$

$$\varepsilon_{1S} = \varepsilon_1 exp(-6.28908 \times 10^{-3} S + 1.76032 \times 10^{-4} S^2 - 9.22144 \times 10^{-5} TS) \quad (11)$$

$$f_{2S} = f_2\big(1 + S(-1.99723 \times 10^{-2} + 1.81176 \times 10^{-4} T)\big) \quad (12)$$

$$\varepsilon_{\infty S} = \varepsilon_\infty\big(1 + S(-2.04265 \times 10^{-3} + 1.57883 \times 10^{-4} T)\big) \quad (13)$$

$$\varepsilon_S = 77.66 + 103.3\Theta \quad (14)$$

$$\varepsilon_1 = 0.0671\varepsilon_S \quad (15)$$

$$\varepsilon_\infty = 3.52 - 7.52\Theta \quad (16)$$

$$\Theta = \frac{300}{T + 273.15} - 1 \quad (17)$$

$$f_1 = 20.20 - 146.4\Theta + 316\Theta^2 \quad (18)$$

$$f_2 = 39.8 f_1 \quad (19)$$

in which T is the temperature in degrees Celsius (°C), f_{GHz} is the frequency of the signal in GHz, S is the salinity in g/kg or ppt, and f_1 and f_2 are the Debye relaxation frequencies for pure water.

From the same model, the conductivity σ is shown in Equation 20.

$$\sigma = \sigma_{35} R_{35} R_{T15} \quad (S/m) \quad (20)$$

The following Equations 21-25 show the calculations for each of the parameters from Equation 20.

$$\sigma_{35} = 2.903602 + 8.607 \times 10^{-2} T + 4.738817 \times 10^{-4} T^2 - 2.991 \times 10^{-6} T^3 + 4.3047 \times 10^{-9} T^4 \quad (21)$$

$$R_{35} = S \frac{(37.5109 + 5.45216S + 1.4409 \times 10^{-2} S^2)}{(1004.75 + 182.283S + S^2)} \quad (22)$$

$$R_{T15} = 1 + \frac{a_0 (T - 15)}{a_1 + T} \quad (23)$$

$$a_0 = \frac{(6.9431 + 3.2841S - 9.9486 \times 10^{-2} S^2)}{(84.850 + 69.024S + S^2)} \quad (24)$$

$$a_1 = 49.843 - 0.2276S - 0.198 \times 10^{-2} S^2 \quad (25)$$

Figure 2 shows the influence of the frequency of the signal in the conductivity of the medium. Figure 3 shows the complex permittivity for pure water, freshwater, and seawater as a function of the frequency according to Equation 26.

$$\hat{\varepsilon} = \varepsilon_r - j\varepsilon_r'' = \frac{\varepsilon}{\varepsilon_0} - j\frac{\sigma}{\omega\varepsilon_0} \quad (26)$$

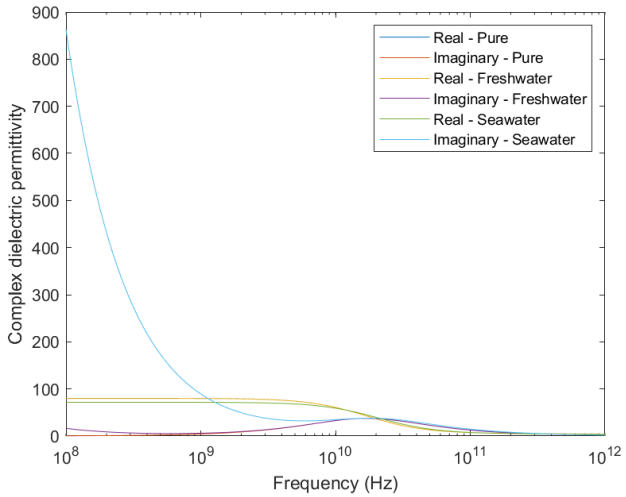

Figure 3 - Real (relative permittivity) and imaginary parts of the complex dielectric permittivity for pure water, freshwater (Salinity = 0.5 g/kg) and seawater (Salinity = 35 g/kg) at temperature T = 20°C.

The dielectric permittivity and the conductivity are then used to determine the attenuation factor α. In [106], the authors propose a review of this model to account for the difference between the theoretical calculations and the empirical data of the attenuation of radio waves underwater. The experiments show that the signal attenuation at higher distances ($\gg$10 m) is not as strong as predicted. Therefore, they redefine α as a corrected absorption factor α' that matches experimental results closely shown in Equation 27 below:

$$\alpha' = \alpha\left(\frac{\lambda}{\lambda + z}\right) \quad (27)$$

For the Transverse Electromagnetic Mode to the positive z direction in lossy medium (in this case, water), **E** and **H** can be derived as shown in Equations 28 and 29 below [92]:

$$\boldsymbol{E}(\boldsymbol{z}) = \hat{\boldsymbol{a}}_{\boldsymbol{x}} E_0 e^{-\gamma z} \quad (28)$$

$$\boldsymbol{H}(\boldsymbol{z}) = \hat{\boldsymbol{a}}_{\boldsymbol{y}} \frac{\gamma}{j\omega\mu} E_0 e^{-\gamma z} \qquad 29$$

For a given antenna, the space that surrounds it can be separated into three regions: (a) a reactive near-field, (b) a radiating near-field and (c) the far-field. There are no abrupt changes at their boundaries [107]. A representation of these regions can be seen in Figure 4.

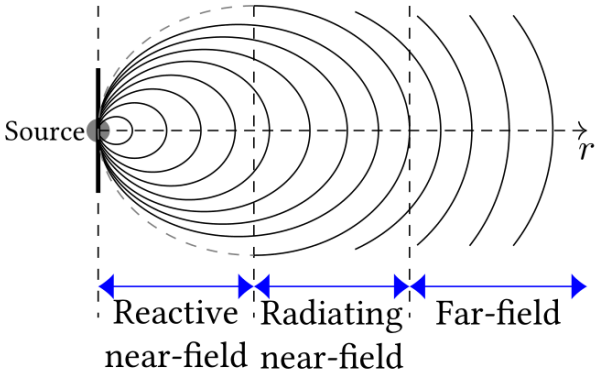

Figure 4 - Field regions for a propagating electromagnetic wave leaving an antenna.

The *Reactive Near-Field* is the space immediately near the antenna where the reactive field predominates (magnetic field). For most antennas, the limit of this region is at $0.62\sqrt{D^3/\lambda}$ [107], where D is the biggest dimension of the antenna. The *Radiating Near-Field* is located between the reactive near-field and the far-field and is the space wherein radiation fields are dominant. The angular field distribution is determined by the distance from the antenna. This field existence depends on the ratio between antenna size D and the wavelength λ: if $D/\lambda \ll 1$ then this region does not exist. The *Far-Field* is the region wherein the electrical and magnetic components of the field become orthogonal to each other as they separate from the antenna and propagate as an electromagnetic wave. The lower boundary of this region is located at $2D^2/\lambda$ for any antenna [92], also considered to be $\lambda/2\pi$ for dipole antennas. According to [73], a good approximate rule for RFID systems is to define the beginning of the far-field at $\lambda/2\pi$.

The field boundary distance is different for each medium due to the difference in wavelength. Tables I and II show the values for the attenuation coefficient, wavelength, and far-field boundary for freshwater and seawater, respectively.

Current RFID systems can be separated into two categories: near-field systems that work with inductive coupling due to the dominance of the magnetic field in the near-region, and far-field systems that receive power from the propagating electromagnetic waves in the far-field [108]. The frequencies used in each region are different. Since the lower frequencies – such as Low Frequency (LF) at around 134.2kHz and High Frequency (HF) at 13.56MHz – have a far-field boundary that is further away, they are mainly used in inductive coupling systems. Higher frequencies are then used mostly in far-field systems.

Table I - Values of attenuation factor α, wavelength λ and far-field boundary $z_F = \lambda/2$ for freshwater (S = 0.5 g/Kg).

Frequency	**α (Np/m)**	**λ (m)**	**z_F (m)**
134.2 kHz	2.16E-01	2.89E+01	4.60E+00
13.56 MHz	1.58E+00	2.10E+00	3.34E-01
433.9 MHz	2.83E+00	7.73E-02	1.23E-02
915 MHz	6.16E+00	3.67E-02	5.84E-03
1.5 GHz	1.34E+01	2.24E-02	3.57E-03
2.4 GHz	3.11E+01	1.41E-02	2.24E-03
5 GHz	1.24E+02	6.91E-03	1.10E-03

Table II - Values of attenuation factor α, wavelength λ and far-field boundary $z_F = \lambda/2$ *for seawater (S = 35 g/Kg).*

Frequency	α (Np/m)	λ (m)	z_F (m)
134.2 kHz	1.59E+00	3.94E+00	6.27E-01
13.56 MHz	1.59E+01	3.90E-01	6.20E-02
433.9 MHz	7.63E+01	5.80E-02	9.22E-03
915 MHz	9.51E+01	3.34E-02	5.32E-03
1.5 GHz	1.07E+02	2.19E-02	3.49E-03
2.4 GHz	1.25E+02	1.42E-02	2.27E-03
5 GHz	2.01E+02	7.08E-03	1.13E-03

3.4.1 Near-field

In the near-field, the magnetic field created by the reader's antenna induces a voltage in the transponder immersed in this field. This is called *inductive coupling* and the interaction between reader and transponder can be considered as coupled inductors. This method of communication can also be called *Magnetic Induction (MI)*.

Consider the equivalent circuit for the inductively coupled system shown in Figure 5. The transmitter antenna is fed by a source with internal impedance Z_S and the receiver antenna is terminated by a load impedance Z_L. The transmitter coil antenna has an impedance of $Z_{TX} = R_{TX} + j\omega L_{TX} + 1/(j\omega C_{TX})$ and the receiver coil antenna is $Z_{RX} = R_{RX} + j\omega L_{RX} + 1/(j\omega C_{RX})$.

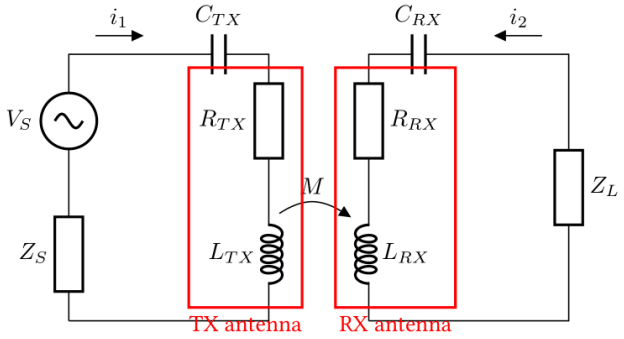

Figure 5 - Inductive coupling between reader and transponder.

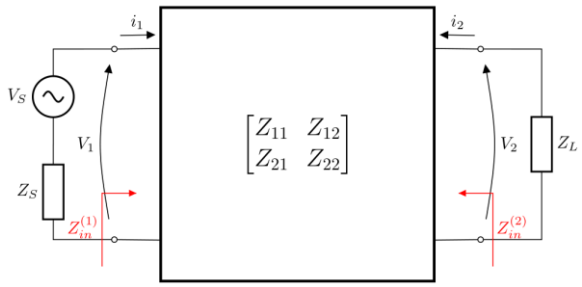

Figure 6 - Two-port network equivalent of the system.

Using the two-port network equivalent (Figure 6) and considering an ideal source for V_S, $Z_{11} = Z_{TX}$ and $Z_{22} = Z_{RX}$ are the self-impedances of the coils and $Z_{12} = Z_{21} = j\omega M$ are the mutual impedances due to the coupling. The Equation 30 shows the two-port network model:

$$\begin{pmatrix} V_1 \\ -Z_L I_2 \end{pmatrix} = \begin{bmatrix} z_{11} & z_{12} \\ z_{21} & z_{22} \end{bmatrix} \cdot \begin{pmatrix} I_1 \\ I_2 \end{pmatrix} \qquad 30$$

The resistance of a coil is $R = N \cdot 2\pi a \cdot R_0$, where N is the number of turns of the coil, a is the diameter of the coil and R_0 is the resistance of a unit of length of the wire used to fabricate the coil. The self-inductance L is calculated as Equation 31 shows:

$$L = \frac{\mu \pi^2 N^2 a}{l} \quad (H) \qquad 31$$

where l is the length of the coil. In the free space, the magnetic field strength generated by a coil antenna in the near field H_0 is shown in Equation 32 below [73]:

$$H_0 = \frac{Na^2 I}{2(a^2 + z^2)^{3/2}} \quad (A/m) \tag{32}$$

The magnetic field magnitude for a lossy medium is then $H = H_0 exp(-\alpha z)$ according to (29). This magnetic field induces a voltage in the tag's coil antenna, given by Equation 33:

$$U_2 = -N_2 \frac{d\Phi_{21}}{dt} = -M \frac{di_1}{dt} \tag{33}$$

where $\Phi_{21} = \int \mathrm{b}B \cdot d\boldsymbol{S}$ is the magnetic flux through each turn, $\boldsymbol{B} = \mu \boldsymbol{H}$ the magnetic field and **S** the surface area of the coil. Considering that the reader's and tag's coils are aligned, and using Equation 32, the magnetic field in the z direction is given by Equation 34:

$$B_z = \left(\frac{\mu N a_1^2 I}{2(a_1^2 + z^2)^{2/3}} \right) e^{-\alpha z} \tag{34}$$

Therefore, the mutual inductance $M = k\sqrt{L_1 L_2}$ is shown in Equation 35.

$$M = \left(\frac{\mu \cdot \pi \cdot N_1 \cdot a_1^2 \cdot N_2 \cdot a_2^2}{2 \cdot (a_1^2 + z^2)^{3/2}} \right) \cdot e^{-\alpha z} \tag{35}$$

where α is the attenuation constant of the medium.

The transmission power can be defined as the power consumed by the radiation resistance in the reader (transmitter) antenna, shown in Equation 36:

$$P_{TX} = \frac{1}{2} Re(Z_{11}) \cdot |I_1|^2 \tag{36}$$

The received power is defined as the power consumed in the load, shown in Equation 37:

$$P_{RX}(z) = \frac{1}{2} Re(Z_L) \cdot |I_2|^2 \quad (37)$$

Using (30) and considering $Z_S \approx 0$, the received power can be written as shown in Equation 38:

$$P_{RX}(z) = P_{TX} \frac{Re(Z_L)\omega^2 M^2}{Re(Z_{TX})|Z_L + Z_{RX}|^2} \quad (38)$$

Path loss in decibels (dB) can be defined as Equation 39:

$$PL = -10 \log_{10} \left(\frac{P_{RX}}{P_{TX}} \right) (dB) \quad (39)$$

The path loss is a function of the number of turns and radius of both coils and the impedances of the system, as well as the frequency and the distance between reader and tag. The highest amount of power is transferred to the load when its impedance is matched with the impedance of the antenna.

The path loss for the MI system increases with the increasing distance between reader and tag. Also, the path loss is higher for seawater due to the higher conductivity of the medium. As the frequency increases, the distance from the reader where the border between the near and the far-field is located decreases. This implies that the maximum theoretical range decreases with frequency. We can then conclude that there is an optimal combination of frequency and distance for each application. In addition to that, the attenuation factor α is higher for higher frequencies.

The influence of the number of turns of the transmitter or the receiver coil in the mutual inductance M is linear. Therefore, the power received would increase quadratically with the increase in the number of turns. However, it

also increases the energy losses in the internal resistance of the coil as it increases. It is also worth noting that a bigger coil diameter allows for more magnetic flux to pass through, but it also has the effect of increasing the internal resistance of the coil.

A more in-depth model of underwater magnetic induction communication can be found in [79]. The model shown here assumes that the reader and tag coils are oriented in the same direction, with the field strength reaching zero if the angle between coils is 90°. To remove this limitation, the authors in [109] present a model of the Underwater MI channel for a tri-directional coil. To increase the achievable range of MI systems, waveguides can be used [72], [110]. The authors in [81] provide a different but similar model that is based on the quality factor of the coil inductor.

3.4.1.1 Data transmission from tag

When a transponder is located in the magnetic alternating field generated by the reader, the reader 'sees' the transponder as the secondary wing of the transformer. This means that the transponder's impedance is reflected back to the reader as the *transformer impedance* Z_T.

If the transponder antenna impedance changes, this is reflected back to the reader's coil via the reflected impedance Z_T. Therefore, a data stream can be transmitted via modulation of the voltage Z_L in the reader's coil (called *Load Modulation*); this can be demodulated by the reader via rectification of the voltage [73]. This is only feasible in the near-field as if the transponder leaves the appropriate read range, the coupling is lost and the transmission link is not operational anymore.

For an amplitude modulating system, due to the weak coupling between reader and transponder antennas, the voltage fluctuation is orders of magnitude smaller than the voltage provided by the reader. As a direct result,

the reader has to integrate a complex circuitry to separate noise from the signal and detect the data stream. On the other hand, if the transponder modulates the signal at a frequency f_s, smaller than the frequency of the magnetic field (f_0), two spectral lines $\pm f_s$ are created and they can be filtered with a band-pass filter and demodulated more easily [108].

3.4.2 Far-field

In the far-field, the electromagnetic fields separate completely from the reader's antenna and become propagating waves, no longer retroacting upon the reader's antenna. These waves are captured by the antenna on the transponder. The energy on the antenna is rectified and used to power up the IC. The frequency range commonly used for this type of transmission is the Ultra-High Frequency (UHF) and Microwave.

A linearly polarized plane EM wave propagating in lossy media in the z-direction can be described by the electric field strength E_x in Equation 40:

$$E_x = E_0 e^{j\omega t - \gamma z} \qquad 40$$

with $\gamma = \alpha + j\,\omega\beta$ as the propagating constant according to Equations 5 and 6.

The radiation power density S is the instantaneous value of the Poynting vector **S=E×H**. From Balanis 2012 [92] and using Equation 29, we get the radiation power density in Equation 41:

$$\boldsymbol{S} = \frac{1}{2} Re(\boldsymbol{E} \times \boldsymbol{H}) = \hat{\boldsymbol{a}}_{\boldsymbol{z}} \frac{|E_0|}{2} e^{-2\alpha z} Re\left(\frac{1}{\eta_c^*}\right) \qquad 41$$

where η_C is the intrinsic impedance of the medium, given by Equation 42.

$$\eta_C = \sqrt{\frac{j\omega\mu}{\sigma + j\omega\varepsilon}} \quad 42$$

For the transmitting antenna in the free-space, s_0 is the power supplied to it over the area of the spread surface, as shown in Equation 43:

$$S_0 = \frac{P_{EIRP}}{4\pi z^2} = \frac{P_{TX}G_{TX}}{4\pi z^2} \quad 43$$

Whereas the radiation power density in a lossy medium is then shown in Equation 44:

$$S = S_0 e^{-2\alpha z} \quad 44$$

For the receiving antenna, the average power received is the radiation power density times its effective receiving area A_e, shown in Equation 45 [106]:

$$P_{RX} = S \cdot A_e = S \cdot \frac{G_{RX}\lambda^2}{4\pi} \quad 45$$

The transmission equation then can be written as Equation 46:

$$P_{RX} = P_{TX}\left(\frac{G_{TX}G_{RX}\lambda^2}{(4\pi z)^2}\right)e^{-2\alpha z} \quad 46$$

where G_{TX} and G_{RX} are the antenna gains for transmitter and receiver respectively, λ=(2π)/β is the wavelength, and z is the distance between antennas. This equation assumes that the antennas are aligned and have the same polarization. The path loss PL_{EM} in decibels is then defined as $PL_{EM} = -10\log_{10}(P_{RX}/P_{TX})$.

3.4.2.1 Data transmission from tag

For passive RFID, the method of transmitting back to the reader is via *Backscatter*. Electromagnetic waves are reflected by objects that are larger than half the wavelength ($\lambda/2$) [73]. The efficiency of this reflection depends on the

radar cross-section of the object: antennas that are resonant with the waves have a larger reflection cross-section. The reflection characteristics can be altered by changing the load that is connected to the antenna. For example, if a load R_L is switched on and off while connected to the antenna, this changes the reflection characteristics of the antenna, generating a modulated backscatter signal [73]. The range is limited by the amount of energy that reaches the tag (path loss) and the sensitivity of the reader's receiver to the reflected signal (reflected signal strength $\propto 1/x^4$) [111]. The authors Rao and Nikitin in [112] present a method for measuring the backscatter of an RFID tag and for calculating its radar cross-section. They utilise a network analyser connected to an anechoic chamber.

3.5 MEASUREMENTS OF MAGNETIC FIELD STRENGTH ON DIFFERENT WATER SALINITIES

An experimental setup was developed to explore the difference in magnetic field strength in free-space compared to the field strength in water in the near-field region. An Anritsu MS2038C VNA Master [113] vector network analyser and a probe 100C from Beehive Electronics, USA [114] were used to measure the magnetic field strength at the system's resonant frequency of 13.56 MHz. Two Evaluation Kit RFID readers were used: *MRD2EVM* from Texas Instruments, USA that operates at 134.2 kHz [115] and *Pepper Wireless C1 USB* from Eccel Technology Ltd, UK that operates at 13.56 MHz [116]. Both readers have square loop antennae embedded on a printed circuit board, with sides of length 3.0 cm and 4.5 cm, and number of turns 14 and 3, respectively.

For a square loop antenna with *N*-turns, the magnetic field strength in free-space can be written as shown in Equation 47 [117]:

$$H_0 = \frac{NI}{2\pi\left(\frac{z^2}{l^2}+\frac{1}{4}\right)\sqrt{z^2+\frac{l^2}{2}}} \qquad 47$$

where z is the distance from the centre of the antenna and l is the length of the side of the antenna. Using Equation 29, for a lossy medium (in this case saline water), the magnetic field strength is then as shown in Equation 48.

$$H = H_0 exp(-\alpha z) \quad 48$$

Using the attenuation factor α from Equation 5 with the salinity and frequency, we can then calculate the theoretical values for the magnetic field strength for any distance and compare this with the measurements made with the probe.

For both systems, the setup for the experiments was the same, as seen in Figure 7. The readers were placed and secured on the side of a plastic transparent container. The probe was placed in different distances z from the centre of the embedded antenna of the reader. A measurement ruler and grid paper were used for the precise placement of the probe. The free-space tests were carried out without water inside the container. For the subsequent measurements, the probe was submerged in the water solution to get the measured field strength.

For the experimental test, 4 different water solutions were used, namely: distilled water, freshwater, brackish water, and saline water. The water solutions were prepared as follows. First the container was placed on a scale, and the appropriate mass of NaCl was added, according to the target value of salinity for each solution, following general definitions of salinity for freshwater (< 0.5 g/Kg), brackish water (0.5 – 30 g/kg), and saline water (30 g/kg – 50 g/Kg) [118], [119]. Then, distilled water was added until the whole solution mass reached 700g (the weight correspondent to the water volume of the plastic container used for the experiments). Table III shows the mass of salt for each solution and their salinity and calculated conductivity.

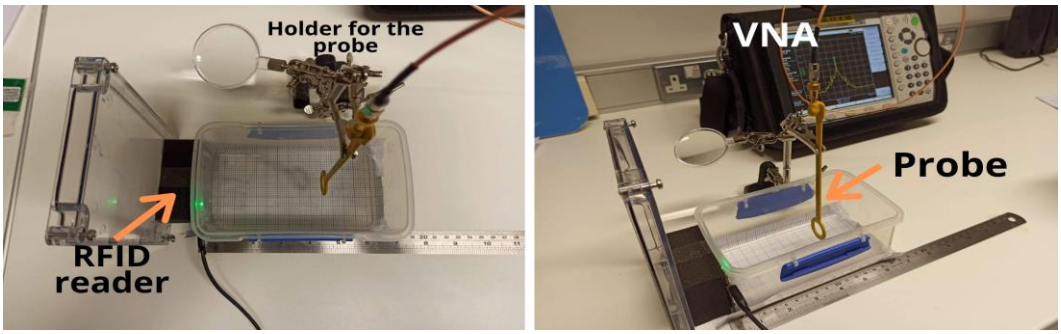

Figure 7 - Experimental setup for measuring the magnetic field strength consisting of a plastic container, magnetic probe, holder and stand for the probe and VNA. Each RFID reader system was placed and secured on the side of the plastic container.

Table III - Solutions used for the experiment, temperature at which they were mixed, their salinity and calculated conductivity for each solution according to [107].

Solution	NaCl mass	Total mass	Salinity	Tempe-rature	Calculated Conductivity (at 1 MHz)
Freshwater	0.35 g	0.7002 kg	0.499 g/kg	19 C	0.093 S/m
Brackish Water	10.5 g	0.7003 kg	14.99 g/kg	18 C	2.32 S/m
Saline Water	24.5 g	0.7003 kg	34.98 g/kg	19 C	5.04 S/m

For each solution, the probe was placed and held at different distances from the centre of the antenna and the peak value of the magnetic field was measured using the VNA. After this was carried out, the probe was wiped so there was no contamination between solutions.

The output power values measured by the probe P_{out} were then converted from dBm to magnetic field strength in A/m using the probe manufacturer's guidelines [114], using Equations 49 and 50, where f_{MHz} is the frequency of the system in MHz, B_{out} is the magnetic flux density, and H_{out} is the magnetic field strength. The raw data collected from the probe and the VNA in dBm can be found in Tables IV and V.

$$20 \times log_{10}(B_{out}) = P_{out} - 42.2 - 20 \times log_{10}(f_{MHz}) \quad 49$$

$$H_{out} = \frac{10^{B}}{\mu} \quad (A/m) \quad 50$$

Table IV - Measured values of P_{out} in dBm for the 134.4kHz system for Free-space (Free), Distilled Water (DW), Freshwater (FW), Brackish Water (BW) and Saline Water (SW) solutions

z (cm)	F (dBm)	DW (dBm)	FW (dBm)	BW (dBm)	SW (dBm)
0.2	-2.2	-2.18	-2.63	-3.62	-1.96
1	-9.66	-7.68	-6.84	-8.34	-7.35
2	-13.82	-14.24	-13.36	-15.42	-14.13
3	-20.2	-21.13	-19.6	-21.06	-20.22
4	-26.1	-25.95	-25.41	-25.81	-25.72
5	-30.15	-30.69	-30.27	-30.04	-30.43
6	-34.02	-34.44	-33.41	-34.06	-34.16
7	-37.7	-37.36	-36.75	-37.24	-37.3
8	-40.9	-40.76	-40.42	-40.56	-40.79
9	-43.34	-43.66	-42.79	-43.07	-43.26
10	-45.65	-45.66	-45.31	-45.84	-45.9

Table V - Measured values of P_{out} in dBm for the 13.56MHz system for Free-space (F), Distilled Water (DW), Freshwater (FW), Brackish Water (BW) and Saline Water (SW) solutions.

z (cm)	F (dBm)	DW (dBm)	FW (dBm)	BW (dBm)	SW (dBm)
0.2	11.64	11.09	11.03	10.7	9.49
1	7.72	7.96	7.87	6.65	6
2	2.74	2.32	2.58	1.73	1.24
3	-2.37	-2.12	-2.06	-3.84	-4.15
4	-6.92	-7.06	-7.01	-7.94	-8.53
5	-10.92	-11.56	-10.76	-11.95	-12.75
6	-14.33	-15.02	-14.92	-15.63	-16.7
7	-17.76	-17.94	-17.56	-18.28	-19.74
8	-20.56	-20.52	-20.88	-21.65	-22.76
9	-23.26	-23.76	-23.66	-24.12	-25.51
10	-25.76	-25.66	-25.96	-26.6	-27.76

Figure 8 shows the measured values of magnetic field strength for the 134.2 kHz system, while Figure 9 shows the values for the 13.56MHz system.

Figure 10 and Figure 11 show the comparison between measured values of field strength and the theoretical values expected using a calculated α based on the level of the water salinity. For the results shown in these figures the peak current (A) flowing through the antennas was measured under the same experimental conditions, and Equation 47 was used.

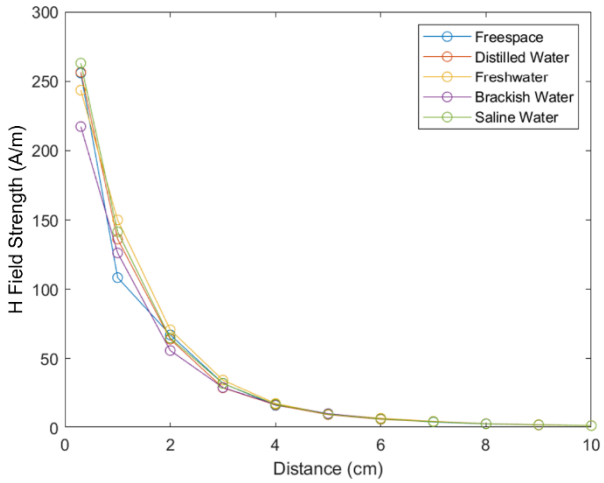

Figure 8 - Measured magnetic field strength values for the Texas Instruments MRD2EVM evaluation kit (f=134.2 kHz).

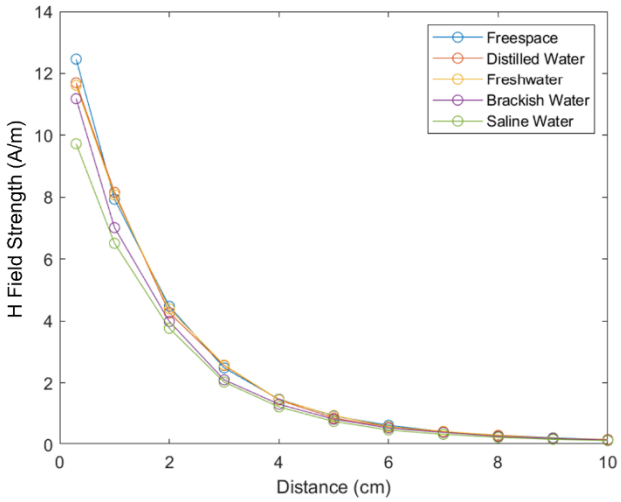

Figure 9 - Measured magnetic field strength values for the Eccel Technology Pepper C1 USB evaluation kit (f=13.56 MHz).

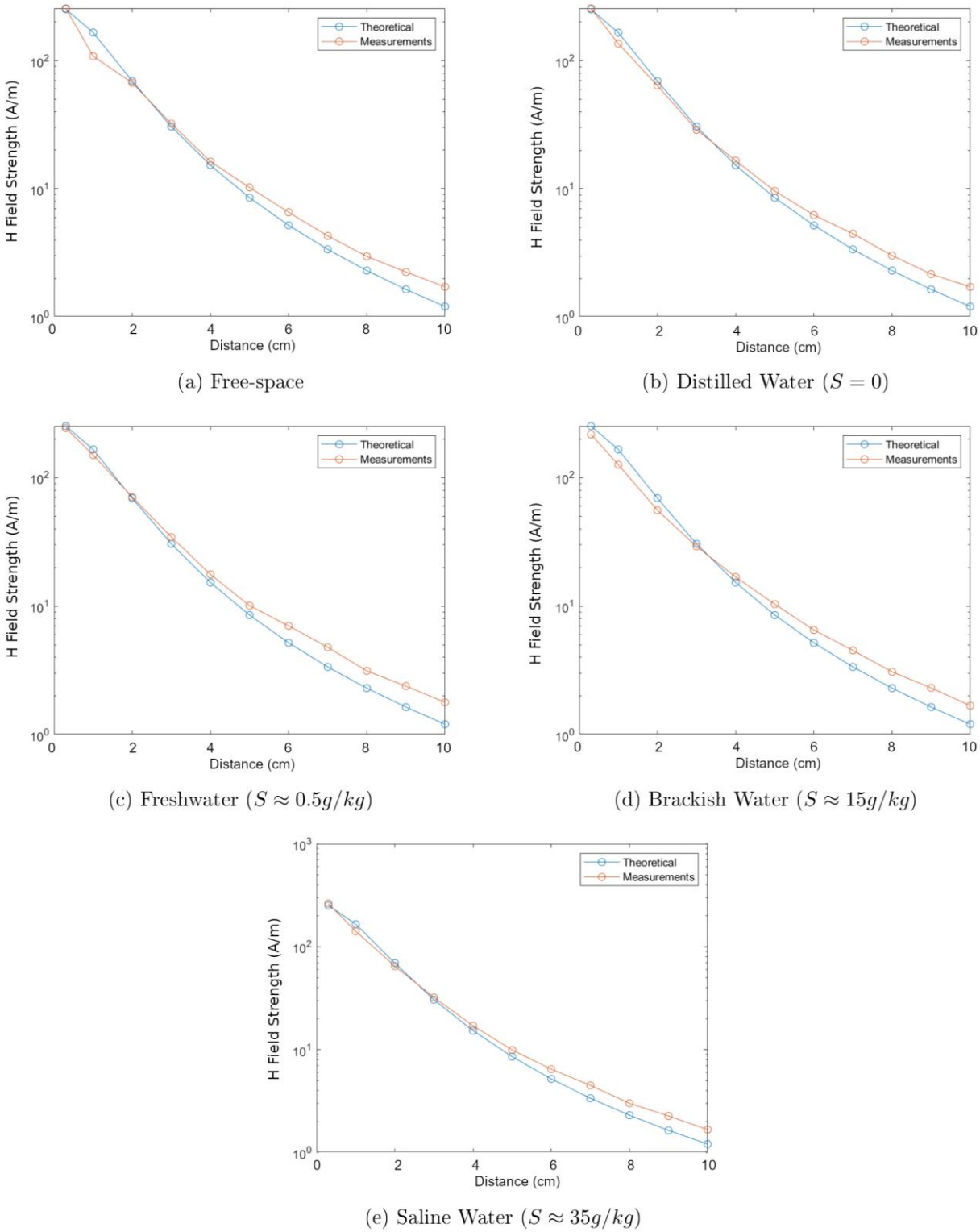

(a) Free-space

(b) Distilled Water ($S = 0$)

(c) Freshwater ($S \approx 0.5g/kg$)

(d) Brackish Water ($S \approx 15g/kg$)

(e) Saline Water ($S \approx 35g/kg$)

Figure 10 - Comparison between measured values of magnetic field strength for different salinity values underwater for the 134.2kHz system.

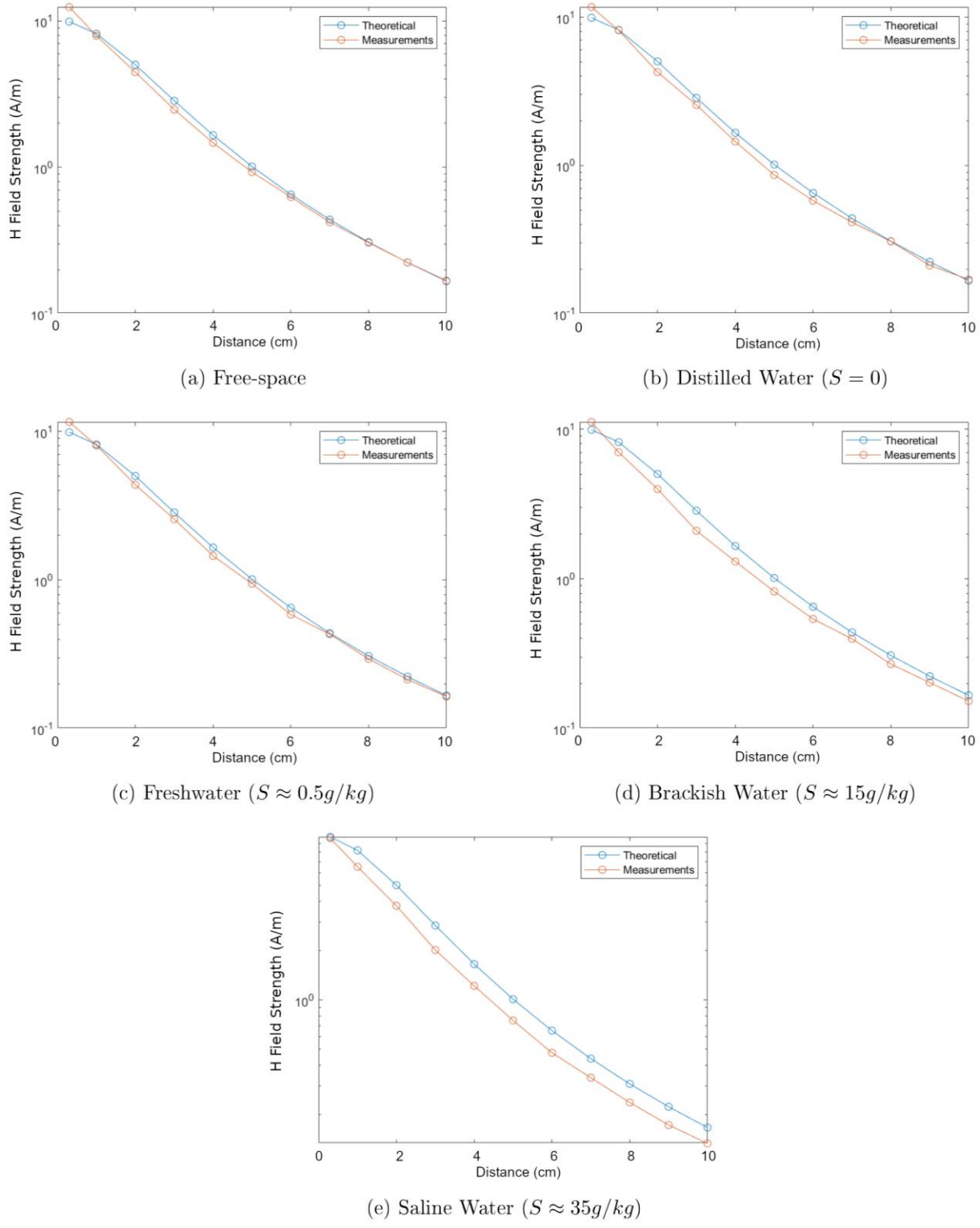

Figure 11 - Comparison between measured values of magnetic field strength for different salinity values underwater for the 13.56MHz system.

3.6 DISCUSSIONS ON THE USE OF RFID IN MARINE APPLICATIONS

The most common method of wireless transmission underwater is acoustic communication. This is due to the long range that can be accomplished with this technology. However, some applications do not need such long range and are deeply affected by acoustic noise and refractions, reflections and multipath, due to the proximity to the water surface, such as in coastal environments. In these cases, wireless communication can be better served by other methods that do not suffer from these problems. We explore the possibility of using RFID technology to better serve these environments.

In the near-field region, the magnetic component of the electromagnetic field dominates. The method of communication for RFID in this region is MI. Compared to other methods of underwater communications, MI has several advantages. It is not affected by multipath propagation or fading and the magnetic field can cross the water to air boundary with low attenuation [72]. The signal propagation delay is negligible if compared to acoustic waves. The channel response is predictable, and a sufficiently large range can be achieved with modest data rates [78].

For the far-field, the electromagnetic field propagates as a wave, and the communication is realized through radiofrequency. Due to the high attenuation, there is a severe constraint on data rates and propagation distances for this method [25]. Lower frequency signals have lower attenuation (due to conductivity of the water) but require larger antennas. This also limits the bandwidth of the system due to the lower frequency of operation. Higher frequency systems would then require more power to reach the same ranges. Shallow water environments, in particular, pose a problem to wave propagation due to the proximity to the water/air upper boundary and to the river/sea bed, which causes multipath propagation [24], [26].

Both technologies do not require line-of-sight and are unaffected by light and acoustic ambient noise. Moreover, the channel response is independent of water quality conditions, such as turbidity. The literature generally agrees that the achievable range for a given transmission power is not great for both MI and RF. The reasoning is due to the high attenuation caused by the medium conductivity which increases with the salinity of the water. From this, it follows that long-range transmissions underwater, particularly in a marine environment, are best served by acoustic communication based systems [25].

However, there is some evidence that this attenuation could be lower than expected. The authors in [120] managed to transmit a RF signal at 90 m distance in seawater with a lower attenuation than expected. To reflect this results, [106] propose the change in the attenuation factor α to α' according to Equation 27. In addition to that, the dielectric permittivity for saline water is not completely understood [95]. There are models available extrapolated from measurement data, but they do not agree completely. Since the dielectric permittivity affects the attenuation, it follows that the attenuation itself could have a different value.

The results from our experiment shown in Figure 10 for the 134.2 kHz system demonstrate that there is a difference between the expected theoretical value and the measured value, especially as the distance increases. Yet, the same cannot be said for the results in Figure 11 for the 13.56 MHz system. In this latter case, the measurements seem to be lower than the expected value. It is not clear what is the cause, but this suggests that higher frequencies suffer higher attenuation in a manner not considered in the model. More research about this is needed to identify if the difference measured is due to a problem in the model or an effect that was not previously considered.

Otherwise, the difference in the measured values for the experiment is potentially caused by a difference between the real world experimental setup and the simulated model. One of the important parameters considered in the model to calculate the attenuation is the water temperature, which was measured as the water solutions were mixed, but not during the experiment or after. Thus, the water temperature could have changed during the experiment, and therefore changed the attenuation factor. For example, the complex dielectric permittivity for seawater at a temperature of 18 °C is $72.325 - 82577\text{j}$ and it changes into $70.088 - 95479j$ at 25 °C. As the permittivity affects the attenuation factor, this in turn would be more noticeable at higher frequencies where the attenuation factor is higher.

Also, the current flowing through the antenna for each device tested was not measured at the time of the experiment, but later. Although the functionality should remain the same, there could be differences in the actual value of the current, which would change the value of the magnetic field.

Other possible sources of error or interference could be the presence of other magnetic fields in the test area. The experiment was not done in a radio-frequency anechoic chamber, so other electronic or electrical devices nearby could produce electromagnetic fields strong enough to interfere.

Even without a complete understanding, as expected a higher water salinity implies in a higher attenuation for the signal. Although the relative permittivity for seawater is slightly smaller than for freshwater, as can be observed in Figure 2 the conductivity for seawater is higher for the frequencies in question, and dominates, increasing the attenuation factor. It is also worth noting that the 134.2 kHz system is not as affected by the increasing salinity of water as the 13.56 MHz system, as it can be seen looking at the values in Tables IV and V. This means that a MI communication system for a marine

environment should be designed with a lower frequency, keeping in mind the needed bandwidth to transmit data and other requirements. This would ensure that the system is efficient, as there is less energy being lost in the transmission.

Some authors, such as Domingo [72], argue that MI has a lower attenuation than RF for freshwater, and similar results for seawater. This fact, combined with its immunity to multipath and fading, implies that MI could be a great alternative for wireless communications underwater. In addition, the achievable range of MI communications can be greatly extended by deploying waveguides that do not require power – simple passive relay coils that guide the magnetic field – such as demonstrated in [72], [110]. For example, Domingo 2012 [72] uses an MI waveguide and achieves a range 26 times higher than a normal MI system. Another development that improves MI communications underwater is to use omnidirectional coils that remove the requirement of the transmitting and receiving coils being aligned [78], [109].

However, to design an underwater RFID system it is required to balance a trade-off between range, transmission power and frequency (and therefore data rate and channel capacity). Nonetheless, the RFID system can always be engineered to achieve the best range given its power budget.

For an MI system, the size and number of turns of the transmitting and receiving coils in the antenna also has an impact on the path loss. A bigger coil diameter increases the generated and captured magnetic flux for the transmitter/reader and receiver/tag, which increases the mutual induction and decreases the path loss. However, this is also a trade-off, as a bigger coil has a bigger internal resistance, requiring more power to transmit. It is also worth noting that some applications have size restrictions.

In the far-field category, the antenna can be carefully designed to provide the best radar cross-section, and therefore antenna gain, for the desired application. Again, the size of the antenna is important, as it is related to the wavelength. There is also a trade-off to be made for the frequency, attenuation, and antenna size: for a lower attenuation, the system would need a lower frequency, which requires a bigger antenna.

An example application that would benefit from MI communication over acoustic would be sensors deployed in coastal areas and fish farms [43]. In these environments, the acoustic noise – from waves, animal life and vessels – and the proximity with the water surface negatively impact acoustic underwater communications. In such scenarios, MI underwater communication would better fulfil the communication mechanisms for the of the system.

3.7 CONCLUSIONS AND FUTURE WORK FOR MARINE RFID BASED COMMUNICATIONS SYSTEMS

Given the existing challenges in wireless underwater communications, it is worth exploring alternatives, such as RFID which may be suitable for certain scenarios. However, underwater RFID communication is not a well-explored topic in the scientific community. In this chapter of the thesis, we expanded on the existing theoretical model for RFID channel characteristics to account for the attenuation that the electromagnetic field suffers underwater. The water salinity is an important factor, which is used to calculate the dielectric permittivity and the conductivity of the water, and therefore, the attenuation. The RFID operation was separated into two categories: near-field and far-field. For both cases, the physical characteristics of the transmission were presented and from this, the equation for path loss was obtained.

In both technologies, the water salinity is an issue as it increases the conductivity of the medium and, therefore, correspondingly increases the attenuation of RFID signals. However, MI communication has advantages over RF in terms of immunity to multipath propagation and fading. In addition, a magnetic field can cross the air/water boundary, which is required for some applications. Therefore, near-field RFID communication is a promising alternative for underwater wireless communications for certain applications.

The model presented in this chapter considers that both the transmitting and receiving antennas are located underwater with no transition borders and other losses. This model could be expanded to account for transition borders such as the air-water interface located at the water surface or the interface with the waterproofing material of the reader and tag.

In this chapter, was also presented measurements for magnetic field strength for two near-field systems in different water salinity conditions. The results for the 134.2 kHz show that the attenuation may not be as strong as expected from theory, especially for larger distances. But the results for the 13.56 MHz follow more closely the expected values, sometimes being even lower than the theory. This seems to imply that there may be a relationship between the attenuation factor and the frequency that is not currently expressed in the model. More experimental data is needed to draw any definitive conclusions.

The results also suggest that a higher concentration of salt in the water increases the attenuation, which agrees with the model. However, the effect is more prominent the higher the frequency, which implies that the best communications solution for marine environments requires the use of lower frequencies to minimise attenuation.

Due to the lower attenuation in sea water, and not suffering from multipath, near-field RFID is a promising solution for short-range communication in marine environments. In particular, for the project, it would enable the farm operators to easily download data from the sensor device. From the results presented in this chapter, we establish that the near-field RFID system used in the sensor device should have as low-frequency as possible. In our case, the frequency chosen firstly was 134.2 kHz, as it is also the frequency used in PIT tag systems. Another important element identified in this analysis is that antenna size affects the transmission distance, as a bigger antenna area allows for more magnetic flux captured by the tag. Thus, the antenna should be as big as possible, though restricted to the device size. The same can be said of the number of turns of the coil antenna, but this parameter also affects the antenna impedance, which in turn affects the resonant frequency, and therefore is a more restrained design parameter. All of these factors are taken in consideration for the antenna design, described in section 4.3.3.

4 SEAWEED SENSOR SYSTEM DEVELOPMENT – HARDWARE AND SOFTWARE DESIGN

This chapter contains part of "Peres, C., Emam, M., Jafarzadeh, H., Belcastro, M. And O'Flynn B. (2021) 'Development of a low-power underwater NFC-enabled sensor device for seaweed monitoring', Sensors 2021, 21. https://doi.org/10.3390/s21144649"

4.1 INTRODUCTION

This chapter explains the development of the IMPAQT Seaweed sensor system (Aquabit) and the rationale for each design consideration based on a review of the literature in this area and defined user requirements from stakeholders and prospective users of such a system (IMTA farmers). The final hardware developed and deployed is a novel miniature low-power NFC-enabled data acquisition system to monitor aquaculture species. This sensor system monitors temperature, light intensity, depth, and motion, logs the data internally, and can transmit the logged data.

As described in Chapter 2, no integrated in-situ multi-sensing solution for seaweed monitoring exists (to the best of our knowledge). From the literature review done, the sensory modalities to be included in the device were identified as the most important environmental parameters that affect seaweed growth. Also from the literature, we identified that different sensor deployment objectives require different data collection frequency [64].

The importance of remote monitoring of these environmental parameters was also highlighted in various studies [6], [45]. As the current remote sensing technology for seaweed monitoring does not provide very fine resolution, we aim to fill this need with the device developed. In this sense, we have explored the most promising communication technology option identified in the literature – RFID – in Chapter 3. From the experiments, we identified near-

field communication in lower frequencies as the best option for underwater transmission.

From these studies and experiments, and the review of the state-of-the-art in the area of marine monitoring systems, we compiled a list of requirements for the sensor device. This list was presented to stake-holders and end users of IMTA/seaweed farms of the IMPAQT project, which have contributed to the final requirement list. These requirements are shown below:

- The sensory modalities embedded in the device are to be temperature, depth, light intensity, and wave motion, as they are considered the main parameters that affect seaweed growth [51].
- The device must be as small as possible as to not disturb the seaweed physiology; be reusable to reduce environmental waste and pollution; waterproof and resistant to the marine environment. It needs to be able to be attached securely to the seaweed via either gluing or threading.
- The sensors should be configurable regarding sampling frequency and other relevant parameters to allow greater customisation in the deployment; and be capable of high-frequency (> 100 Hz) accelerometer sampling to allow the capture of fast movement.
- The device must have a battery and wireless communication to be able to collect the logged data remotely.
- The battery should be rechargeable to reduce waste, and its lifetime should be maximised to allow longer periods of deployment without the need for farm operator interaction.

Terms, acronyms, and definitions

- *Shutdown mode*: All internal devices that have an active state must be turned off. In this case, the only device allowed to remain in a "active

sleep" status is the wake-up subsystem. This is to minimize battery consumption, as the battery is always connected.

- *IMU*: Inertial Measurement Unit (accelerometer, gyroscope)
- *Host*: NFC reader or USB host (computer)
- *Device*: attached sensor device; Aquabit.

4.2 FIRST SEAWEED MONITORING SYSTEM PROTOTYPE

The seaweed monitoring system developed to meet the defined system requirements consists of a battery powered wireless smart sensing system with an accelerometer, light, pressure and temperature sensors, microcontroller, and RFID front-end with coil antenna for communications. As a communications mechanism for data transfer, Low-frequency RFID was chosen due to its immunity to the identified adverse effects that other communication methods exhibit underwater, such as multipath propagation as described in Chapter 3. When data transfer is initiated by the user, the coil antenna can harvest energy from the field generated by the reader, powering up the tag. An added benefit is the compatibility of the system with existing PIT tag readers already used in aquaculture [20]. The following Figure 12 shows the proposed ideal system.

Since the accelerometer will be continuously operating to acquire data around the movement underwater of the seaweed, it requires a battery to keep it running. The microcontroller used to control the system, manage power, and process data has to have low-power consumption. In addition, the processor also has to be capable of floating-point operations as the data analytics required involve calculating variances – which require square-root calculation – and angle and rotation calculations – which involve trigonometric functions. This allows the device to correctly process the data collected and enables autonomous behaviour through edge analytic algorithms carried out on the

datasets to contextualise behaviour of the seaweed monitor. This functionality and edge analytics capability could be used also to carry out embedded processing of data to reduce communications over head.

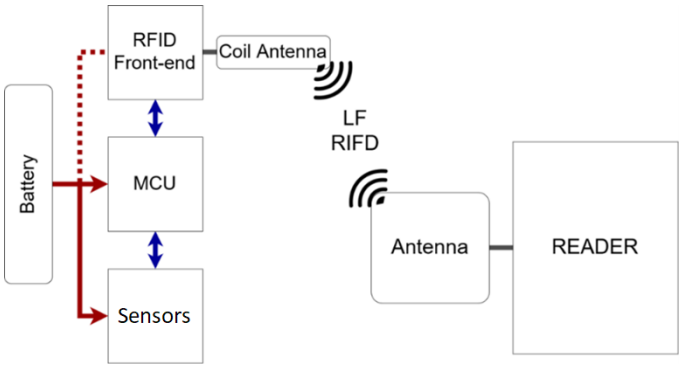

Figure 12 - Block diagram of proposed attached sensor system.

4.2.1 First Prototype design

The first prototype of the system was developed to better understand the integration of the system, and the functionality of each component. As no initial evaluation boards for the technologies chosen on which to build to sensor system existed for near-field RFID at the desired frequency, the first prototype would allow us to better understand the RFID front-end chosen and how it would integrate with the other components. The first prototype was designed using Altium designer for manufacture test and system characterisation, and to inform the subsequent miniaturised and optimised sensing system for deployment in the pilot sites.

The first task was to find a COTS RFID front-end that could work as a bridge between the wireless communication link and the microcontroller unit (MCU). To act as a bridge between the existing PIT tag reader currently in use in aquaculture activities and the microcontroller, the RFID front-end needs to have the specified:

- Low-frequency (LF) RFID (134 kHz)
- Serial wired communication interface (e.g., I2C, SPI, 2-wire, etc)

The selected COTS semiconductor that met these requirements was the TMS37157 [121] from Texas Instruments. It is a low-power LF RFID transponder interface with an internal EEPROM of 121 bytes and a SPI interface for EEPROM access and data exchange with the RF field. The TMS37157 communicates with a LF RFID reader via a Half-Duplex (HDX) Interface. It can be entirely powered via the RF link, not requiring any external power. It is also able to harvest energy from the LF RFID field and supply it to the rest of the circuit (maximum 16 mA).

A first-generation prototype evaluation board was designed and developed to test and characterise the RFID chip selected (no evaluation kits were available from the supplier). This prototype board measured 3 cm x 5 cm. The main objective of this evaluation board was to test the RFID chip front-end selected, test its communication protocol and establish its compatibility with standard RFID systems commonly used in the marine environment such as the PIT tag system by Biomark [30] in use at the Marine Institute costal pilot site which was the envisaged demonstration site for the technology [122].

The following figure shows a block diagram of the evaluation board developed. To facilitate the test and characterisation of the system, additional functionality was added to the board, such as an external non-volatile memory, a USB connector, and additional interfaces such as LEDs, buttons, and connectors. The following Figure 13 shows a block diagram of the evaluation board system.

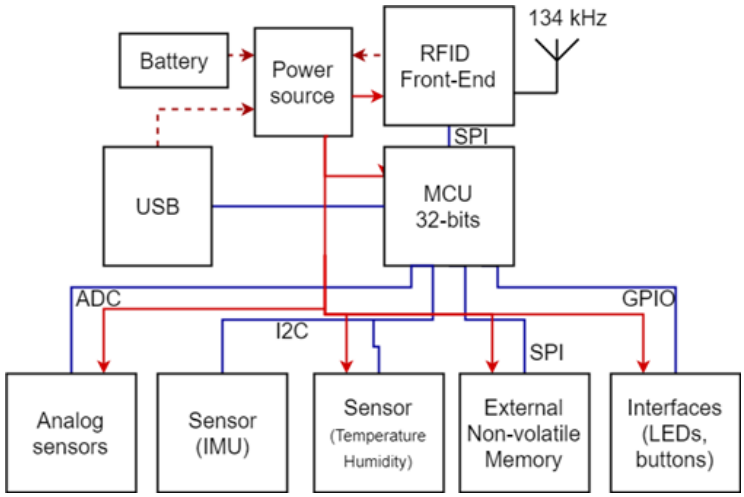

Figure 13 - Evaluation board block diagram for the attached sensor.

The RFID front-end TMS37157 requires an external antenna with a resonance circuit capacitor. According to the datasheet [121], the antenna needs to have an inductance of 2.66 *mH* and a quality factor of 60. From the TMS37157 documentation on the Texas Instruments website, one of the application notes [123] analyses the performance with off-the-shelf antenna coils from Neosid [124]. Therefore, the coil antenna selected for this board was the Neosid 32 KA.

The microcontroller unit (MCU) selected for this board was the STM32L452 from STMicroelectronics. It is a low-power 32-bit ARM Cortex-M4 MCU with floating-point unit (FPU). It was selected due to its very low power consumption, the presence of FPU and DSP instructions to speed up complex algorithms, and the ease of use of the STM32 MCU line [125].

An external non-volatile memory was added to store collected data. The memory selected was the AT45DB641E serial flash from Adesto Technologies. The sensors added to the evaluation board were an IMU (LSM6DS3HTR – STMicroelectronics) to log motion and acceleration data and a temperature/humidity sensor (HTS221 – STMicroelectronics). An additional connector was placed on the board to allow the user to add another two analog sensors to the Analog-Digital Converter (ADC) of the MCU. Three LEDs and

two buttons were also added to the board to interact with the RFID Front-End and the MCU. These buttons had functionalities to reset the device or send a user signal to the MCU.

For a wired communication to an external host, a USB type-C connector was added to the circuit, connected to the USB peripheral on the MCU. The USB connection was also used as a possible power source for the circuit.

Multiple power sources options were added to the circuit. The 5V supply from the USB connector was regulated down to 2V with a linear low drop-out (LDO) regulator. A battery was added so that the system could operate wireless. The battery selected was a coin-cell CR2025 (3V). To better utilise the battery lifetime, the whole system is operational at 2V. This enables the battery to discharge up to 1V before the system stops operating. The LDO used has a dropout of less than 50 mV for output currents under 50 mA (the current the prototype consumes is less than 10 mA, discussed in the next section). 2V was selected, and not 1.8V which is a common value for embedded circuits, because the RFID front-end TMS37157 requires a minimum external power source of 2V.

To test the different power sources available and evaluate how they could interact and affect the system, a row of jumper connectors was placed on the board to select the power source for both the whole system except the RFID front-end (called VCC) and the RFID front-end external power source pin (called VBAT_RF). The power options for VBAT_RF were either the regulated battery voltage or the regulated USB voltage (at 2V). Power options for VCC were the regulated USB voltage, the regulated battery voltage, or the power output from TMS37157 (called VBATI). This allowed the testing of the TMS37157 as regards its capability to provide power to the system while in an RFID field.

4.2.2 First Prototype characterisation and testing

The designed prototype embedded system which presents a size of 5 x 3 cm (approx. 1/3 of a credit card) is shown in Figure 14 below. The system was tested operates in conjunction with the evaluation module reader kit MRD2EVM [115] (Texas Instruments) pictured in Figure 15.

Figure 14 - Evaluation IMPAQT PCB of tag fabricated, front and back respectively.

Figure 15 - COTS Reader module

The testing done for the first prototype had the following objectives: (1) characterising the read range achieved with the LF RFID front-end; (2) determine an approximate power consumption of the system so this can be improved in the next version; (3) test the different power supply options and how they interact with each other (such as determining if the energy harvesting output from the RFID font-end was able to power the whole device); (4) study how data transmission is done between reader and tag (as

no evaluation kit for the RFID front-end was available); (5) determine if the RFID front-end was fully compatible with the PIT tags in use in the aquaculture farms.

The evaluation board read range with the MRD2EVM (reader antenna length of 5 cm) is 5 to 10 cm depending on the coil antenna orientation. This range is mainly dependent on reader antenna size and power.

The current consumption of the developed evaluation board is, at maximum power, 3.8 mA from a 5V power source (USB connection). This was measured with the MCU in run mode, USB, sensors, external memory, and RFID turned on. When operating from the battery, power saving mode can be turned on for almost all components.

The current configuration of the tag requires that the reader sends a command requesting data from the tag. In the MRD2EVM documentation [115], this command is called MSP Access. The test system consists of a PC communicating via USB / COM port connection to the reader, sending the frame referent to the *MSP Access* command. The MRD2EVM reader then manages the downlink connection to the tag, providing the magnetic field to power up the RFID front-end and sending and receiving data. At the end of this exchange, the MRD2EVM sends the reply of the tag via the USB communication to the PC. *Each exchange* can transmit 6 bytes to and from the tag. The MSP access command format sent to the MRD2EVM can be found in the MRD2EVM documentation [115] on table 780.

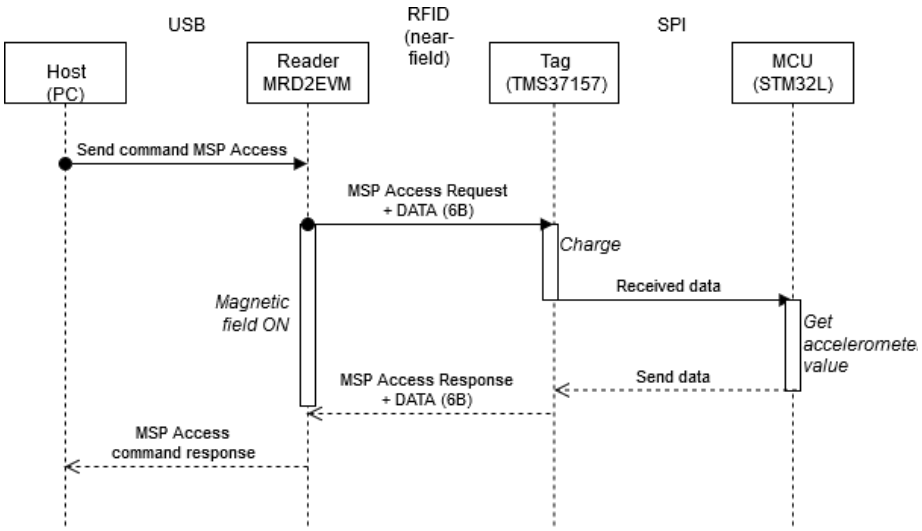

Figure 16 - Exchange sequence for the MSP Access command

The main drawback of this system is that the MSP Access command can only send 6 bytes and receive 6 bytes from the tag. Added to this, a timeout for the MSP Access command needs to be specified in the MSP Access command if any response is expected from the tag. During testing, a timeout lower than 500ms made the communication link unreliable. This means that the data transfer rate for the system would be around 12 bits per second, which is too low to be useful for data download involving large quantities of data.

An experiment was designed for the MRD2EVM evaluation reader kit to measure its magnetic field strength at different distances. As described in chapter 3, section 3.5, , the Anritsu MS2038C VNA Master vector network analyser [113] and the 100C probe [114] from Beehive Electronics, USA were used to measure the magnetic field strength at the system's resonant frequency (134.2 kHz). The MRD2EVM reader evaluation kit antenna is a square loop antenna embedded on the printed circuit board, with sides of length 3.0 cm and 14 turns. The magnetic field strength generated by this reader was measured in different underwater conditions and is shown in Figure 8 in Chapter 3, section 3.5.

To demonstrate the functionality of the system in operation, the evaluation board turns on when the battery (CR2025) or the power supply (USB) is connected. The RFID tag (evaluation board) front-end transmits 6 bytes back to the reader every time the reader makes a request. These bytes are the current value that the IMU is reading. These 6 bytes are organized as follows:

```
| ACC Z MSB | ACC Z LSB | ACC Y MSB | ACC Y LSB |
ACC X MSB | ACC X LSB |
```

The accelerometer is configured to read +-4g, so the resolution for these values is 0.122 mg per LSB (g being the gravity acceleration).

The next step involved testing the compatibility of the evaluation board with the PIT tag readers from the Marine Institute. Two systems were tested: a large-scale PIT tag antenna reader system that is used in fish cages underwater and a small handheld PIT tag reader (Biomark 601 Reader), both from Biomark and able to read HDX and FDX PIT tags (compatible with ISO 11784 and ISO 11785). However, both systems were not able to read either the ID number of the TMS37157 or any other memory contents. It was established that, although the reader and tag are compatible on the physical layer [121], [126], the TMS37157 uses a proprietary protocol which is different to the ones standardised for animal identification (ISO 11784 and ISO 11785) used by PIT tags, and therefore not compatible with those systems.

4.3 FINAL SEAWEED MONITORING SYSTEM PROTOTYPE

Since the LF RFID front-end was not compatible with the PIT tag readers and had a very low data transfer rate, it was decided to change the RFID link to a High-Frequency (HF) RFID front-end. Although it has a lower read range than the LF RFID system, the HF RFID has a higher variety of off-the-shelf solutions, is compatible with multiple devices, including NFC-enabled smartphones and has a comparatively high data transmission rate. The final

system prototype, then, would be developed to interface with standard RFID/NFC technology using a smartphone as a standard reader aligned with the end use case envisaged where the seaweed farm operators would download the data from the sensor system as part of scheduled maintenance activities for the seaweed and lines.

The final device system prototype was designed as represented in the Figure 17, using the final requirements compiled earlier in this chapter. For easier referencing, the system is separated into subsystem building blocks:

- *Power*: subsystem responsible for providing power, battery management, turning the system on and off, and voltage protections and regulations.
- *Connectors*: USB-C connector for battery charging and communication with PC host and a programming connector for the microcontroller.
- *Communication* (comms): Subsystem responsible for the NFC/RFID communication with host.
- *Sensors*: Contains the sensing capabilities of the system (motion, pressure, temperature, and light).
- *Control*: Subsystem that contains the microcontroller (responsible for the control of the whole system) and the external memory to store data collected.

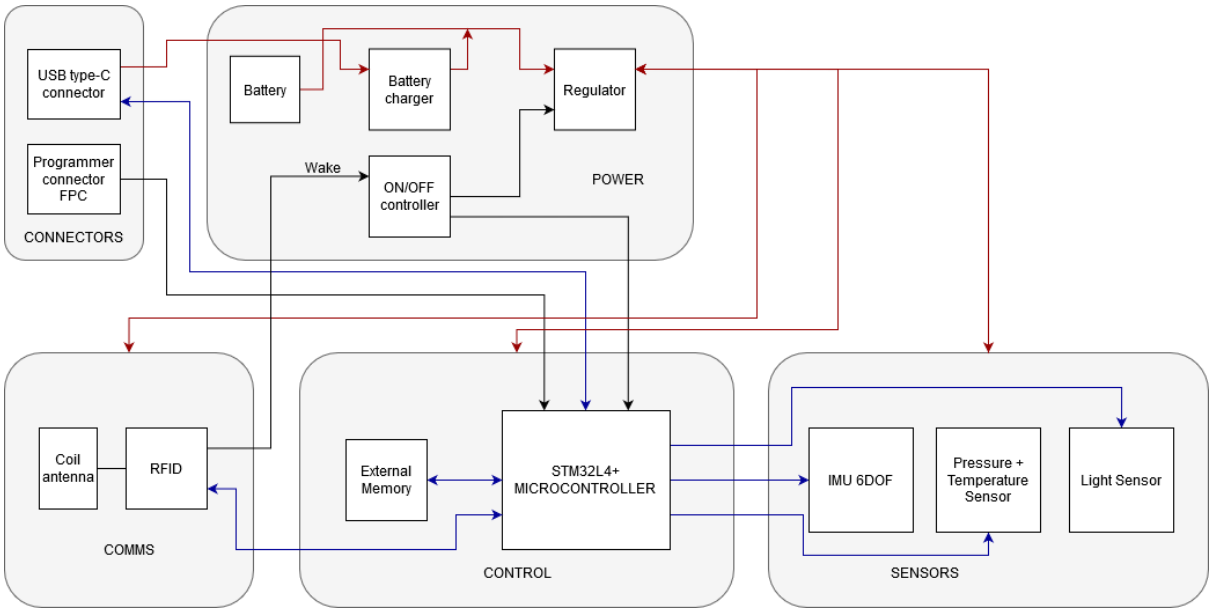

Figure 17 - System block diagram of attached sensor device

4.3.1 Circuit Design

When selecting the components for the system, the main constraints were size, power consumption and compatibility with the other components. The main constraint was to keep the device size close or smaller than 15 x 50 x 10 mm, the approximate size of the biggest commercially available fish tags (such as the DST centi-HRT ACT by Star-Oddi, Iceland [127], or the MCFT3 [128] by Lotek, Canada).

Firstly the main components identified in the system block diagram in Figure 17 were selected and listed in .

Table VI - List of the components for the main functionalities of the device, with their respective parameters, in order: Part Number, minimum input voltage, maximum input voltage, package (footprint), area, height, current consumption on sleep or low power mode (in μA), maximum and typical current consumption (in mA).

Component	Part number	V min	V max	Package	Area (mm x mm)	Height (mm)	Sleep (uA)	Max. (mA)	Typ. (mA)
MCU	STM32L4R5QII6	1.71	3.6	UFBGA132	7.0 x 7.0	0.45	2.8	30	18
IMU	LSM6DSOXTR	1.71	3.6	LGA-14L	2.5 x 3.0	0.83	3	1	0.55
P+T Sens	MS583730BA01-50	1.5	3.6	Module 3.3	3.3 x 3.3	2.75	0.01	1.25	0.02
Light Sens	TCS3472	2.7	3.6	FN-6	2.0 x 2.4	0.65	2.5	0.33	0.24
Mem	MT29F8G01ADAFD12-IT:F TR	2.7	3.6	TBGA	6.0 x 8.0	1.1	50	62	0.5
RFID	ST25DV04K-JFR6L3	1.8	5.5	WLCSP10	1.65 x 1.5	0.33	2	0.3	0.076

The selection process for each of these components was as follows:

1. On an electronic components distributor (such as Digikey[1]), a list of available components for that category (e.g. light sensor, IMU, etc) was found.
2. Using the website filters, the smallest packages (size and footprint) available were selected, which resulted in a small list of components.
3. From those, each component's datasheet was consulted to find the power consumption and other relevant specifications of the device. This was compiled in a list of potential components for each category.
4. From this list, the component which had the best trade-off between size and power consumption (and other specific parameters for each category) was chosen.

[1] https://www.digikey.com/

The details on what specifications were used in the selection process for the components in each subsection is detailed in subsections 4.3.1.1 to 4.3.1.4.

The shows the list of the components selected as the main functions of the system: the microcontroller (MCU), the inertial measurement unit (IMU) for movement sensing, the pressure and temperature sensor (P+T Sens) which needs to interface with the water, the light/colour sensor (Light Sens), the external memory (Mem), and the NFC RFID front-end (RFID).

4.3.1.1 Power subsystem

Due to the size constraints defined for the seaweed monitoring system as well as the need to maximise the operational lifetime for the seaweed sensor, the battery technology chosen was lithium-ion polymer (LiPo) due to its small size to power ratio characteristics. The additional benefit of this type of battery is the small weight and the rechargeability. The nominal voltage of a LiPo battery cell is approximately 3.7 V, so it can be used to power integrated circuits in the 3.0-3.3 V range, which increases the number of available sensors that are compatible with the system voltage. We chose 3.0 V (instead of the 3.3 V commonly used) as the main voltage of the circuit to extend the power-on time, letting the battery discharge as much as possible.

From the list of main components selected in , an estimate of the power consumption of the system was calculated taking in consideration a sampling rate for the sensors of 1 Hz and 52 Hz for the IMU. The time to program the external flash memory was also calculated (as it was the component with the highest instantaneous current draw). From this, the calculated average instantaneous power consumption was approximately 3 mW. Given this, we wanted to find the smallest LiPo battery possible with a capacity bigger than 100 mAh (equivalent to 3 days of deployment for the scenario calculated).

From a list of possible LiPo battery sizes, we searched for batteries manufactured and their capacity, compiling a list of possible sizes and capacities, shown in Table VII. The battery with the best trade-off in size and capacity is a 300mAh capacity battery with dimensions of approximately 30 mm x 12 mm x 6.5 mm. Higher capacity batteries were too big and the resulting system size would be bigger than intended.

Table VII - List of LiPo batteries found, their capacity and dimensions.

Capacity (mAh)	**Dimensions (mm x mm x mm)**	**Area (mm^2)**
130	10 x 35 x 5	350
190	10 x 40 x 5.5	400
450	11 x 48 x 6	528
300	12 x 30 x 5	360
300	12 x 35 x 6	420
220	12 x 40 x 5	480
260	12 x 40 x 6	480
500	13 x 50 x 8	650
500	13 x 50 x 8	650

The battery chosen has an integrated management system embedded which protects the battery from over-discharge, overcharge, and short circuits.

A battery charger IC was added to the design to control the charging of the battery over the USB connector. The IC used for this is the BQ25100 [129], which has a small footprint, allows the configuration of the charging current via an external resistor connected to one of its pins, and it has a pin input for a thermistor to enable thermal shutdown in case of a high temperature being

sensed. The charging current for the battery was set to 250 mA as a safety measure, as the maximum safe charge current for the battery is 1C (300mA).

The battery is always connected and powers the whole system when in normal and sleep modes via the system low-dropout regulator (LDO). To conserve battery when not in the data collection mode, the device has a shutdown mode that supplies power only to the wake-up subsystem and the real-time clock system in the MCU. This is done via a separate LDO that is always on. The main system LDO is off when in shutdown mode, effectively reducing battery drain when the device is not in use. Both LDOs are the TPS7A0230PDQNR [130], selected due to the small footprint and the very low dropout in the output. Both are fixed to regulate the voltage to 3.0V.

An ON/OFF controller [131] was added to the design to manage the system shutdown by turning on and off the main system LDO. The controller turns on the main system power regulator according to the occurrence of one of two events: (1) a low logic level on its PB input pin (which represents a wake-up signal from the NFC application), or (2) by monitoring an external voltage source (connecting the device to a USB host). The circuit was designed so that the GPIO pin output from the NFC chip creates an interrupt signal on the PB pin when it detects any RF activity (i.e., the presence of an NFC reader). The external voltage monitored is the USB bus, and therefore whenever the device is connected to a USB host, the system is also turned on. The ON/OFF controller has an input that can be used to shutdown the system via a KILL command. This input is connected to the MCU which is then able to turn off the main system voltage. The controller also has an interrupt that is connected to the MCU and a pin that indicates which type of wake-up event happened (USB or RFID). The ON/OFF controller used is the LTC2955CDDB-1.

4.3.1.2 Sensors' subsystem

The sensors chosen for the device were selected to be as small form factor as possible, with very low power consumption and compatibility with the system voltage of 3.0 V. Another factor that was considered as part of the sensor selection is the configurability of the sensor according to different needs and the resolution of the sensor measurement taken.

The motion sensor used in the system is the LSM6DSOX [132], which integrates a 3D accelerometer and a 3D gyroscope in a very small package with very low power consumption and low noise. This module has an internal FIFO buffer to store up to 3 kbytes of data while the controller is in sleep (low power consumption) mode. The measurements then can be transferred to the controller all at once, minimizing power consumption. The IC also has an embedded machine learning core that can be used to filter and detect features in the motion data, reducing the processing needed in the controller. The IMU is connected to the MCU by a SPI bus, and its two interrupt lines are also connected to GPIO pins in the MCU.

For temperature and pressure sensing, the MS5837-30BA [133] was chosen due to the very small form factor and it being optimised for water depth measurements. It has a resolution of 0.2 cm in water and provides low power consumption characteristics. The pressure sensing opening is built for chemical endurance in harsh liquid media (such as seawater), and it can be made watertight using an O-ring. In addition to pressure sensing, it provides temperature sensing as well.

For light/lux sensing, the target sensor is a photosynthetically active radiation (PAR) sensor commonly used in aquaculture monitoring, that measures the light intensity with wavelengths between 400 nm and 700 nm, which corresponds to the light spectrum range that is used for photosynthesis [57]. Since commercially available PAR sensors, such as the Li-COR [62]

(considered the gold standard for such application's [134]), are expensive and too big to be integrated into the device small package, a colour + clear light sensor with embedded IR (infrared) blocking filter was selected (part number TCS3472) [135]. A colour sensor with IR filter was preferred due to the possibility of correlating the RGB channel values with PAR sensors, as some authors such as Rajendran et al. [136] have done. In addition, it has a clear (white light) channel that correlates with the lux values. The sensor chosen has programmable integration time and gain, which allows it to measure values in different light intensity environments. Other key factors are the very small size and the low power consumption.

Both the pressure and the colour sensor are connected to the MCU via the same I2C bus, with 10kOhms pull-ups in the lines for each sensor which allows them to be addressed independently.

4.3.1.3 Control subsystem

A microcontroller (MCU) was added to the design to control and manage the whole system, transfer data from sensors to external memory, and communicate with hosts. The requirements for the MCU include low power consumption, small size, large RAM, enough peripherals for all the sensors and external circuits, and floating-point operation with sufficient processing capability for any required data analytics. The MCU chosen was the STM32L4R5QII6 [137, p. 32], due to its low power, machine learning compatibility and high CoreMark and ULPMark scores [138], [139] compared to other MCUs of same power consumption.

The data collected needs to be time-stamped to be correlated with other external sensors. To track time internally in the MCU, we used the Real-Time Clock function that requires an accurate clock source. For this, we added a 32.768 kHz low-speed external crystal to act as the clock source. No high-speed

crystal is needed, as the USB module in the MCU can synthesise the needed frequency from the low-speed clock using its internal PLL. This also saves energy, as the higher speed external crystal requires more power to operate.

To make sure there is enough memory for data storage to save all sensor data collected in any long-term deployments, the SPI Flash memory with the largest memory size possible was selected. For a serial SPI Flash, the largest memory capacity available in a commercial off-the-shelf IC is 1 GB. The memory used in this design is the *MT29F8G01ADAFD12-IT:FTR* [140]. The memory consumes a considerable amount of power when on, so a very small and low-power consumption load switch (part number TPS22901YFPR [141, p. 22]) was added to its power supply pin and the firmware needs to make sure to turn on and off (duty cycle) the external memory only when needed.

4.3.1.4 Communication subsystem

To communicate, download data collected, and wake-up the system, two communication interfaces are present in the device design: (1) a wired interface using a USB type C connector, and (2) a wireless communication interface using NFC/RFID at 13.56 MHz

The USB connection is used to communicate with the MCU, download data, configure the system, update the firmware and wake-up the system. USB was chosen because of its ease of use and compatibility with any personal computer and laptops. The USB connector selected is waterproof with an O-ring around its external chassis, which adds a layer of protection to the device when using it in wet areas. The MCU includes a USB peripheral in its chip, which makes the integration easier. The USB is also used to provide the power to the device, powering the main system voltage and/or charging the battery.

A small FFC/FPC connector was included to allow direct programming of the MCU and debug capabilities. This connector is used with a specifically

developed Interface Board for STM32 microcontrollers, which connects the board in development to a STLink programmer via a smaller connector than the standard STLink. The Interface Board also contains a FTDI UART to USB converter to allow easier debugging via UART.

Near-field communication (NFC) is a standard of communication on the high-frequency (HF) RFID at 13.56 MHz. The low attenuation of RF signals underwater still applies at this frequency, but it has more attenuation than the 134.2 kHz system described in the previous evaluation board (section 4.2). However, the NFC standard is widely used today, and a great number of modern smartphones have an NFC reader/writer controller embedded to be used as a smart wallet. This can then be leveraged to be an easily accessible and operable reader for the device.

The interface for the NFC communications chosen was the ST25DV chip transponder [142], which in addition to having an internal EEPROM, also can communicate via a mailbox system that can transmit up to 256 bytes per message on demand. This mailbox system (also called Fast Transfer Mode in the ST25DV datasheet [142]) works as follows: the ST25DV acts as a bridge between the NFC reader (RF communication) and the MCU (via I2C serial interface), where each interface can deposit a message in the ST25DV mailbox and the ST25DV notifies the other interface that a message has arrived. For messages going from the RF interface to the MCU, the notification occurs via a GPIO output from the ST25DV or by polling the ST25DV MB_CTRL register. For messages going the other way (from MCU to RF interface), the NFC reader must poll the MB_CTRL register. This makes the communication between reader and transponder more efficient, as there is no need to read/write to the internal EEPROM. However, the message sender must always check if there is a message already in the mailbox before writing to it, otherwise the old message is lost, as the mailbox is the same for both directions (making this

communication interface half-duplex). This custom fast transfer mode has a transmission rate of up to 26 Kbit/s.

The ST25DV chip also has an energy harvesting function, and a general-purpose input/output (GPIO) pin that can be programmed to wake-up the system when a message is received. Communication with the reader can be carried out without the need for a battery, so the power requirement for wireless transmission is only on the reader.

The GPIO feature is used in the wake-up circuit, such that the ST25DV pulls the GPO line high and this, in turn, signals to the ON/OFF controller to turn on the main system LDO. However, the GPIO pin needs to be powered via the V_{DCG} pin to output its signal (pulling the line logically high). Therefore, the chip is always provided with battery power directly from the battery LDO to the V_{DCG} pin for the wake-up functionality. The input leakage current from the V_{DCG} pin is lower than 0.1 μA, which is very low and would not drain the battery in the power-off mode.

To enable power transfer and NFC communication, an external antenna tuned to 13.56 MHz needs to be connected to the ST25DV chip AC0 and AC1 pins, which have an internal capacitance of 28.5 pF [142] that needs to be accounted for in the antenna design. The antenna design is explained in detail in section 4.3.3. To connect the antenna to the main PCB, a small FPC connector [143] was placed at the edge of the board, and the antenna flex PCB was designed with a ribbon that fits the connector selected.

4.3.2 PCB design

The full schematics can be seen in the Appendix I. The PCB design was carried out using the software Altium Designer. It provides ready to use PCB footprints for many components, and those were used when available. Nevertheless, all the footprints were inspected to verify if they followed the

recommended footprint in their respective datasheets. Part numbers for which the footprint was not available were designed according to the datasheet of the component.

All passive components, such as resistors and capacitors, where chosen to be SMD standard size 0201 for the purposes of system miniaturisation. The exceptions to this are the antenna capacitors, which were left unpopulated and with size 0402 for easier hand soldering in case the antenna impedance needed tunning – this is explained in detail in Section 4.3.3. All pull-up resistor values were calculated to be the maximum possible value so as to minimise system power consumption without compromising the required voltages for each pin. Every resistor's power (P=V*I) was calculated to check if the dissipation of the 0201 package was enough.

The PCB outline and size were designed to match the battery size, with a small space added on the bigger dimension to place the USB connector. In this way, the battery sits right behind the USB connector in the bottom side of the PCB and defines the overall shape and size of the seaweed sensors. No components apart from the USB connector are placed on the bottom side so that the battery is not in danger of being perforated by any component as this would pose a safety hazard due to the chemistry inherent in Lithium batteries. The battery is connected to the main PCB via two solder pads, designed to minimize the connection size and footprint. The system floor plan and overall 3D placement of all components (PCB with sensors, rechargeable LiPo battery, and FPC Antenna) inside the enclosure can be seen in the following Figure 18:

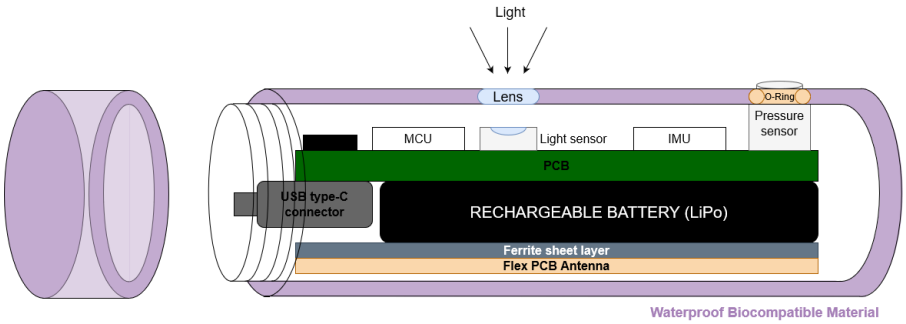

Figure 18 - Initial block diagram of the 3D design of the device

The PCB was designed with 4 metal layers – top, bottom, power and GND. The PCB layer stackup (shown in Figure 19) and the rules for clearance were provided by ECS Circuits [144] according to their fabrication standards as they were the manufacturer of choice for this system. The layer information is presented in the figure below. Microvias were used due to the small size of the board, with microvias in pad added below some BGA components for system reliability and manufacturability reasons. The impedance of the USB DP and DM lines were matched using the Altium Designer Differential Pair option.

#	Name	Material	Type	Weight	Thickness	Dk	Df
	Top Overlay		Overlay				
	Top Solder	Solder Resist	Solder Mask		0.01mm	3.5	
1	Top Layer		Signal	1oz	0.036mm		
	Dielectric 2	PP-001	Prepreg		0.051mm	3.9	0.02
	Dielectric 4	PP-001	Prepreg		0.051mm	3.9	0.02
2	GND	CF-004	Signal	1oz	0.035mm		
	Dielectric 1	FR-4	Dielectric		0.32mm	4.8	
3	Power	CF-004	Signal	1oz	0.035mm		
	Dielectric 3	PP-001	Prepreg		0.051mm	3.9	0.02
	Dielectric 5	PP-001	Prepreg		0.051mm	3.9	0.02
4	Bottom Layer		Signal	1oz	0.036mm		
	Bottom Solder	Solder Resist	Solder Mask		0.01mm	3.5	
	Bottom Overlay		Overlay				

Figure 19 - Layer configuration and stackup used in calculating the impedance of tracks.

The IMU was placed so that it was close to the centre of the board and had balanced copper traces coming out of its pins to reduce mechanical deformities due to thermal expansion and contraction of the tracks that would affect its readings. The pressure and light sensors were placed centrally on the other

end of the board from the USB connector to allow better readings and easier placement of the clear lens for the light sensor and the pressure sensor interface. The decoupling capacitors were placed as close as possible to the power pins of their respective ICs to reduce high-frequency noise (from the switching circuits) and act as a temporary local power supply in case of sudden drops in power (when the power consumption spikes).

The power lines were designed with extra tolerance: the minimum width was 0.254 mm (while normal signal tracks had a minimum of approximately 0.08mm), but a higher width was used where possible (especially for the VCC and GND tracks). This is done so that their intrinsic resistance is as low as possible, which greatly decreases the current loss due to ohmic heating. The copper trace resistance is proportional to its length and inversely proportional to its cross-section area [145]:

$$R = \rho \frac{l}{A} \qquad 51$$

Where ρ is the resistivity of the material, l is the length, and A is the cross-section area. The cross-section area for the trace is a rectangle consisting of the trace width and trace thickness as height. Therefore, the trace intrinsic resistance is lower with a higher trace width.

The thermal power dissipation in this process is described in the following Equation 52:

$$P \propto I^2 R \qquad 52$$

Where P represents the power lost as heat, I is the current flowing through the track and R is the intrinsic resistance. Since the power traces conduct much higher current than the signal traces, the extra width added to the power traces helps decrease the power lost as heat when conducting the current. To this

end, we also added copper heat sinks on the power pins in the LDOs and the battery charger to better dissipate the heat.

A ground copper plane was added on all signal and power layers, with a dedicated ground layer connecting to the other planes using stitching vias. This was done to better dissipate the heat via the copper and decrease the impedance of the GND path for return current. The switching signals on the PCB need a small inductance path to return as this reduces noise and interference with other signals; and the power currents need a small resistance path to close the loop to the power supply, reducing losses.

The Figure 20 below shows the final PCB design in 3D.

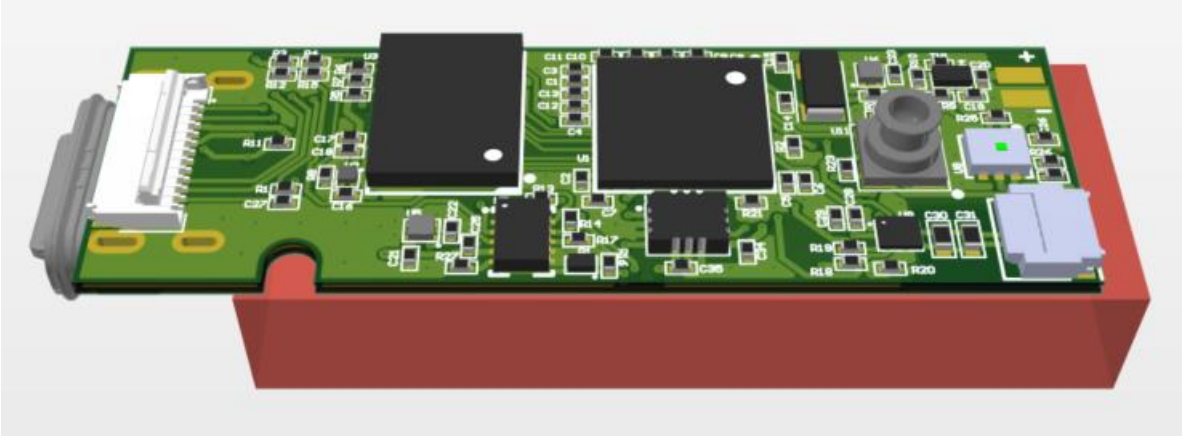

Figure 20 - 3D view of the PCB designed. The only component placed in the bottom layer is the USB connector. The orange box represents the battery placement in the bottom layer.

4.3.3 Antenna design

The antenna was designed to be a flexible printed circuit board that connects to the main PCB via a FPC connector. A flexible printed circuit (FPC) board was chosen for the antenna due to its small thickness, reducing the space needed to place the antenna inside the device. Its size (excluding the connection cable) is 40 x 13 mm and this was chosen aligned to the overall PCB and battery size. The antenna parameters were designed using ST Antenna

eDesign Suite [146] to match the expected impedance for the NFC chip used in the design (ST25DVxxx). To design the antenna and calculate its parameters, the procedure described in the application notes for this device was followed [147]. Firstly, since the antenna had a size restriction, those were the fixed parameters on the design software. The number of turns, trace width, and trace separation size were adjusted so that the total inductance of the antenna came as close to the resonant value as possible. Figure 21 shows the pattern design for the rectangular antenna.

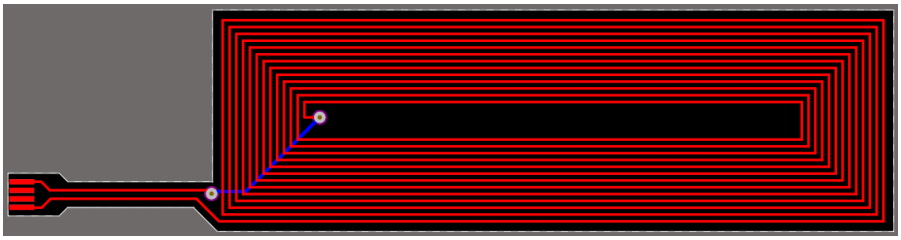

Figure 21 - Flexible PCB design for the antenna.

The internal capacitance of the NFC chip used (ST25DVxxx) for the antenna pins is 28.5 pF. To make a resonant antenna at the 13.56 MHz frequency, one can use the Equation 53 to determine the inductance of the antenna.

$$X = 2\pi f L_{ant} + \frac{1}{2\pi f C_{int}} = 0 \qquad 53$$

From the Equation 53, we calculate the required antenna inductance to be L = 4.83 μH. Using the ST Antenna eDesign Suite, the parameters for conductor width and spacing were calculated for the chosen antenna size, but due to the small size, a compromise was needed on the inductance value. The antenna inductance calculated from the design was L = 4.88 μH. Due to fabrication tolerances and errors, the actual inductance value could be different. To make it resonant at 13.56 MHz, the PCB was designed with space to solder a capacitor in parallel with the antenna to complete the resonant circuit. This

would add another capacitance to the complete impedance X shown in Equation 54, which should be 0 for a resonant circuit at the desired frequency.

$$X = 2\pi f L_{ant} + \frac{1}{2\pi f C_{int}} + \frac{1}{2\pi f C_{par}} = 0 \qquad 54$$

Once fabricated, the antenna inductance was measured using a VNA to confirm that the antenna was fabricated correctly and to the desired standard. The VNA measured the impedance of the antenna at 13.56 MHz and the result can be seen in Figure 22.

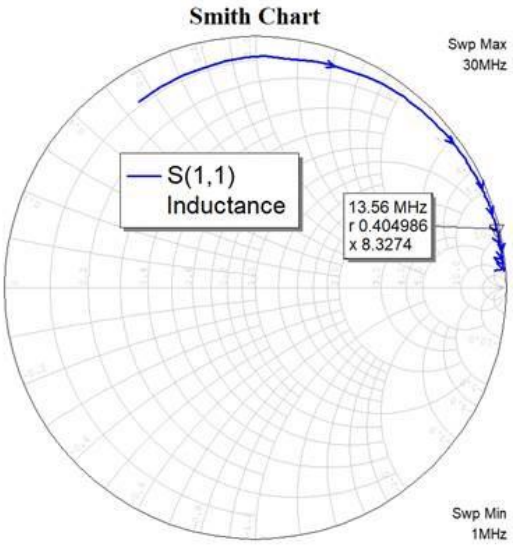

Figure 22 - Fabricated antenna measured Smith Chart and measured impedance at 13.56 MHz.

Converting the impedance $Z = 0.41 + 8.32\ j$ measured by the VNA at 13.56 MHz, we find that the inductance of the antenna is indeed 4.88 μH. Therefore, the capacitance needed in parallel to complete the resonant circuit is described below in equations 55 and 56:

$$C = C_{int} - \frac{1}{(2\pi f)^2 L_{ant}} \qquad 55$$

$$C = 28.5\,pF - 28.23\,pF = 0.27\,pF \qquad 56$$

This value was found to be negligible, so no additional capacitor is needed.

4.3.4 Enclosure design

The enclosure was designed using the PCB 3D model and the battery size (dimensions of approximately 30 mm x 12 mm x 6.5 mm) as base sizes. As can be seen in Figure 23, Figure 24, and Figure 25 below, a screw-on cap designed to be waterproof when deployed is used to access the USB-C connector (the USB-C connector selected is also IP rated for additional safety). The back of the enclosure is designed with relief details to aid the attachment to the seaweed/kelp leaf using glue, as seen in Figure 24. Figure 23 shows the front side with the openings for the pressure sensor and the light sensor. The whole enclosure is waterproofed by using gaskets and the screws as seen in Figure 25, as well as using a polyurethane resin (PUR) inside the device to protect the electronics from water ingress.

The holes on the sides provide a space to thread a line securing the device to the mooring lines in the farm. This is needed to make sure the device is not lost and becomes an environment pollutant unintentionally.

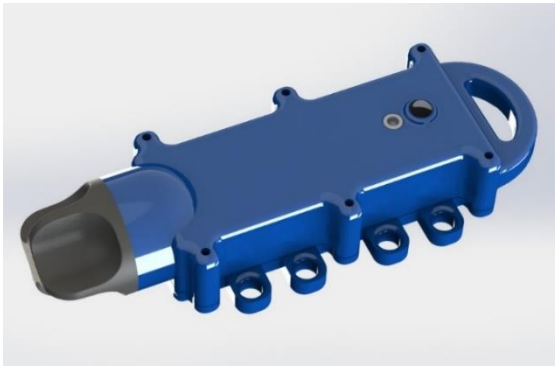

Figure 23 - Front view of the enclosure with openings for pressure and light sensor.

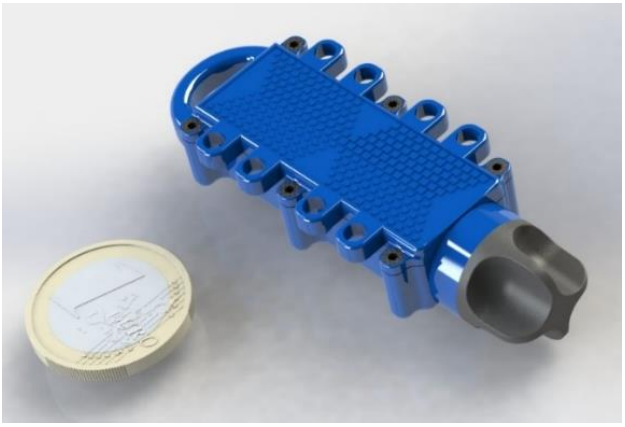

Figure 24 - Back view of the enclosure with details in relief for glue adherence to seaweed.

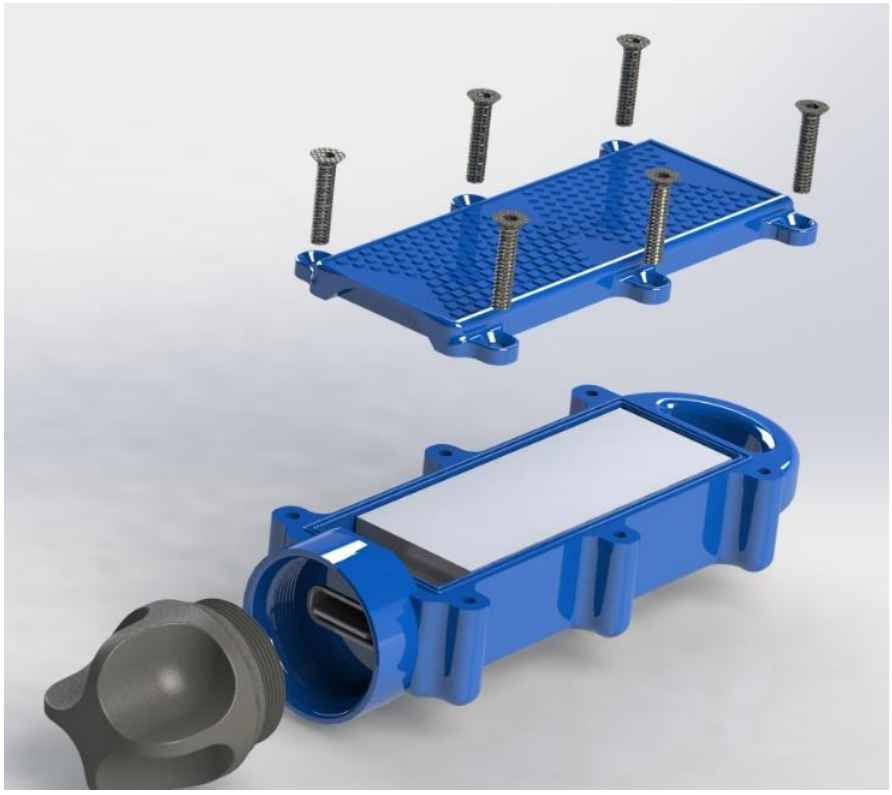

Figure 25 - Exploded view of the enclosure. The round black part unscrews for access to USB connector.

The enclosure was 3D printed using Low Force Stereolithography (LFS) using a Formlabs Form 3 3D printer [148] (Formlabs, MA, USA). This process was used due to the high quality and refined details produced, creating a waterproof enclosure. The material used in the printing is the "Durable Resin" [149] (which has similar physical properties to polypropylene (PP) or high

density polyethylene (HDPE)), as it results in an enclosure plastic that is waterproof and more resistant than standard polylatic acid (PLA) used in other 3D printers. PLA or acrylonitrile butadiene styrene (ABS) were not used because they create a printed surface with small imperfections that would allow water to enter the enclosure.

After the enclosure was printed, the PCB was placed inside, attaching, in the process, the O-ring for the pressure sensor and a fine glass tubing for the colour sensor. This process was facilitated due to the small notch made in the PCB (show in Figure 20) at the bottom left corner. The notch was designed to align the placement of the PCB inside the enclosure.

After this process, the polyurethane resin (PUR) was mixed and injected into the enclosure, and this resin was left curing for 24 hours.

4.3.5 Firmware development and operation modes of the seaweed sensor

The Aquabit sensor device has three modes of operation: shutdown, sleep and normal mode. During shutdown, all the components are turned off, with the exception of the NFC chip, the ON/OFF controller and the RTC (real-time clock) on the microcontroller. The device remains in shutdown mode until a wake-up condition is met – i.e., when the NFC reader sends a wake-up command to the ST25DV, pulling its output pin high. After the wake up signal the device goes to the normal state and can communicate with the USB host or the NFC reader. The shutdown mode can be entered via sending a turn-off command to the device via either the NFC or the USB communication links.

During normal operation, the device is either communicating with the USB host or the NFC reader, or the device is collecting sensor data. Otherwise, the device enters the sleep mode to save battery power while still waking up

periodically to collect the sensor data. Figure 26 shows the modes of operation and the transition between these states.

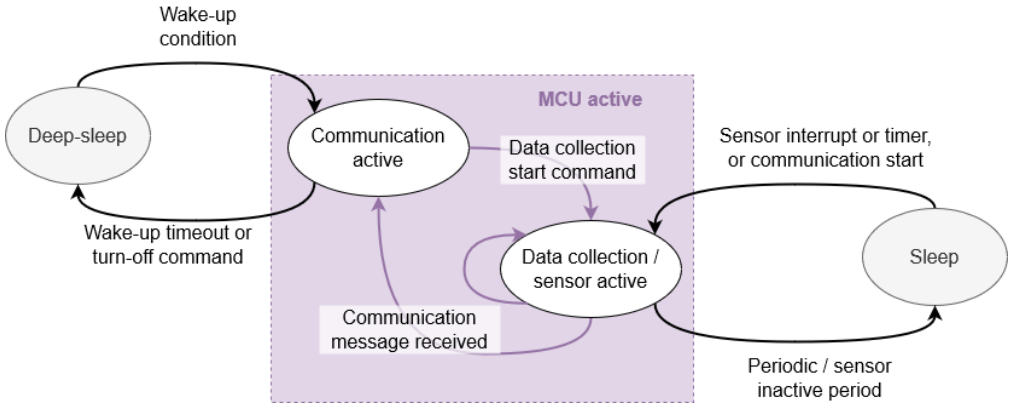

Figure 26 - State machine of the operation modes of the device.

The shutdown wake-up conditions are:

- NFC field/message from NFC reader.
- USB connection to PC host.

In these conditions, the device will wait for any message from the respective communication channel. In the case of the USB connection, the device is always ON as the USB powers the battery charger. In the case of the NFC field being used to wake-up, the NFC host application needs to send a wake-up command turning the GPIO output of the ST25DV chip high.

To start data collection, the respective command needs to be sent to the device. During data collection from the sensors, the read data is saved in a buffer inside the MCU memory. To reduce power consumption, the MCU only writes the data collected in the external flash memory when this buffer is full. In this way, the external memory is turned off for most of the time, and only turned on during transfers. If the device is configured to collect data, the sensor data collection subroutine should be running even while it is communicating with a host. To optimize the battery life, STM32CUBEMX Battery life estimator has been used. To specify the timing requirements of the estimator, the clock

counter of the Data Watchpoint and Trace (DWT) unit of STM32 has been used. To minimize the battery power consumption, all non-essential peripherals got disabled, the microcontroller set to run at 16MHz to minimize the current consumption of the CPU. In Figure 27, the STM32CubeMX Battery life estimator is shown. This can be used to calculate estimated battery lifetime under different modes of operation.

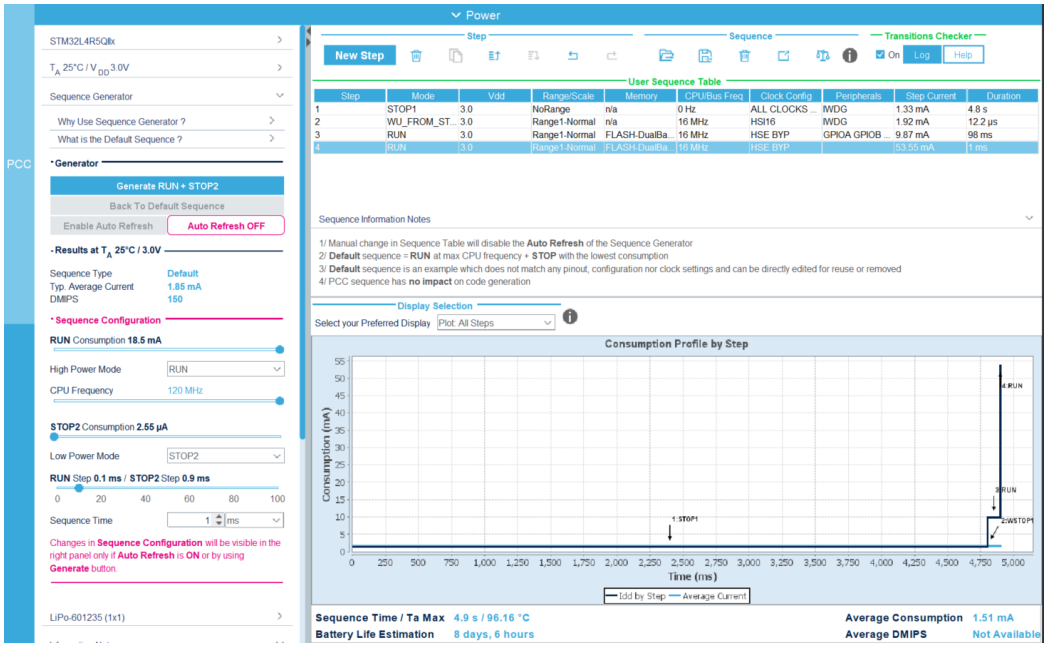

Figure 27 - Power consumption profile calculated by STMCubeMX battery life estimator.

4.3.6 Communication protocol used by the sensor device

The device has two communication channels: USB connection and the NFC link to the reader. The low-level communication protocol for each of the channels is dependent on the particular technology. The high-level protocol (user messages and procedure) used for both channels is the same.

4.3.6.1 NFC communication low-level specification and protocol

This communication link is based on the ST25DV chip by STMicroelectronics. It follows the ISO/IEC 15693 or NFC Forum Type 5 specifications for RFID proximity transponders [142].

The channel physics for the NFC channel is explained in Chapter 3 and summarised below. Basically, the transponder (ST25DV chip) and the reader function as a pair of coupled inductors. The reader generates an electromagnetic field from its antenna, that is captured by the transponder antenna, powering the transponder and sending data via modulation. This takes place in the near-field region of the electromagnetic field generated by the reader, hence the protocol name "Near-Field Communication". The reader generates an oscillating electromagnetic field at 13.56 MHz that consists mainly of an alternating magnetic field; almost no power is actually radiated in the form of electromagnetic waves (with an oscillating electric field). Generally, the communication distance is approximately 10 cm, and this is defined by the power level available for the reader antenna and the antenna size.

For the reader to be able to read and communicate with the transponder, a minimum value of electromagnetic field strength needs to be generated so that the reader antenna is able to pick up the field and use its power. In the case of the ST25DV chip (and active transponders in general), power is transferred from the RF operating field to the chip by rectifying the AC voltage generated in the transponder antenna. This rectified voltage is then filtered and regulated internally in the ST25DV chip, powering up its NFC communication capabilities.

For the ST25DV chip (and generally any transponder that follows the ISO/IEC 15693), the communications take place via a 13.56 MHz carrier electromagnetic wave generated by the NFC reader, on which the incoming data is modulated via Amplitude Shift Keying (ASK). The modulation is of 10% or 100% of the amplitude of the wave – signifying a zero or a one, respectively; with a data rate of 1.6 Kbits/s (using 1/256 pulse coding mode) or 26 Kbits/s (using ¼ pulse coding mode). The outgoing data generated by the ST25DV chip is modulated

using load modulation using Manchester coding, with one or two subcarrier frequencies at 423 kHz and 484 kHz.

The transmission protocol between the ST25DV and the NFC reader is based on the reader initiating every message transaction. This means that the ST25DV starts transmitting only after receiving a valid request from the reader. Each request and response are contained in frames. More details about this protocol can be found in the ST25DV datasheet [142]. This protocol includes low-level RF and ST25DV management messages (such as EEPROM read/write, ST25DV register read/write, and ST25DV GPIO output), and the fast mailbox transfer, which is used to transmit the high-level messages between the host (NFC reader) and the device.

4.3.6.2 USB low-level specification and protocol

The USB communication is carried out using a four-wire cable that is attached to the USB-C connector. It is based on the USB 2.0 specification [150], which is the version supported by the particular STM32 MCU selected. The USB host is defined as the external device that initiates the communication (e.g. a PC), while the USB device is the attached sensor device (the system described here). The signalling is done on the two wires (DP and DN) with full-speed bit rate of 12 Mbit/s.

The USB low-level protocol is implemented in the firmware using the STM32 USB Communications Device Class library. When connected to a PC, this library automatically sends the needed information to the Operating System and it, in turn, opens the communication channel to the device via a Virtual Serial Port.

4.3.6.3 High-level protocol

This high-level protocol encompasses the rules and the messages transmitted between *host* (USB host or NFC reader) and the *Aquabit device* (the system

described here). This protocol is the same for both communication channels; the message is transferred between host and device using the fast transfer mode mailbox in case of the RFID channel, and the USB Virtual Serial Port in the USB channel.

In this protocol, the host always communicates first. This means that every message transaction is initiated by a request sent from the host and ended with a reply from the device or a timeout. The device never sends a message without being requested to first. Commands that do not have a specified response must be replied to with an ACK response. Every message has a CRC (cyclic redundancy check) field to verify the integrity of the message. This is especially important during firmware updates, to ensure the uploaded firmware is not corrupted.

4.3.7 Host application

To communicate with the device once it is encapsulated – to wake it up, configure it, and to download data – two host applications were developed: (1) an Android application to be used in an NFC-enabled smartphone, and (2) a Windows software run on a PC or laptop.

The Android app was developed using the Software Development Kit (SDK) for the ST25DV [151] tag made available by STMicroelectronics. The application uses the SDK and the Android NFC libraries to communicate with the ST25DV tag using its custom commands according to its datasheet [142]. It can also communicate via the standard NFC Forum Type 5 standard commands as implemented by the SDK [151].

The application functionality is as follows: the user places the smartphone close to the device with the application open. The application reads the device configuration and enables the user to change it by showing the options on the screen. The user has the option to download the logged data and upload them

to the IMPAQT cloud severs, which can be used to visualize the data on the IMPAQT monitoring system (IMS). The uploading procedure is shown in Figure 9.

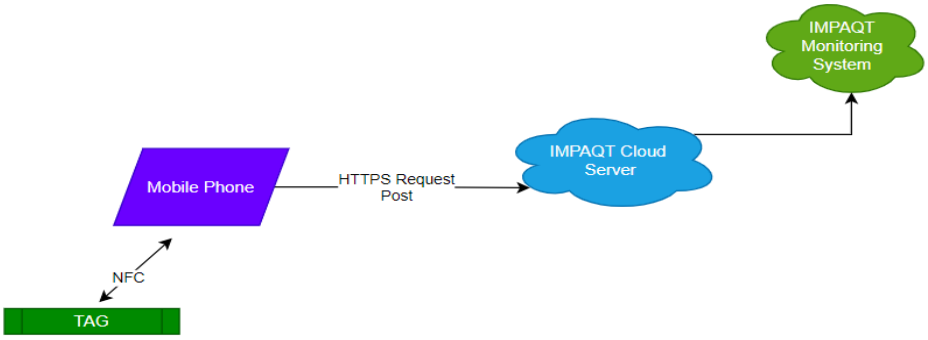

Figure 28 - Data upload procedure to the IMS for visualisation.

To communicate via USB, a Python 3.6 application was developed to work with the *pyusb* package [152] that provides a wrapper to USB functionality in Windows-32 environments. In the device side, the USB stack was set to function as a USB communications device class (CDC), using the library provided by STMicroelectronics for ST32L4 microcontrollers [153].

This Python application (hereafter called PyHost) is able to send commands to the device, update its internal real time clock, download data from the device internal memory. It also has debug capabilities and can update the firmware of the device without the access to the programmer connector.

5 SEAWEED SENSOR SYSTEM CHARACTERISATION RESULTS AND DATA COLLECTION

This chapter contains part of "Peres, C., Emam, M., Jafarzadeh, H., Belcastro, M. And O'Flynn B. (2021) 'Development of a low-power underwater NFC-enabled sensor device for seaweed monitoring', Sensors 2021, 21. https://doi.org/10.3390/s21144649"

5.1 INTRODUCTION

In this chapter is described the test and characterisation of the sensor device developed, as well as the results from these tests. We also show the protocol and results from the pilot prototype deployment in Lehanagh Pool (Bertraghboy Bay, Connemara, Ireland) in conjunction with the Marine Institute who are IMTA pilot site owners and project partners in the IMPAQT project.

5.2 IN LAB DEVICE CHARACTERISATION

The final embedded system has been fully characterised in Lab settings to ensure accurate measurements and data sets will be obtained when deployed in the seaweed farm associated with the IMPAQT project [43].

The Figure 29 shows the individual hardware components of the internal circuit. The battery connector was soldered into the battery pads of the PCB (top right on the PCB). The antenna FPC cable was connected into the antenna connector, and the whole system encapsulated in the enclosure using the polyurethane resin (PUR).

Figure 29 - From top to bottom, system components: battery, antenna, and PCB.

The complete encapsulated system is shown in Figure 30 with a 1-euro coin for scale.

Figure 30 - Final embedded system for seaweed monitoring encapsulated.

A general functionality test was also performed to determine system usability. The achieved read range for the NFC communication was dependent on the reader: different smartphones used provided different read distances. The maximum achieved distance in air was 5 cm.

5.2.1 Inertial Measurement Unit characterisation and calibration

To characterise and calibrate the Inertial Measurement Unit (IMU), a motion capture (MoCap) system was used. In this setup, the objective was to record

the movement internally using the IMU at the same time the MoCap system would record the tracked motion. Combining and correlating both would then prove the accuracy of the IMU system as regards tracking of motion parameter values in terms of rotation and accelerometry.

The MoCap system used consists of 10 infrared cameras by Optitrack (Prime^{X}13, NaturalPoint, Inc. DBA Optitrack, Corvallis, Oregon, US) [154] mounted in different positions, pointed at the same area. The positioning of the cameras in relation to the observed area can be seen in Figure 31. This system is designed to track the position of passive or active (IR-LEDs) markers placed in the object under observation and uses these markers to determine the position and orientation of the object in relation to global predetermined coordinates. Each camera has a 1.3MP resolution and its frame rate can be adjusted between 30 and 240 FPS. In this experiment, passive reflective markers of 12.5mm diameter were used. The cameras are connected to a computer using the Motive 2.2 software [155] that combines the data from the cameras to recreate the movement of the object being tracked. The MoCap system was calibrated according to the instructions of the manufacturer [156]. The calibration file was saved as it contains the calibration error necessary to assess the results.

The MoCap system was used in conjunction with a custom-made test structure consisting of a pendulum device with a gimbal platform attached to it. The system was put in movement by oscillating the pendulum while the gimbal was set to a specific orientation, so all 3 axes of the IMU were at least once the focus of the oscillation.

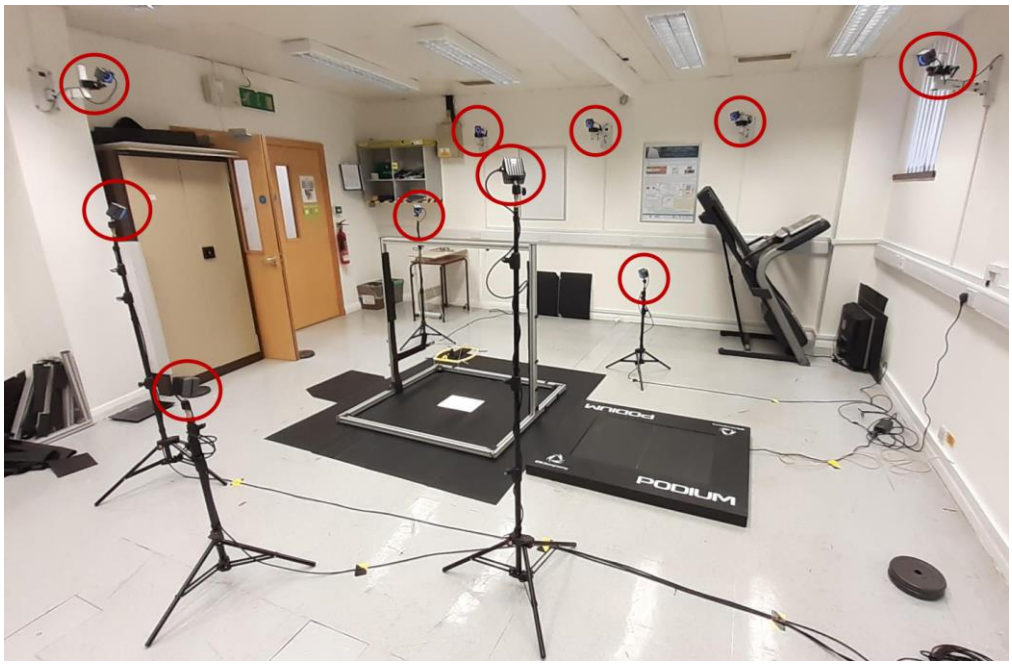

Figure 31 - Positioning of the MoCap system cameras in relation to the device. Cameras are highlighted with red circles.

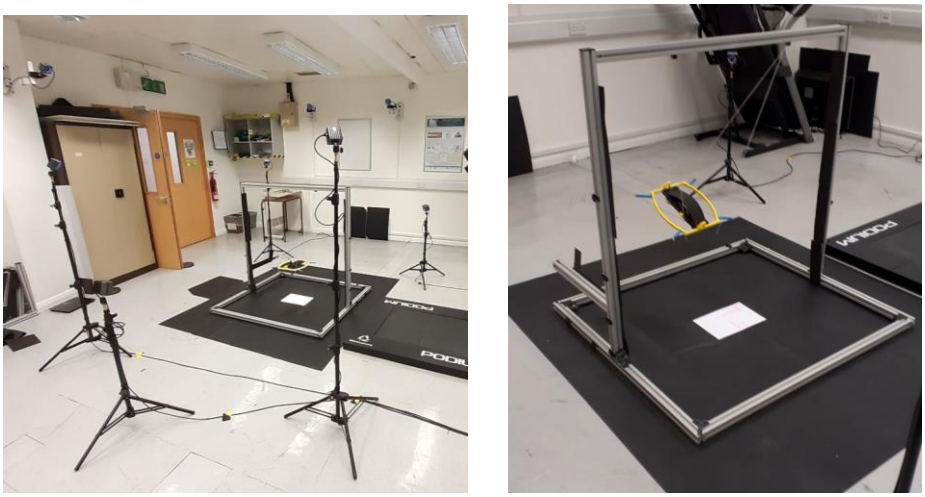

Figure 32 - (a) Pendulum in the area covered by the Optitrack cameras; (b) Pendulum mounted in the aluminium frame. The reflective markers were placed in the four courners of the pendulum base to track the oscillation of the whole system.

The custom-made swing is composed by 4 strings attached to the aluminium rig structure via bolts and nuts and a gimbal platform with 2 DoF. Figure 33 shows the detail photo of the gimbal platform where the device was placed with the passive reflective markers attached to the corners.

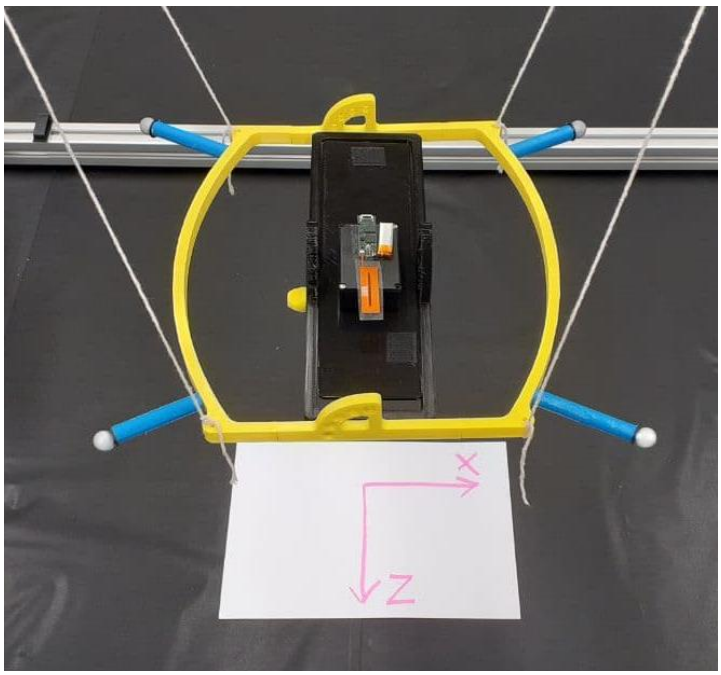

Figure 33 - Detail of the gimbal platform attached to the pendulum where the Aquabit device was placed for the motion tracking system test.

The procedure for the data capture was as follows:

1. The cameras' FPS was set to be the same as the sampling frequency of the IMU (100 Hz).
2. The device was configured with the time synchronisation parameters and the IMU sampling frequency via the NFC Android Application described in the previous section. Then, after placing the device in the specific orientation for the test, a start data recording command was sent to it.
3. In the Motive software, a recording was initiated, and the time was noted to be correlated with the data from the device.
4. The pendulum was pulled and then set free to oscillate until coming to a rest. This period was recorded in the Motive software and independently by the Aquabit device under test.
5. The saved data from the IMU was downloaded for comparison.

To compare the datasets from the MoCap system and the sensor device, all of them must be synchronised temporally, mapped to a same coordination frame, and they must represent a same physical quantity. The data collected from the Motive system is the *position* of the object under observation in the fixed coordination frame seen in Figure 33; and the data collected from the IMU sensor is the *acceleration* (direction and intensity) in the 3-axis of the sensor coordinates (X_{IMU}, Y_{IMU}, and Z_{IMU}). Therefore, the data from one of the systems needs to be transformed to the coordinates of the other. Let $\boldsymbol{M}(t)$ be the position in the $\hat{\boldsymbol{x}}$, $\hat{y}$, $\hat{z}$ coordinates of the Earth (Figure 33) as measured by the MoCap system. The values measured in each axis X(t), Y(t) and Z(t) are shown in Equation 57:

$$\boldsymbol{M}(t) = X(t)\hat{\boldsymbol{x}} + Y(t)\hat{\boldsymbol{y}} + Z(t)\hat{\boldsymbol{z}} \qquad 57$$

Therefore, we can find the acceleration of the object as measured by the MoCap system by taking the second order derivative in each axis, as shown in Equation 58:

$$a_{MoCap(t)} = \frac{d^2X(t)}{dt^2}\hat{\boldsymbol{x}} + \frac{d^2Y(t)}{dt^2}\hat{\boldsymbol{y}} + \frac{d^2Z(t)}{dt^2}\hat{\boldsymbol{z}} \qquad 58$$

We then assume the three axes of the device accelerometer to be aligned with the MoCap reference frame but rotated. The acceleration reference for the Aquabit sensor device output is shown in Figure 34.

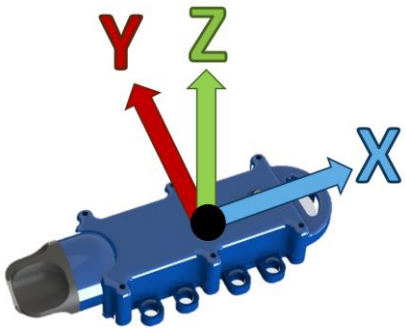

Figure 34 - IMU reference frame for the sensor device.

Therefore, the axis alignment are as follows:

$$\hat{x}_{MoCap} \equiv \hat{y}_{IMU} \quad 59$$

$$\hat{y}_{MoCap} \equiv \hat{z}_{IMU} \quad 60$$

$$\hat{z}_{MoCap} \equiv \hat{x}_{IMU} \quad 61$$

After the data collection, both the data exported from the Motive software and the data downloaded from the device were imported into MATLAB® [157]. Both time series were synchronised and then compared against each other, as seen on Figure 35.

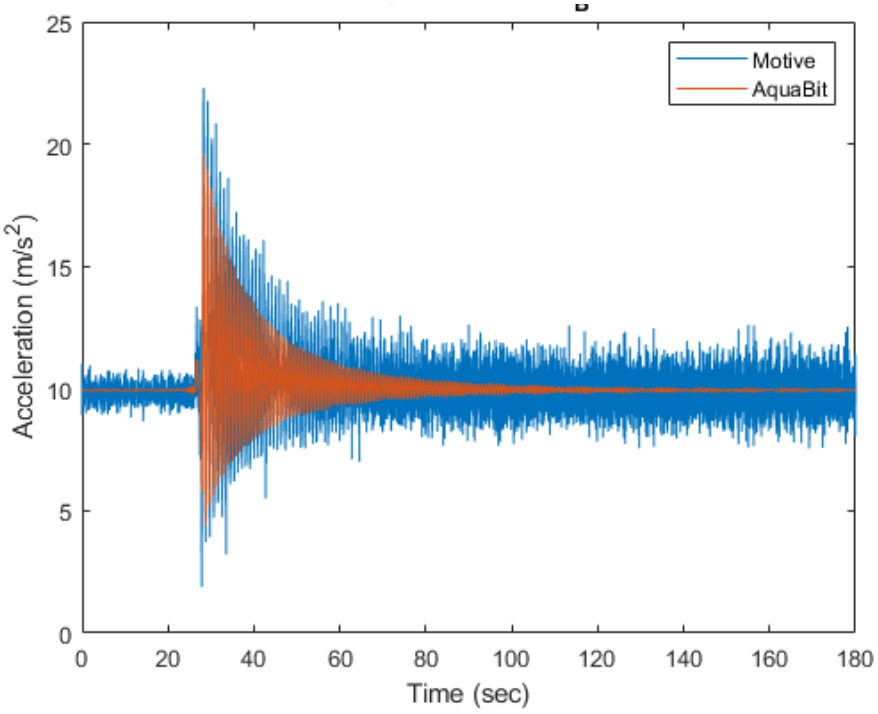

Figure 35 - Time series of acceleration axis captured by the Aquabit device and the Motive MoCap system.

The accuracy of test results has been limited by the time synchronisation for Aquabit and the MoCap. Since a timestamp needs to be transmitted to the Aquabit's internal RTC to synchronise its' time, and this process has delays (even if minimal due to the high-speed of USB communication), the timestamp for both systems could be delayed between each other. To minimise this delay, the Aquabit RTC was updated with the same timestamp source as the Motive

system (the PC where the Motive was running during the tests). The maximum delay expected was of 1s, but the actual delay measured (using the USB communication) was in the order of 100 ms.

In addition, the resolution of the Aquabit's RTC used for the test was 4 ms. The sampling frequency used for both the Aquabit IMU and the MoCap system was 104 Hz. A higher frequency was chosen as it enabled us to collect more information in the frequency spectrum, and the very small period between data points enabled a more fine-scale numerical derivative of the MoCap data for a more accurate comparison with the IMU.

The accuracy achieved by calibrating the MoCap system for the experiments had a mean error of 0.6 mm – i.e., the positioning error between the real position and the position calculated by the MoCap system had a mean difference of 0.6 mm. This value is calculated by the Motive software during its' calibration phase, where a 'wand' that has reflective markers with specified and fixed distances between each other is waved through the area covered by the Optitrack cameras. The MoCap software then aggregates the data collected by all the cameras and calculates the accuracy error (see Motive documentation for a more in-depth explanation of the calibration process [156]).

The results logged from this test can then be used to calibrate the IMU using the method explained in Kim and Golnaraghi [158].

5.2.2 Pressure sensor characterisation

For the pressure sensor characterisation, the device was placed in a pressure vessel with digital pressure gage (MTI DPGA12, Dwyer Instruments, Inc.) that monitored the pressure inside the vessel. The air pressure inside the vessel was increased in intervals of 5 psi each 3 minutes, up to 30 psi – which is approximately equivalent to a depth of 20 meters. The pressure was set

manually, and the Aquabit sensor system was set to log the pressure. The setup for this test is shown in Figure 36.

The results for the pressure test in air are shown in Figure 37. The blue line represents the pressure values measured by the gage, and the red line represent the measurements of Aquabit pressure sensor. The data logging for the pressure gauge (blue line) was done manually by observing the displayed value and writing it down. Due to this, no data is available for the transition periods between the different pressure plateaus.

As we can see in Figure 37, the difference between these two measurements is very low in various pressures, as the maximum error for all different pressure values is always lower than 6.9 Pa.

Figure 36 - Test setup for the pressure sensor test in water.

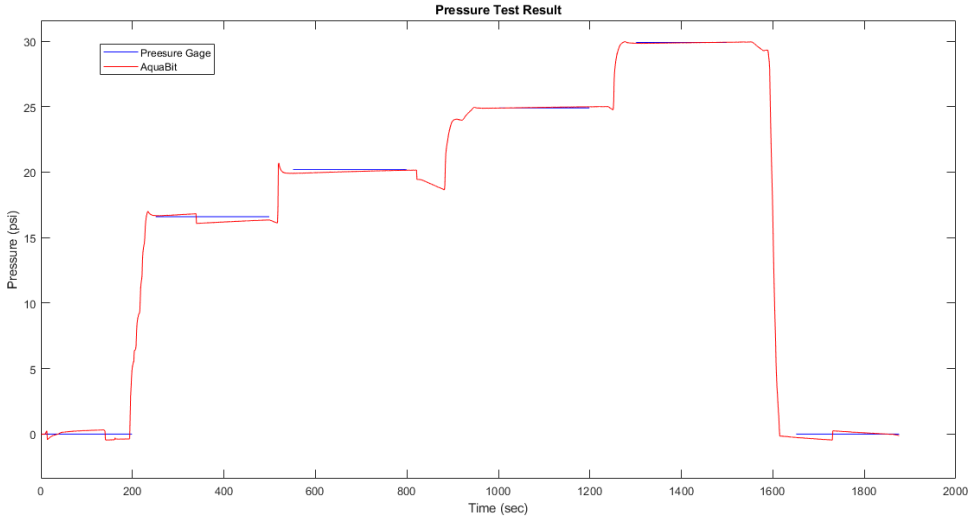

Figure 37 - Pressure sensor test in air result.

The same test procedure was repeated, but the device was placed in a container with water and completely submerged underwater. The results for the pressure test in water are shown in Figure 38.

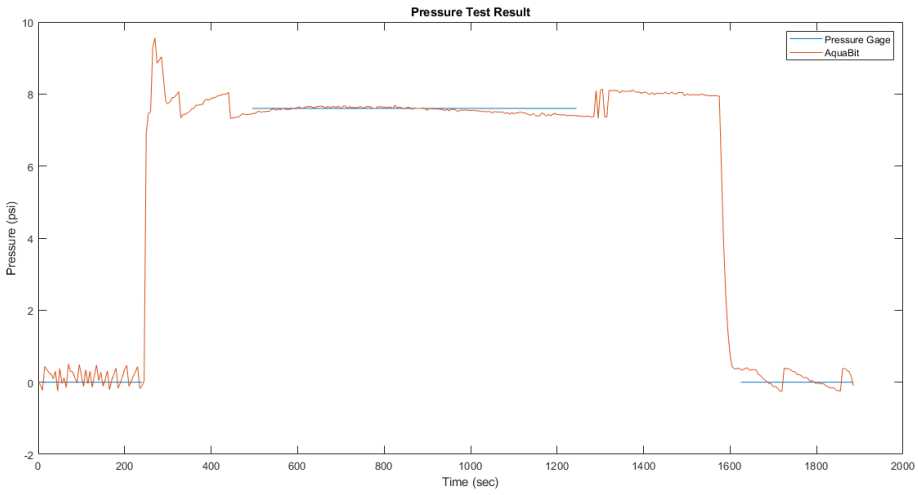

Figure 38 - Pressure sensor test in water result.

As shown in Figure 38, the difference between the blue lines, which represents the pressure measurements using a pressure gage, and the orange line, which represents the measurements using the pressure sensor on Aquabit, is very

small. The max error is 0.5 psi (3.4 Pa), that approximately simulates 5 m depth in sea water. It is worth noting that, measurements using the pressure gage have been done only when the pressure inside the pressure vessel was stable. The spike in the pressure measured by Aquabit between 200 s to 400 s is the normal overshoot happened during adjusting the pressure, as the pressure vessel had a manual adjustment.

5.2.3 Light sensor characterisation

To characterise the light sensor, the device was placed in different natural light conditions with a lux meter. The value read by the lux meter was manually noted and the device recorded the lux measurement read by the internal light sensor as shown in Figure 39 below.

Figure 39 - Light measurement calibration of Aquabit

5.2.4 Power consumption measurements

Since the strictest constraint in the device design was its size – to not interfere with seaweed motion and not cause seaweed breakage – the available battery capacity to this device is very limited. The biggest battery capacity found for the size was 300 mAh. Therefore, the battery lifetime is constrained by the battery size, the PCB design, the PCB components actual power consumption,

and power-efficient MCU programming. Since most of these parameters are hard to predict, there is no expected battery duration, and the objective was to make the device lifetime last as long as possible.

Also, since up until now we have done only initial trials, with the objective of collecting data to characterise the sensor device, the device may be programmed with a sampling frequency greater than necessary in real farm deployments. Future work may inform an optimum sampling rate and associated deployment time.

The power consumption of the Aquabit has been measured using a power analyser (N6705B DC Power Analyser) to establish how long the unit can be deployed for sampling using its internal battery. As is shown in Figure 40, the power analyser was on the battery emulator mode and was connected to the battery port of the unit.

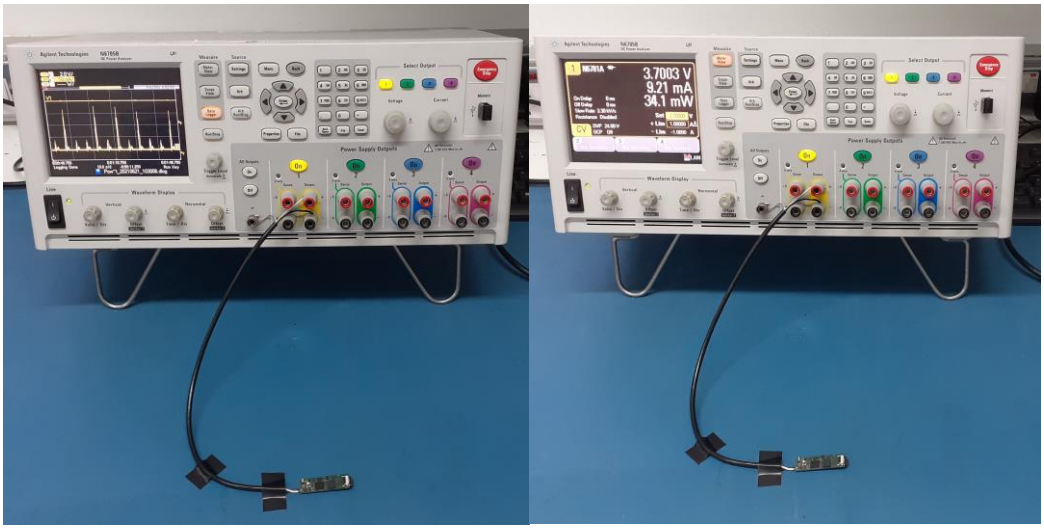

Figure 40 - Power consumption measurement of battery lifetime using a DC Power Analyser.

This battery emulator mode of the power analyser provides power to the device under study, but with a different current and voltage response compared to a standard DC output. A battery is not an ideal DC source due to

its internal state that varies depending on its current charge [145], [159]. Following this, the battery emulator mode of the power analyser sets an output resistance, so the output voltage varies with the load impedance, simulating a battery [160]. This provides more realistic results to the power consumption test.

The test results are shown in Figure 41 below:

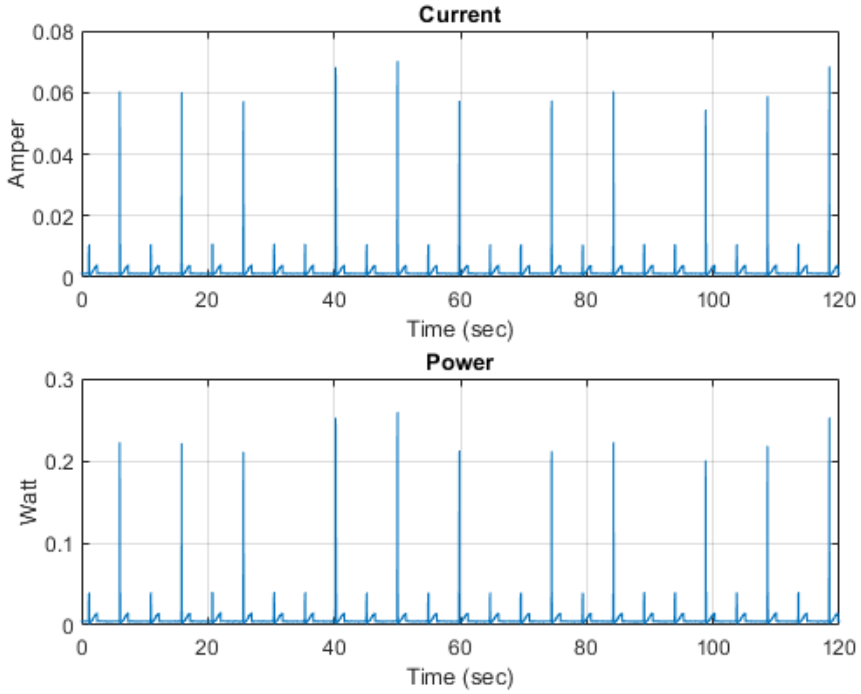

Figure 41 - Aquabit current and power consumption during sampling.

The power consumption of the Aquabit is very low (~ 1 mA) for most of the time since the unit is in sleep mode and it goes to higher values during the sampling, as is shown in Figure 41. A spike in the current consumption occurs every time the device leaves the sleep mode to sample data from the sensors, as expected. This, however, is very short in duration, and the device goes back into sleep mode after the sample is done. Some spikes are bigger than others due to data being save into the external memory. The external Flash memory was identified as one of the biggest consumers of power in the device during the circuit design. According to the Flash memory datasheet [140], the current

consumption during a write command is typically 44 mA, with a maximum of approximately 50 mA. This makes up most of the increase in current draw seen on the bigger spikes: the sampling procedures with writes to the external memory draw 0.06 A while the sampling procedures with no interactions with the memory draw approximately 0.01 A.

For the test shown in Figure 41, the device configuration was set to sample and log temperature, pressure, and light intensity each 5 s, and the IMU was configured to log acceleration and angular rate at 12.5 Hz. For this setup, the average of current and power consumptions are 1.6 mA and 5.7 mW. To calculate the battery lifetime, we can use the average current consumption and the battery capacity to get the number of hours the device can operate, according to Equation 62.

$$t(h) = \frac{C_{bat}(mAh)}{I_{avg}(mA)} \qquad 62$$

Since the battery has a capacity of 300 mA, the battery lifetime for the setup above (Figure 41) is 187.5 hours, or approximately 1 week.

The battery lifetime for the Aquabit depends on the sampling frequency set for the sensors, as a bigger interval between sampling would decrease the average current consumption. This is especially true for the motion sensor, as its current consumption in high-performance mode (which has a lower noise in the readings) is 0.55 mA; turning off the gyroscope drops the current consumption to 170 μA; and also setting the IMU in low-power mode drops the current consumption even further to approximately 26 μA (dependent on sampling frequency).

For most deployment cases where temperature, depth and light measurements are taken in bigger intervals (1 hour or more) the expected lifetime can be expanded. This can be configured to allow customization for

each deployment and study type. For example, aquaculture sites with maintenance schedules in which the site is visited less than once a week would need to set the sampling interval to each hour so the device can log as much data as possible before the next visit. On the other hand, shorter maintenance cycles allow a more frequent sampling.

5.3 DEVICE DEPLOYMENT AND PILOT SITE TRIALS

The device was sent to the Marine Institute for deployment in the aquaculture site in Bertraghboy Bay, Connemara, Co. Galway, Ireland (53°24'02.8"N 9°49'07.7"W) – henceforth called "Lehanagh Pool". The location can be seen in the maps shown in Figure 42. It is a fully licensed IMTA site, with production of Atlantic salmon (Salmo salar), Lump suckers (Cyclopterus lumpus), Wrasse (Labrus bergylta), Blue mussel (Mytlus edulis), Seaweed (Laminaria spp. (Brown sea-weed)). Figure 43 shows an aerial image of the IMTA site with circular fish cages and mooring points. It also shows a photo of the brown seaweed type produced there.

Figure 42 - Location of the Lehanagh Pool IMTA site. (Source: Google Maps)

Figure 43 – Aerial photograph of the IMTA site and photo of seaweed production. (Source: Marine Institute Ireland)

The Aquabit device was attached to an 'artificial seaweed' for this pilot trial. The pilot trial was not done by attaching the device to real seaweed due to the possibility of losing the device due to breakage suffered by the seaweed, which will be addressed by a future trial. The artificial seaweed is similar in length weight and physical appearance to the real seaweed attached to the seaweed lines on the farm.

The first objective of this pilot trial was to verify if the device enclosure was resistant to the harsh environment of the sea water. The test would be considered successful if the device remained operational during the whole deployment, and if no signs of damage or water entrance were detected. Secondly, we test if the attachment method was secure enough. The test would be considered successful if no device were lost, and if the attachment thread showed no signs of damage. Finally, we correlate the data logged by the device with other sensors deployed on the same site – namely the HOBO temperature and light sensor (Part Number UA-002-64, by Onset Computer Corporation, MA, USA) [63].

The 'artificial seaweed' used for the test are strips of plastic tarp designed to have similar hydrodynamics and texture of kelp. The Aquabit device was

attached to the 'artificial seaweed' using fishing nylon threads, firmly securing it to the 'artificial seaweed' blade as seen in Figure 43.

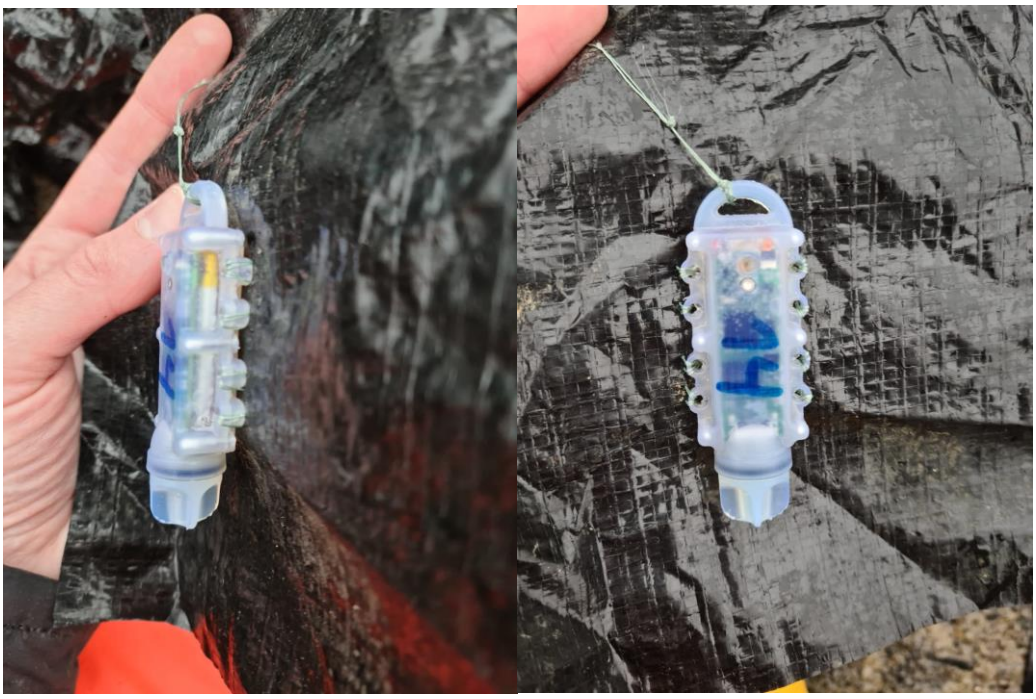

Figure 44 - Aquabit device attached to a 'fake seaweed' (plastic tarp cut to imitate seaweed) using fishing nylon threads.

The Aquabit device was then configured to sample motion (via the IMU), temperature, pressure, and light, using the Android app and the NFC communication link. The sampling frequency for the IMU was 12.5 Hz, while the other sensors had sampling frequency of 0.2 Hz (1 sample every 5 seconds). The artificial seaweed with the device was placed in the IMTA site on the 10-Jun-2021 and left there for a week.

Three devices were deployed in this manner, and all three were recovered with no visible damage. The recovered devices are shown in Figure 45. One of the devices' screw-on cap fell off during deployment, but due to the waterproof USB-C connector selected, no damage occurred to the electronics, and the device was still operational.

Two of the devices did not collect any data – one of them did not turn-on and the other was mistakenly turned off by the operator during the deployment. The other unit deployed collected data for a day before running out of battery. The data collected for temperature, pressure and light intensity is shown in Figure 46.

Figure 45 - Recovered Aquabit devices from deployment.

5.3.1 Data analysis of temperature and light logged and comparison with standard commercial sensor

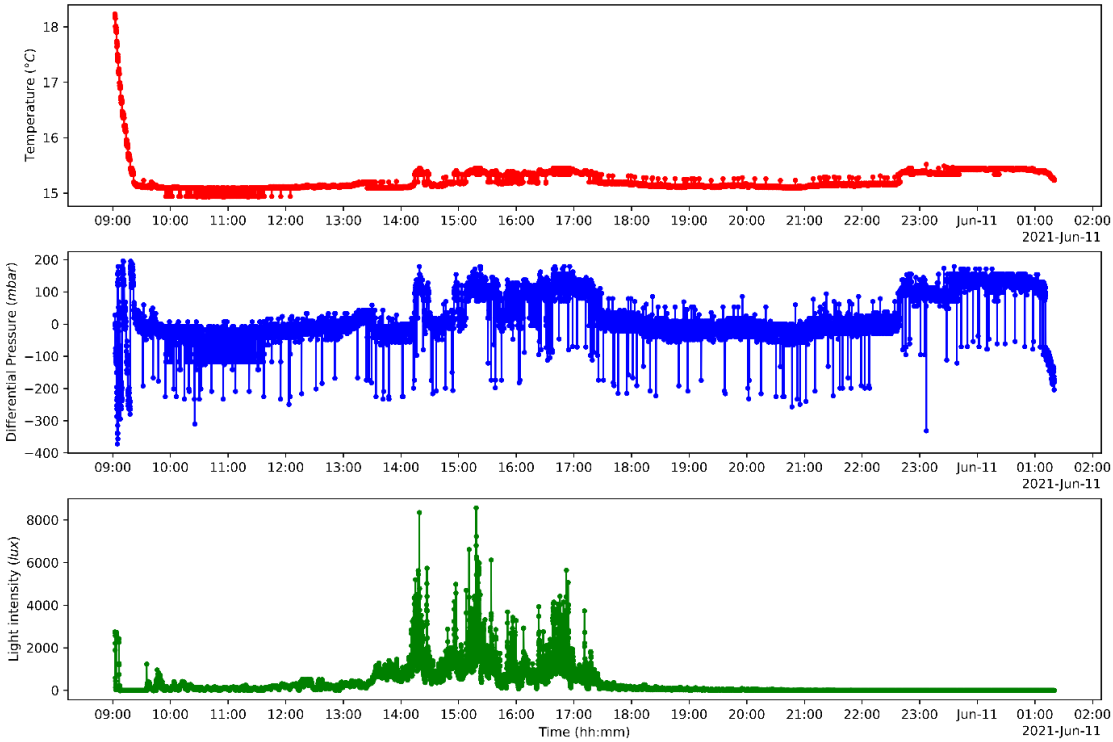

Figure 46 - Data recovered from Aquabit device for the deployment day of 10/Jun/2021.

For the following data analysis, the first 30 min of data were removed as those data points reflect the deployment activity, the manipulation and acclimation time, so the readings do not accurately represent the sea environment to be measured. Figure 47 shows the comparison between the data collected by the Aquabit (in red) and the other sensor deployed at the same site – the HOBO temperature and lux logger [63] (in blue). The HOBO sensor was configured to collect data every 10 minutes. The data shown for the Aquabit is the raw data – no processing was done, and no calibration values were applied. Even with no calibrations, it is possible to see that the temperature and light values follow the same trend.

To analyse and compare the two sensors, the Aquabit data was resampled to the same frequency as the HOBO sensor (1 sample each 10 minutes), and each data point represents the mean value of the logged data for those 10 minutes. The result is shown in Figure 48. These two measurement data series – HOBO measured temperature and Aquabit measured temperature – were statistically analysed and correlated using Pearson's R correlation. For the HOBO temperature sensor (here considered to be the 'gold standard'), the mean value read for the day was 14.76 °C with standard deviation of 0.18 °C. The Aquabit temperature sensor had a mean of 15.22 °C with a standard deviation of 0.18 °C. The similarities in the standard deviation imply that the variation of the measurement of the two sensors was similar.

The two measurements series have a correlation of $R = 0.646$ with p-value of $p < 0.001$. Therefore, it is possible to conclude that the two measurements are statistically significantly correlated. A scatter plot of the two measurements is shown in Figure 49.

The mean difference between the two values measured for the day was 0.44 °C, with a standard deviation of 0.14 °C. The root-mean-squared-error (RMSE)

between the two measurements was 0.465. We conclude that the two sensors are correlated.

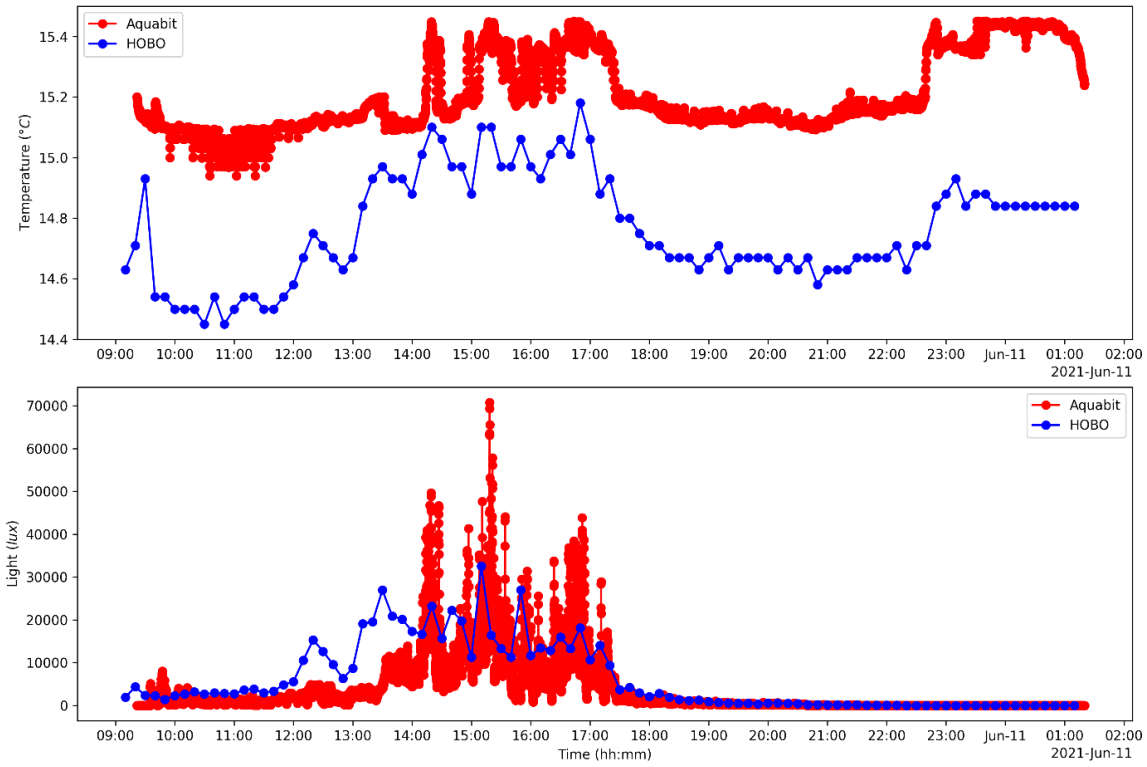

Figure 47 - Data comparison between Aquabit (in red) and the HOBO temperature and lux logger (in blue) deployed on the same site.

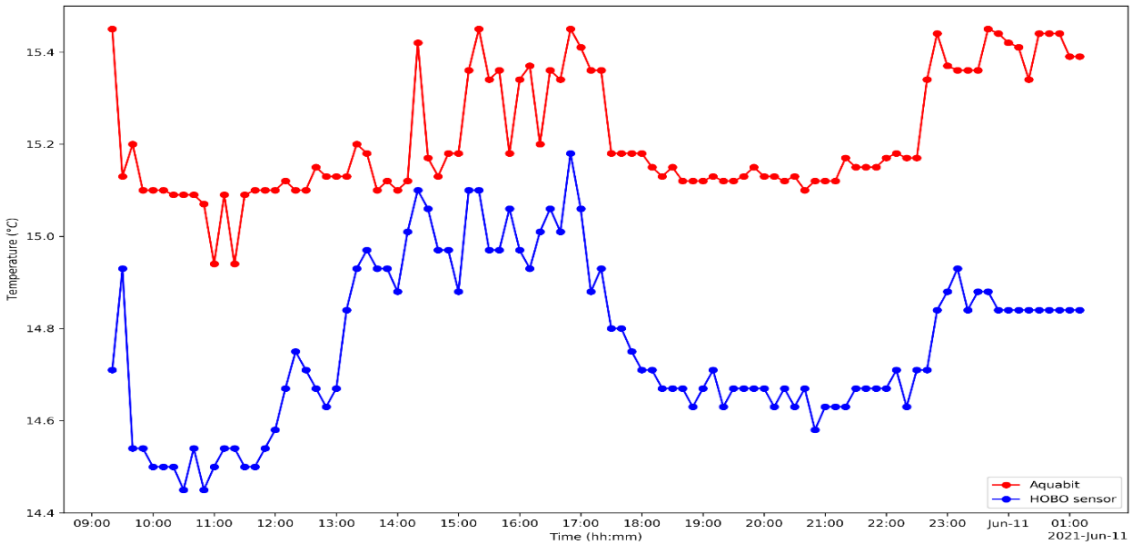

Figure 48 - Temperature data collected by the HOBO sensor (each 10 min) and the Aquabit device (mean values for each 10 min).

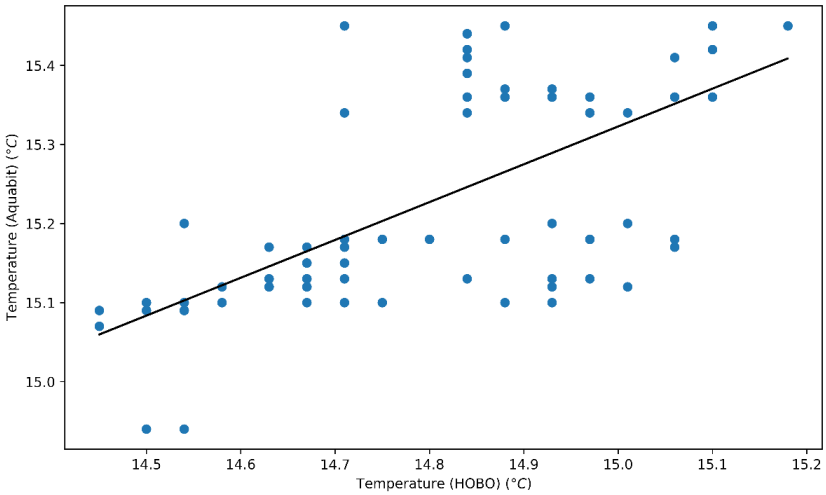

Figure 49 - Scatter plot of the logged temperatures for each 10 min by the HOBO sensor and the Aquabit device.

The Figure 50 shows the hourly average of the temperature for the two sensors. Here we can see more clearly that the two sensors follow the same trend, with a small bias. According to the Aquabit internal temperature sensor datasheet [133], the typical maximum error is approximately 0.6 °C, which is validated by our findings. The correlation for the two hourly averages is 0.699 with $p < 0.01$.

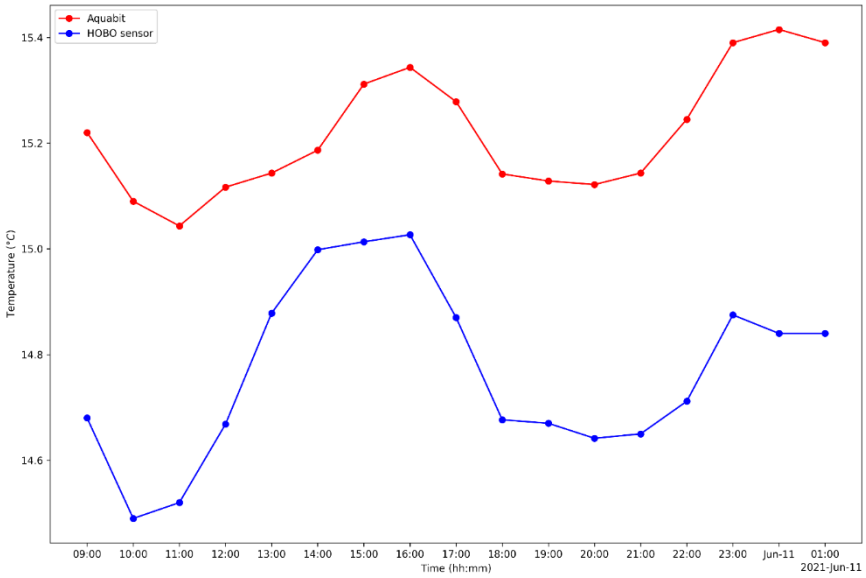

Figure 50 - Hourly average of the temperature logged by the HOBO sensor and the Aquabit device.

The same analysis was done for the light sensor, comparing the HOBO data logged and the Aquabit data from the clear channel of the sensor. The mean value read by the HOBO light sensor was 6242.6 lux, with standard deviation of 7937.6; while the Aquabit sensor had a mean value of 3581.9 lux, with standard deviation of 6856.0. The two measurement series are correlated with $R = 0.613$ and $p < 0.001$. The Figure 51 shows the two measurement series.

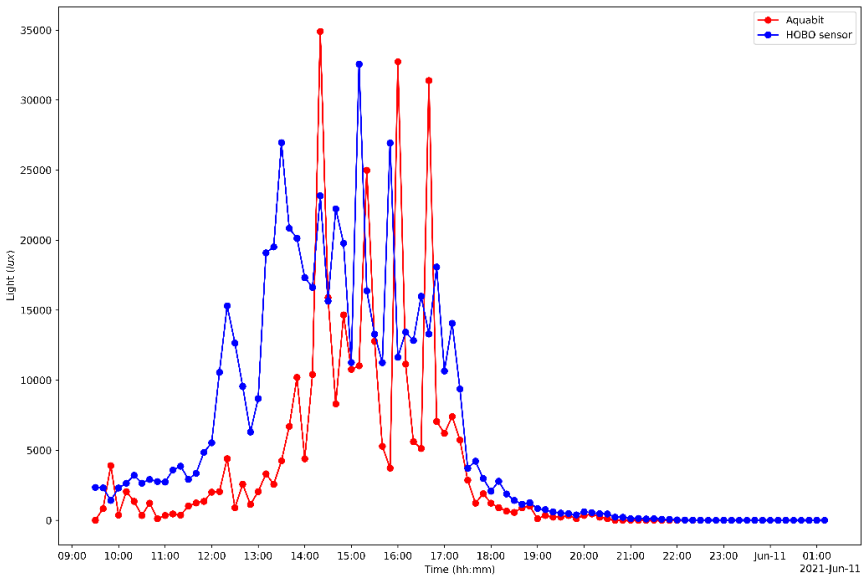

Figure 51 - Light intensity measured by the Aquabit (in red) and the HOBO sensors for the deployment date of 10/Jun/2021.

The Figure 52 shows the hourly average of the two light intensity measurements (by the Aquabit in red, and the HOBO sensor in blue). The hourly average of the two sensors is strongly-correlated with $R = 0.853$ ($p < 0.001$). There is a 'apparent lag' of 1 hour between the HOBO sensor and the Aquabit, but since the Aquabit was deployed with the light sensor opening sideways (as opposed to the HOBO sensor that was deployed with the light opening vertically), this lag on the hourly average is most likely due to the Sun's position changes during the day and the resulting reflected light arriving into both sensors.

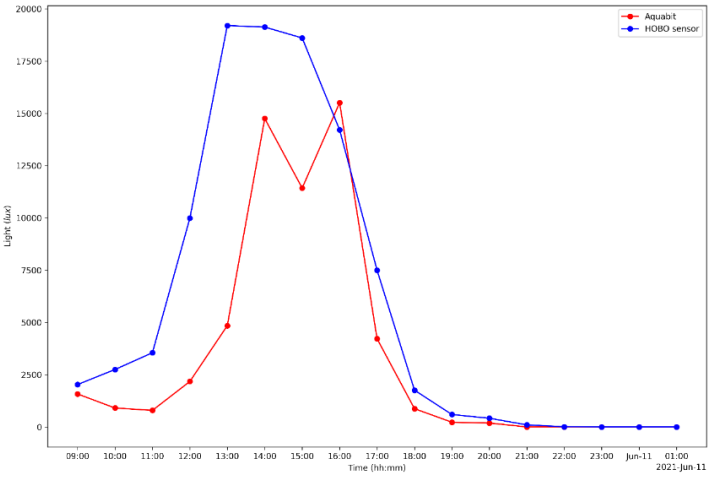

Figure 52 - Hourly average of the light intensity logged by the HOBO sensor and the Aquabit device.

5.3.2 Wave Movement Data Analysis

The IMU data collected consists of three values for each measurement, representing the magnitude of the acceleration value for each axis in the 3D coordinate system shown in Figure 34, plus a timestamp from the internal IMU clock. The actual sampling frequency achieved by the device was 13.02 Hz. A total of 680108 datapoints were collected – representing around 14.5 hours of data.

A median filter was applied to the data with window time of 1s. This acts as a low-pass filter to remove high-frequency noise. The data from 09:00 to 10:00 was removed from the analysis for the same reason of the previous data analysis – the device was being manipulated and undergoing deployment.

The total magnitude of the acceleration of the device in a given time *t* is shown in Equation 63.

$$|a| = \sqrt{a_x^2 + a_y^2 + a_z^2} \qquad 63$$

Where a is the acceleration vector, a_x is the magnitude of the acceleration in the x axis, a_y is the magnitude of the acceleration in the y axis, and a_z is the magnitude of the acceleration in the z axis.

One would expect that the mean value of the acceleration magnitude for the whole time period would be *1g* (the value of the gravity). Indeed, applying the Equation 63 for each datapoint, we get a time-series $|\boldsymbol{a}|$ with mean value 1000.52 *mg* and standard deviation 3.12. This *1g* value represents the static acceleration that is caused by the gravitation field of the Earth.

We are interested in the dynamic acceleration: the acceleration caused by movement of the device. After applying the median filter, the static acceleration was removed by subtracting the mode for each axis, as described by the Equation 64 – where *i* represents each axis (x, y, z) of the accelerometer. The mode of the output of each axis is assumed to represent the static acceleration measured by the accelerometer that is due to the gravity [7].

$$a_i^{dyn}(t) = a_i(t) - mode\big(a_i(t)\big) \qquad 64$$

The magnitude of the total dynamic acceleration in a time *t* is then:

$$|\boldsymbol{a}^{\boldsymbol{dyn}}|(t) = \sqrt{\left(a_x^{dyn}(t)\right)^2 + \left(a_y^{dyn}(t)\right)^2 + \left(a_z^{dyn}(t)\right)^2} \qquad 65$$

The Figure 53 shows a slice of the dataset, with datapoints collected between 2021-06-10 14:30 and 2021-06-10 15:30. The dynamic acceleration is also shown in magenta. Negative values for a_x , a_y , and a_z represent accelerations in the opposite direction than the reference axis. This data has a very fine-scale resolution, and can be used to determine wave dynamics [7], [13], [16], [161].

After filtering and calculating the dynamic acceleration, we resample the data with period of *60s*, taking the mean value for each period and the standard deviation. According to Focht and Shima [13], the standard deviation of the dynamic acceleration over a time period is a good proxy for wave movement.

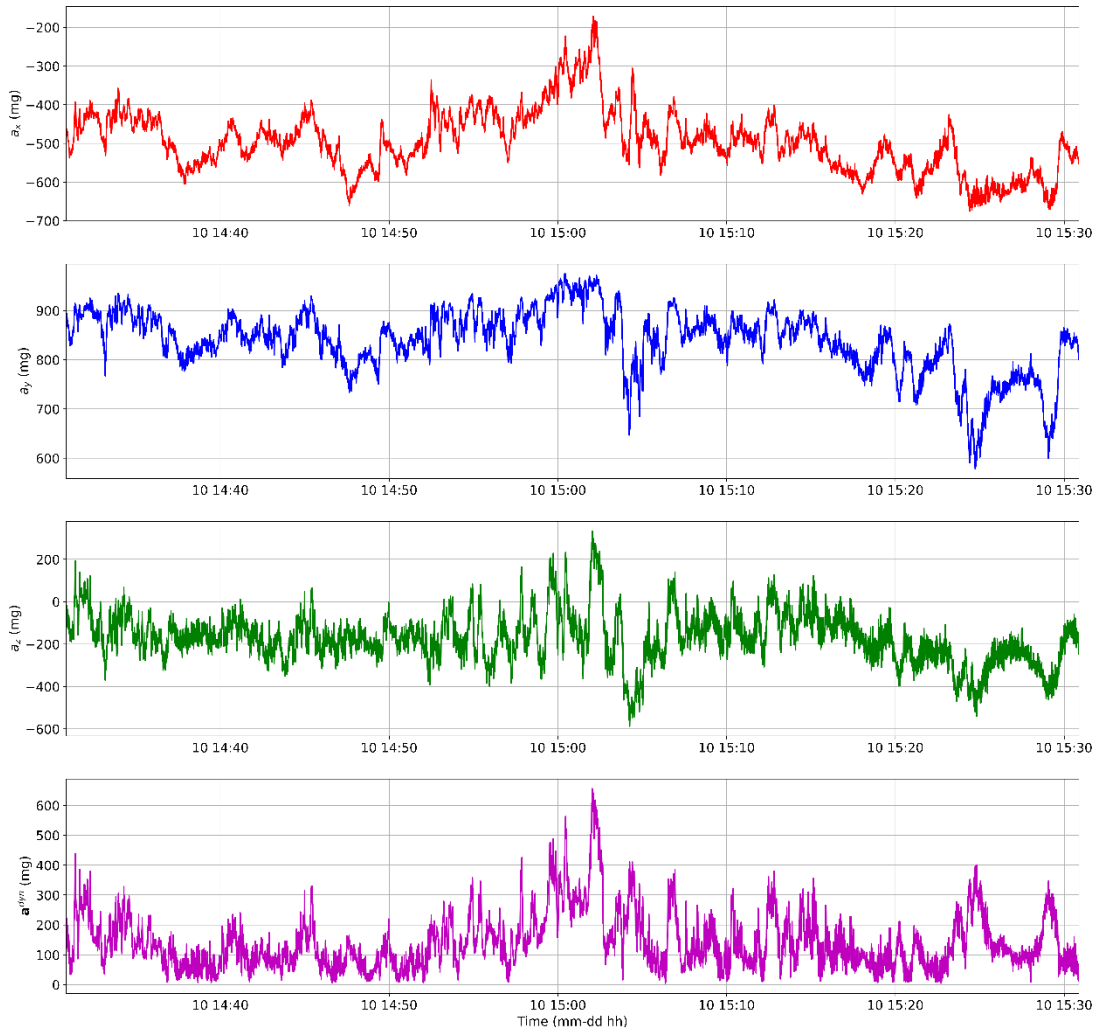

Figure 53 - Movement data collected by the Aquabit between 14:30 and 15:30. From top to bottom: acceleration in the x axis, acceleration in the y axis, acceleration in the z axis, and dynamic acceleration calculated.

The resulting data is shown in Figure 54. In order, the time-series shown are (all sampled over periods of 60s): mean dynamic acceleration for the x axis, mean dynamic acceleration for the y axis, mean dynamic acceleration for the z axis, mean dynamic acceleration magnitude, and standard deviation of the acceleration magnitude.

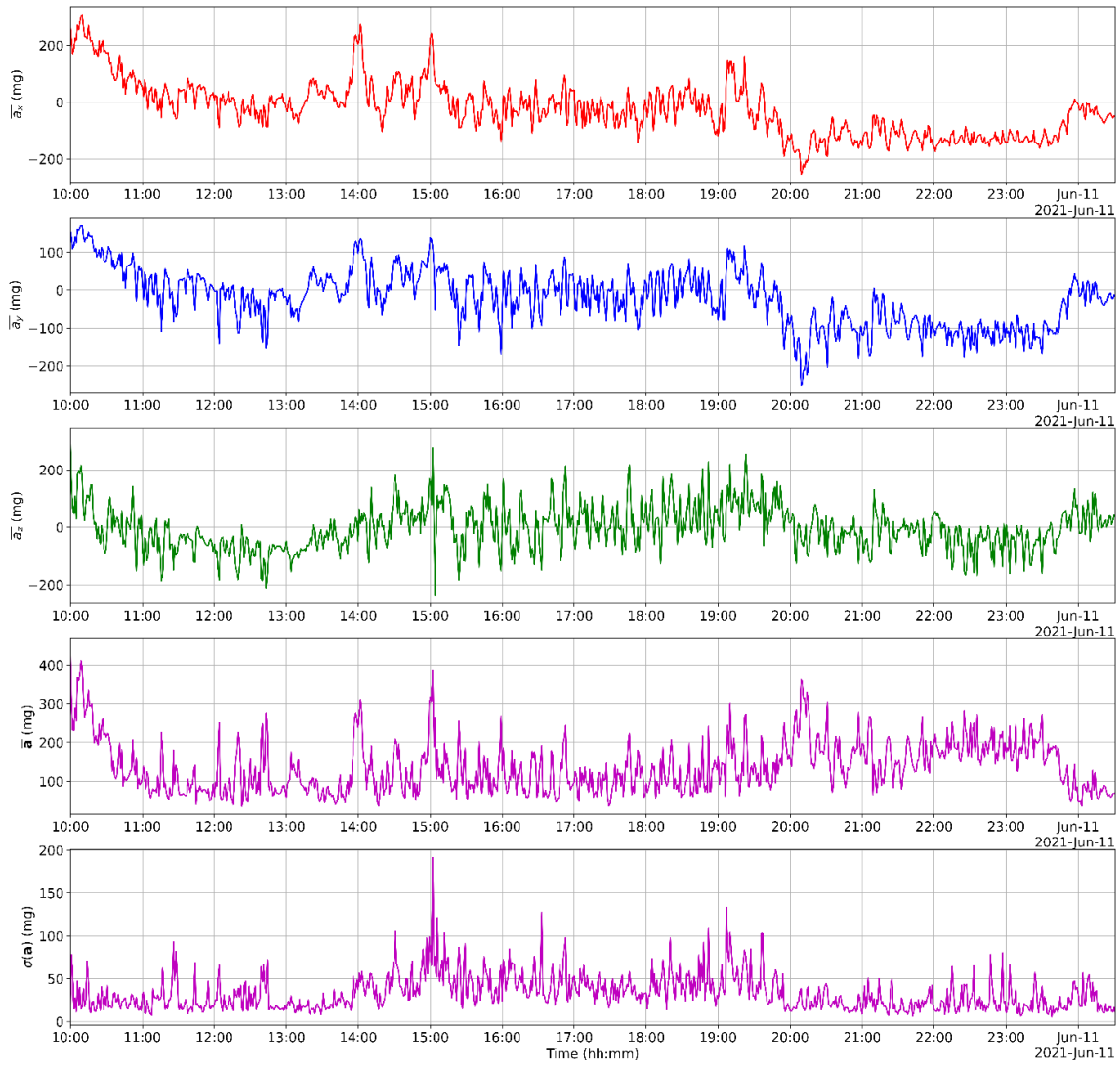

Figure 54 - Motion data collected by the Aquabit in the deployment day of 10/Jun/2021. The values shown are: (a) mean dynamic acceleration in the x-axis; (b) mean dynamic acceleration in the y-axis; (c) mean dynamic acceleration in the z-axis; (d) mean dynamic acceleration; and (e) standard deviation of the dynamic acceleration.

Since no other data for the wave movement is available for the date of the trial, the acceleration data was compared to wind data. Various studies have used wind as a proxy for water movement and wave incidence [9], [12], [13], [162]. The wind data used in this analysis was collected by the Irish Meteorological Service Met Éireann at the Mace Head weather station, at approximately 10 km of distance from the trial site (Lehanagh Pool). The location of the weather station and the trial site are shown in Figure 55.

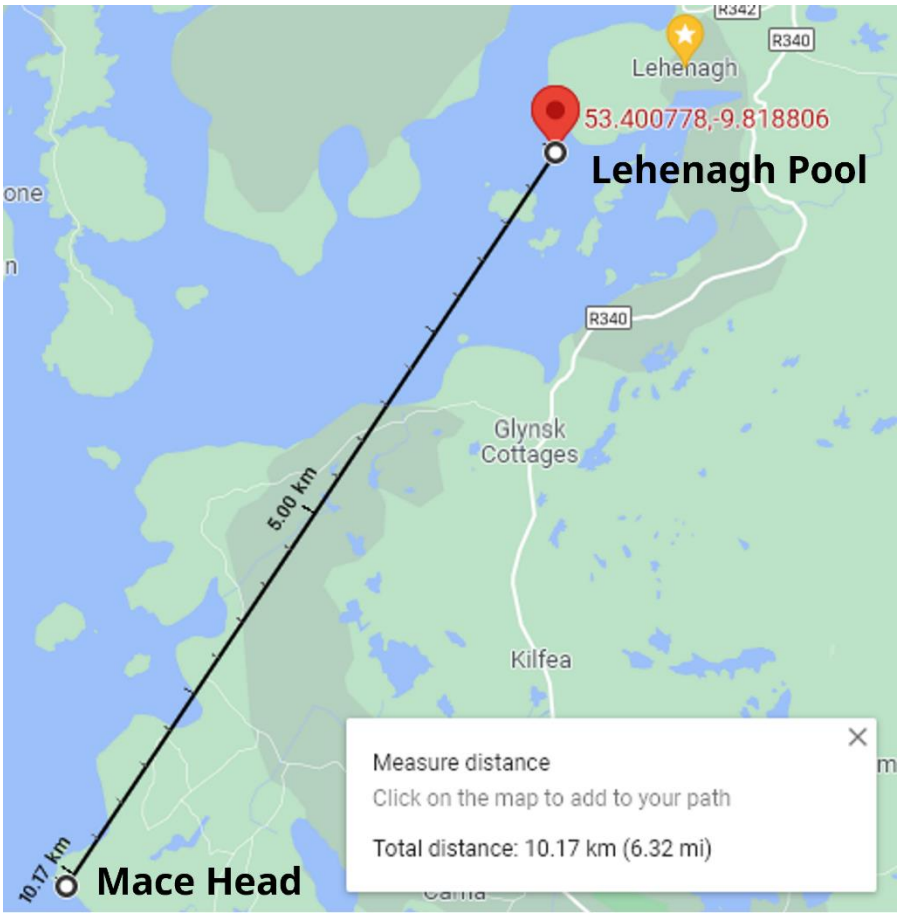

Figure 55 - Location of weather station in relation to the trial site (Lehanagh Pool).

The data collected by the Met Éireann for the day of the trial is shown in Figure 56. It is available to download at https://www.met.ie/climate/available-data/historical-data [163].

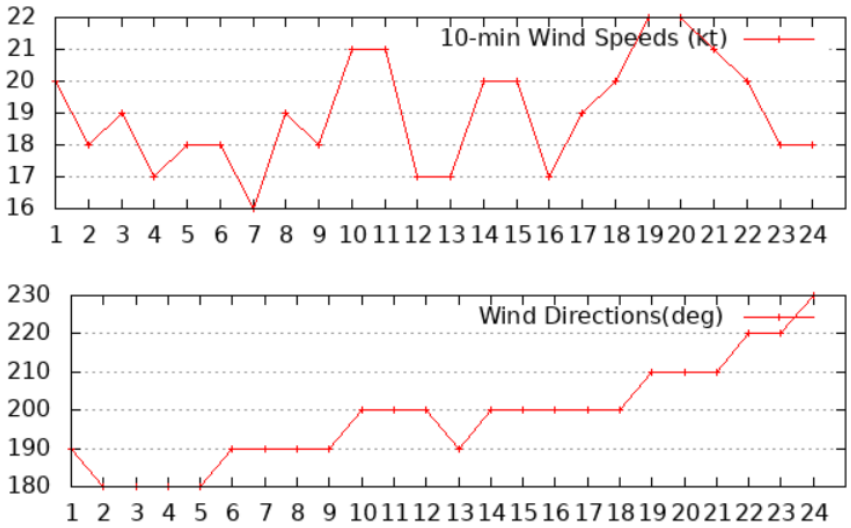

Figure 56 - Wind speed and direction measured at the weather station in Mace Head for the day of 10/Jun/2021.

To compare wind speed with acceleration of the device, the wind speed was derived over its' period (hourly data). The derived wind speed and the mean dynamic acceleration for each axis are plotted together in Figure 57.

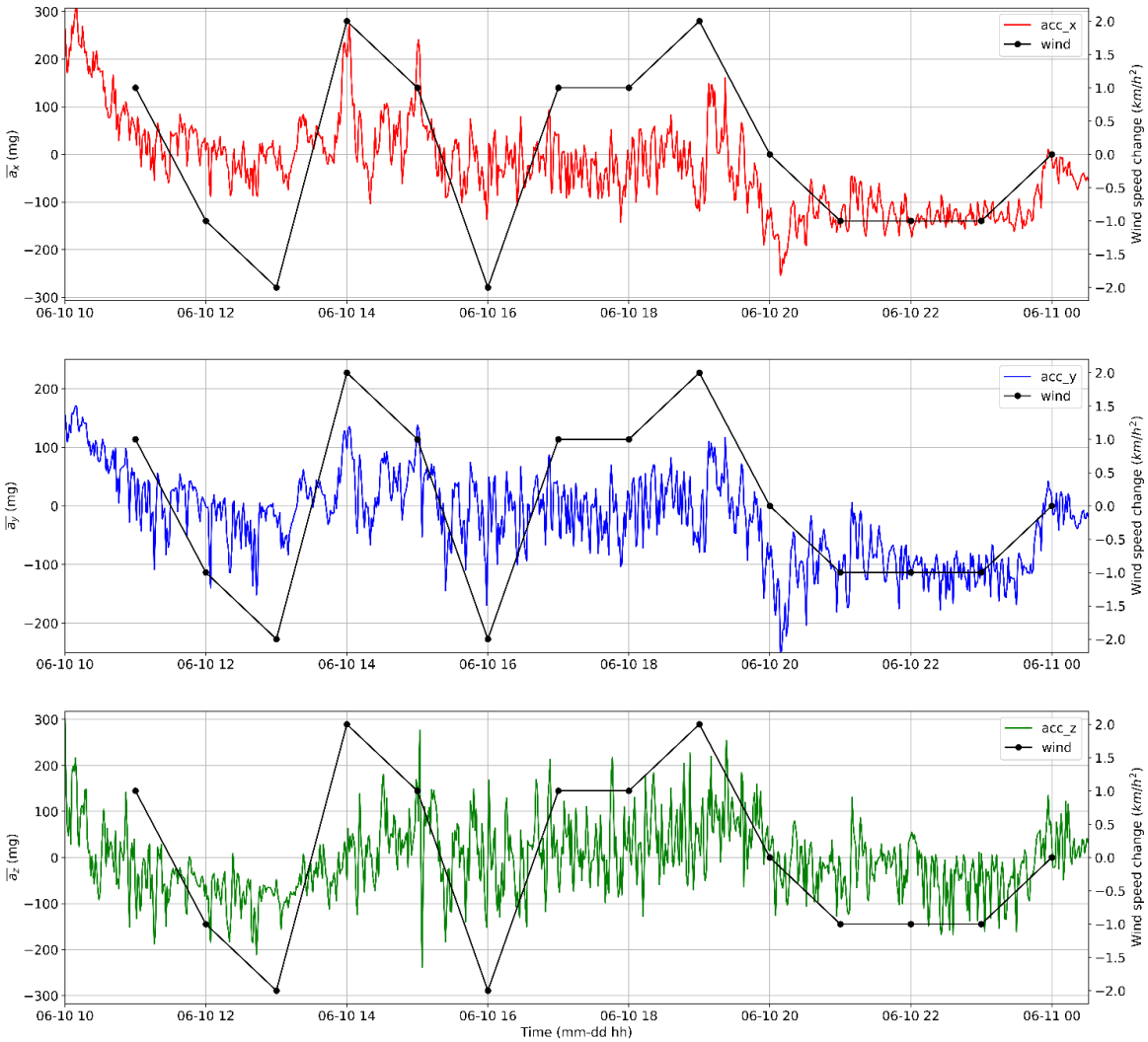

Figure 57 - Comparison between derived wind speed (wind speed change) and mean dynamic acceleration for each axis (x axis in red, y axis in blue, and z axis in green).

In Figure 57, the black line is the derived wind speed – i.e. the difference from the previous hourly value. A positive value of derived wind speed means the wind is stronger, and a negative value means the wind got weaker (lower speed). Although the black line closely follows the mean dynamic acceleration

in the y axis, we have to be careful because the y axis at 22:00, for example, has a non-zero average value, while the wind speed is decreasing. So a correlation there is not significant. We can see that a big positive increase in the x axis at 14:00 follows the positive wind speed change. The big decrease in wind speed starting at 19:00 is also correlated with big average dynamic acceleration increase on the opposite direction in the x and y axis.

However, these values are not correlated statistically ($p > 0.1$). This follows the results from Lindegarth and Gamfeldt [17] and Focht and Shima [13] – although wind data is usually used as a proxy to derive wave exposure index, the fine-scale water movement and wave exposure are not necessarily correlated with the wind.

5.4 SECOND DEVICE DEPLOYMENT

Three Aquabit devices were deployed again at Lehanagh Pool from 17/07/2021 to 21/07/2021. Two of the devices collected data for approximately 3 days before running out of battery, while the other one collected only 14h of data. The difference in lifetime for the last device could be due to battery differences or a problem in the PCB which has not been identified. We are currently investigating the reason. Simultaneously, 200m away from the deployment site, a data buoy (MaxiMet GMX600, Gill Instruments Limited, UK) was located, measuring wind speed, wind direction and buoy tilt at 10 min intervals. The location of the device deployment and the data buoy are shown in Figure 58.

Figure 58 - Satellite image of location of data buoy (53.401170N, -9.818715W) and device deployed (53.399801N, -9.820877W).

The data from the buoy was compared to the accelerometer data from the attached sensor device. As mentioned in the previous section, Focht and Shima [13] consider the variation of dynamic acceleration to be a proxy of wave energy. However, no meaningful correlation between buoy data and device data was found (Pearson's $R < 0.5$ and $p > 0.1$). Even with a time delay of 10, 20 or 30 minutes, no correlation was found. This, again, implies that only wind speed is not a good proxy for wave movement. *Figure 59* and *Figure 60* show the comparison of the data collected by the data buoy (Wind Speed and Buoy Tilt on X and Y axes) with the dynamic acceleration data collected by the attached sensor device.

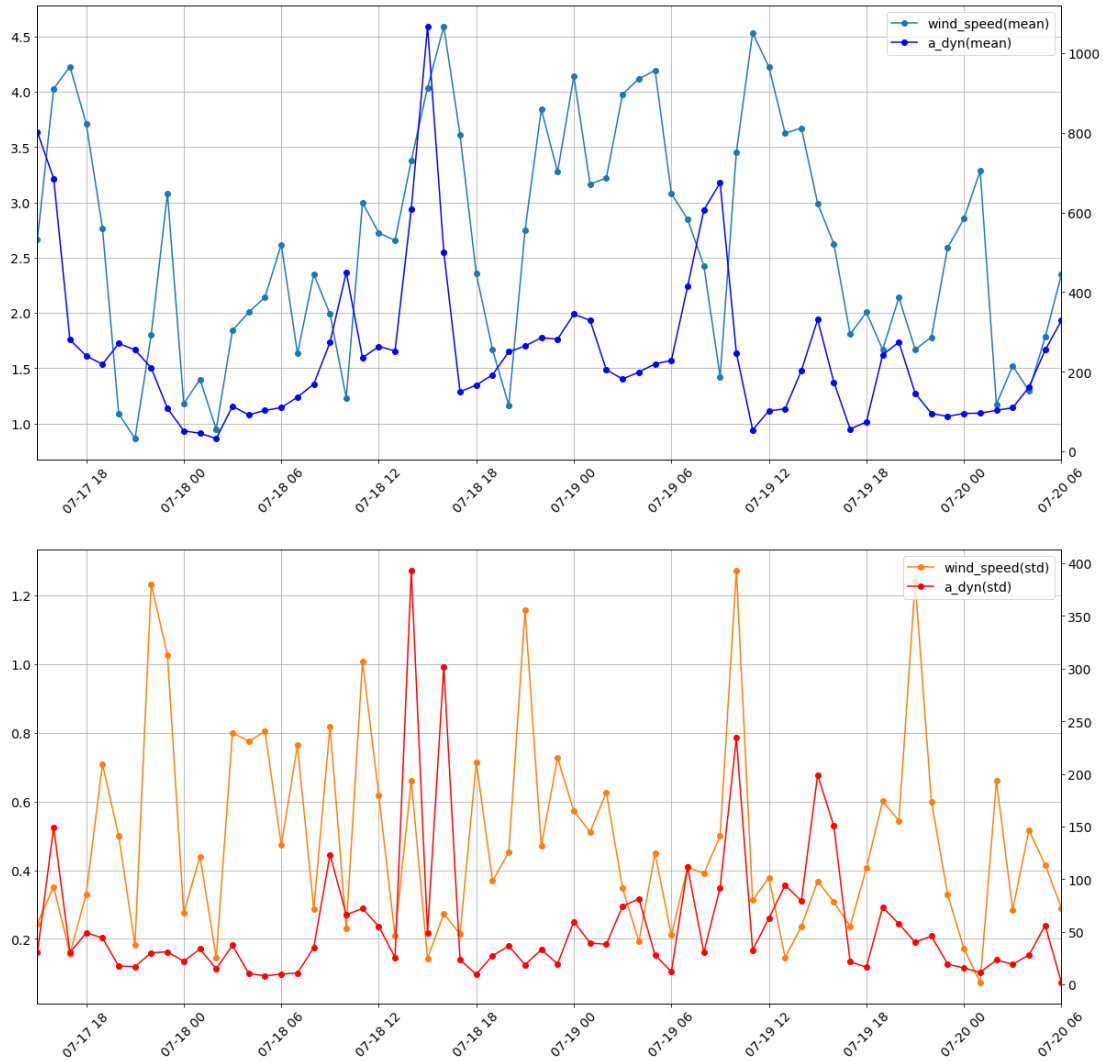

Figure 59 - Comparison of wind speed (from data buoy) and dynamic acceleration from the attached device.

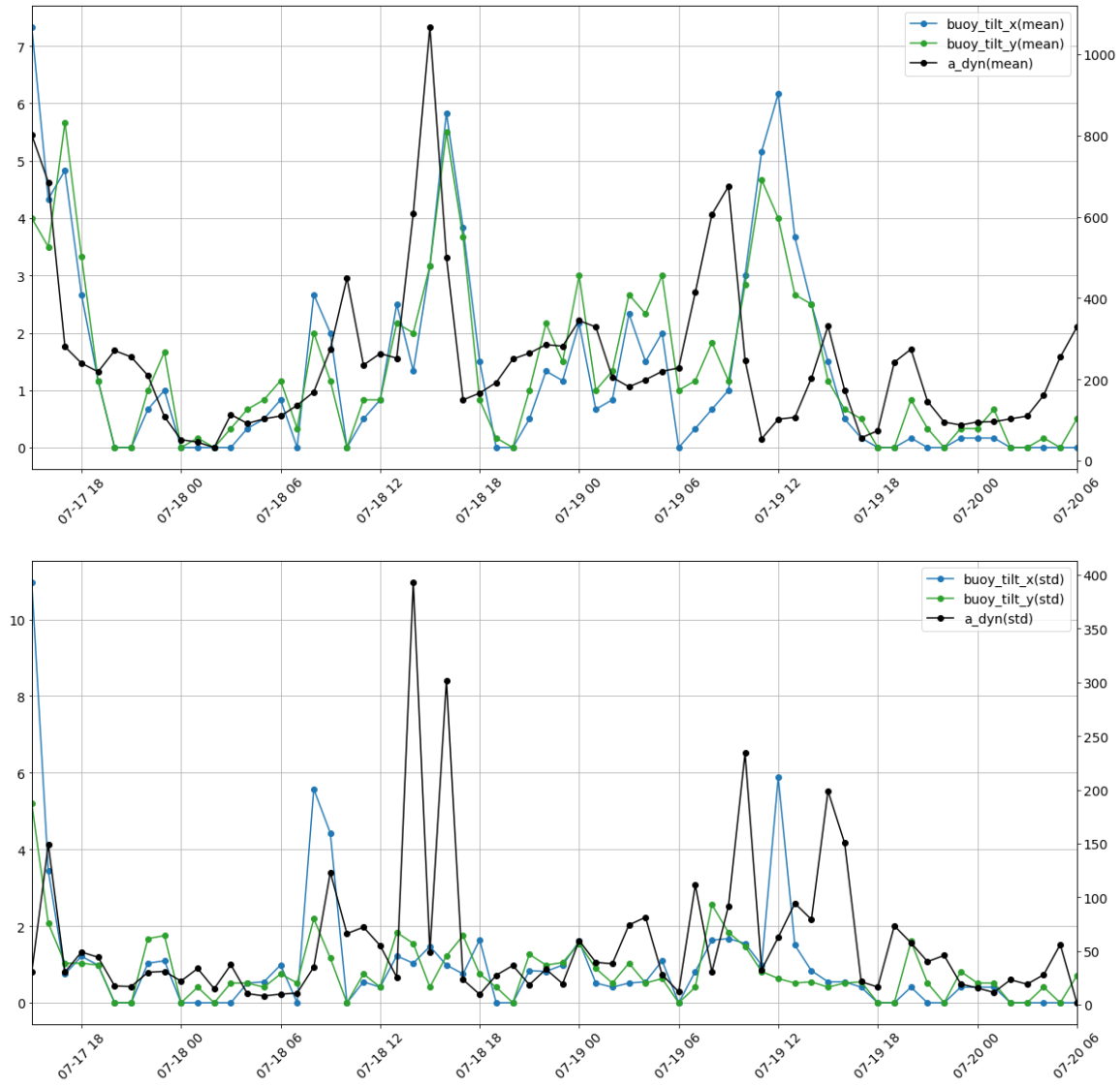

Figure 60 - Comparison of buoy tilt (X and Y axis of data buoy) with the dynamic acceleration measured by the attached sensor device.

The pressure sensor in the attached sensor device can be used to calculate the depth of the device, which is a proxy for wave height. The method used to convert the raw pressure reading from the sensor into the depth value considers the following Equation 66 [164], [165] :

$$P = P_{atm} + \rho g d + \rho g x(t) \qquad 66$$

where ρ is the density of the seawater, g is the gravitational acceleration, d is the deployment depth and $x(t)$ is the sea surface displacement in a specific time t.

The deployment depth of the device was of approximately 2.5 m. To more accurately determine this depth, the value of the atmospheric pressure P_{atm} was removed from the pressure data, and the mean value of the resulting timeseries was considered to be equal to the hydrostatic pressure $P_{st} = \rho g d$. This assumes that $\overline{x(t)}$ (the mean value of the surface displacement timeseries $x(t)$) is 0.

This mean value was then removed from the pressure time series, and then the resulting values were divided by the density of seawater and the gravity to obtain the approximate wave height (sea surface displacement) over time, shown in *Figure 61*.

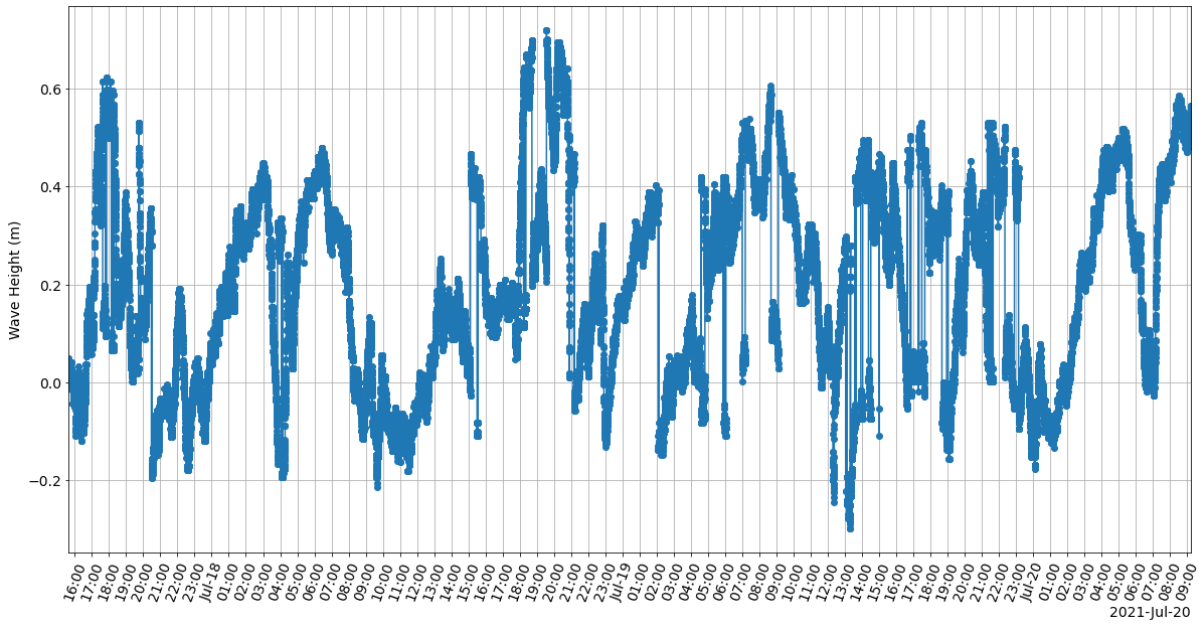

Figure 61 - Sea surface displacement measured by the pressure sensor of the attached sensor device.

This result, however, is only approximate, since some assumptions have been made in the process of calculating the surface displacement from the pressure data. These assumptions are:

- The calculated mean value of the pressure time-series is $\overline{P(t)} = P_{atm} + \rho g d$. Since the actual accurate depth value is not known due to deployment variability, it was calculated from the data collected and was found to be 2.6 m. Since the reported deployment depth was 2.5 m, a possible 0.1 m of error in this calculation exists.
- We considered the seawater density to be $\rho = 1025 kg/m^3$. This is not the real value, which depends on the water salinity and temperature. Since the water salinity is not known, the actual density of the sea water is also unknown. Therefore, the calculation done for the surface displacement timeseries results in only an approximation of the actual value.

To overcome these limitations, one could use the accelerometer and gyroscope data collected by the IMU to calculate the vertical displacement of the device. There are some solutions that use accelerometer data in a wave-rider buoy to calculate wave height, such as the work done by Bender et al. [166] and Kennedy et al. [15]. These solutions, in general, assume that the vertical tilt of the device is small, so some simplification is done in the calculations. For our work, the device is attached to the seaweed which freely moves with the water, so this assumption may not hold.

However, by combining the data from accelerometer and gyroscope, a more accurate vertical displacement could be calculated (i.e. by using inertial navigation equations such as described in [167]). This value combined with the calculated displacement from the pressure data could yield a better estimate of wave height. Future work in this area includes deploying the

device in known wave conditions, finding an appropriate sensor fusion for this instance, and analysing the results.

5.5 RESULTS DISCUSSION AND CONCLUSIONS

The objective of this work was to verify if an integrated solution that combines multiple sensor modalities into a miniaturised package is feasible. We verified that the data collected by the internal sensors is comparable to current commercial sensors. This integrated solution is novel – as far as we know there is no commercial solution that integrates motion, temperature, depth, and light sensing for seaweed monitoring.

The next objective was to deploy it in multiple points of a seaweed/IMTA farm so that fine-scale data about the environment (such as water movement, water temperature, pressure, and light intensity reaching the seaweed) can be collected, analysed, and compared with other environmental sensors on the site.

The device developed embeds a pressure sensor that can measure depth and temperature, a light sensor that measures incident radiation, and an IMU to track seaweed motion parameters with the potential to map this motion to water movement and wave exposure experienced by the seaweed crop. The data measured by these sensors is then logged internally in its memory; and can be transmitted wirelessly via its NFC communication interface in the field to the users' smartphone using the developed application or a wired USB connection. The device is rechargeable, reusable and can be customised with different sampling frequencies to adapt to different needs (for example, a farm operator could need only hourly data, while a researcher interested in fine-scale data could configure the device to sample every second).

All the sensors were characterised and calibrated in lab experiments to verify their accuracy. The results show that the sensors chosen were capable of

measuring data according to the requirements established by end users and literature. Therefore, the device can be used to monitor environmental factors in a specific place in an aquaculture site and the user can be sure that the data for each parameter is co-located and correlated with each other enabling seaweed farmers to make close to real time decisions as to their crop management practice.

Since the device has an internal time keeping feature, the data collected is also dated to the second, which enables the user to plot the data in a time series and analyse it for trends and diurnal patterns and map it to other sensed data available from their deployment if such are available.

The device was waterproofed with the specifically designed enclosure and filled with a polyurethane resin (PUR) rated for marine use. This means that the device can be deployed in either seawater or freshwater aquaculture farms.

The mechanical enclosure was designed to be flexible as to the requirements of the particular type of deployment, so that the user can choose how to best deploy the device for their needs. Small eye-holes on the sides of the enclosure allow for threading of lines to secure the device to mooring lines or to the seaweed itself. The backside has a pattern to provide a better surface area in case the user wants to glue the device to the seaweed/kelp blades. This type of attachment would enable the collection of data specifically about the wave and water motion effects on the seaweed. Since the device is very small, it does not add significantly to the drag or additional stress to the seaweed.

Communication is enabled by the USB interface which was shown to be fully operational for high-speed transmission of data in “out of field” conditions. It can be used to communicate with the device, download data, power, and reprogram the device.

For the NFC communication mechanism designed to be used when "in the field" to configure the device and download smaller amounts of data to the users' phone, an Android app was developed to communicate with the device. It can send commands (such as wake-up, shutdown, start data collection, etc.), change the sensors configuration and sampling frequency, and download data. Due to the miniaturised form factor for the antenna and reduced opportunity for significant power transfer, the read range for the NFC communications is small and the user needs to place their phone against the outer enclosure for the device. This could be due to: the very small size of the antenna used in the device, which greatly reduces the captured magnetic field by the antenna, reducing the induced voltage on the ST25DV; the presence of metal (circuit and battery) next to the antenna, which generates more losses and absorptions; and the potentially unoptimized NFC reader antenna (smartphone) for this specific application (reading a smaller antenna than the standard NFC). However, the system read range was sufficient to enable data download using a standard smartphone with the required capability.

An important feature of the device that we made sure was present is the customisability of the sensors sampling frequency. Especially in the case of the IMU, the sampling frequency greatly affects the type of data that can be extracted using data analysis methods and this is a research topic for future work. A high sampling frequency allows the user to detect very fast movements that would otherwise be missed. However, this needs to be balanced against power consumption – as the higher the sampling frequency, the higher the power consumption is and the less time the device can be deployed due to the battery lifetime.

The device was optimised for low-power consumption, from the hardware design to the firmware development, making sure multiple power options are available. To preserve battery while not deployed, the device has a hardware

on/off controller that can put the system in shutdown mode or wake it up via the USB or the NFC interfaces.

As the power test shows, the device's battery can last for a week if the sampling frequency is set to 0.2 Hz. A longer period between samples would increase the time the device can be deployed, and this can be customised by the user.

The pilot trial deployment in the Lehanagh Poll IMTA site had the objectives of verifying if the enclosure could withstand the seawater environment and if the attachment method was secure enough to prevent the device from dislodging from the seaweed. We concluded the test successfully, as all the three devices deployed were recovered with no damages.

Although the device was deployed on an 'artificial seaweed', it could correctly measure the environmental parameters at the deployment point, and also monitor the water movement. The output of the temperature and the light intensity sensors were correlated with the output from another commercial sensor deployed in the same site.

The movement data collected by the IMU for the deployment was also analysed. As we can see in Figure 53, the acceleration data collected has a very fine-scale resolution, and the wave dynamics can be described in detail by the acceleration data [13], [16], [161].

6 CONCLUSIONS AND FUTURE WORK

Conclusions

Some of the most important parameters that influence seaweed growth are water quality, temperature, light radiation, water pH, nutrient availability, and wave incidence. For an IMTA site, it is necessary to monitor these parameters with the best resolution possible so as to maximise crop yield and minimise environmental impact. Current commercial and research seaweed monitoring technology can cover large areas at low resolution, but for small scale, fine resolution, in-situ monitoring, commercial solutions are available for single sensor modality only. No integrated solution is currently available in a miniaturised form factor which can be directly attached to seaweed or other IMTA species.

In this work, was presented the development of a novel miniature low-power NFC-enabled multi sensor system that fills the gap identified as regards commercially available multi modal miniaturised aquaculture sensors. More specifically, current methods for direct monitoring of aquaculture sites rely on the deployment of multiple separate sensors, which increase the costs and energy requirements. In particular, current methods of wave monitoring are expensive and, therefore, not accessible to many small IMTA farmers. In addition, accelerometer tags commercially available for aquaculture purposes do not provide raw data at a high-enough sampling rate for detecting fast events or for using in machine learning applications.

The "Aquabit" system described in this thesis was developed with the objective of monitoring any type of aquaculture site, in particular IMTA sites, where multiple species are cultivated. The requirements defined in conjunction with end IMTA users were: for the device to be as small as possible; to withstand the harsh conditions of marine water; to be low-power

(long deployment cycles) to be capable of monitoring many aquaculture species (in specific seaweed); to be able to communicate wirelessly; and to be flexible and adaptable to any deployment (with user configured sampling rates).

To remotely monitor some IMTA aquaculture species, the system needs to wirelessly transmit data in real time to the farm operator. To establish the feasibility of underwater wireless communications, the effect of the salinity of seawater on RF transmissions, both on the near and the far-field was modelled and characterised. As already predicted by theory, both are negatively affected by the presence of dissolved ions in the water. The Path Loss for RF transmissions both in the near-field and the far-field relating to the salinity of the water medium was modelled. The Path Loss can then be used to calculate the link budget and estimate the energy needed for transmission in marine water. It was established that near-field RF links perform better than far-field due to the smaller operation frequency. However, the range is very limited as predicted by theory and the research literature in this space.

With that knowledge, we developed a first prototype of the seaweed sensor system using a COTS LF RFID IC – the TMS37157 134.2kHz RFID front-end from Texas Instruments, with the objective of testing its transmission rate, range, and compatibility with existing PIT tag systems already in use in aquaculture. In line with the models, we found that this system had a very limited data rate. We also found that the TMS37157 was not compatible with the existing PIT tag systems.

The second-generation version of the prototype sensing system then was developed with a HF RFID front-end that is compatible with NFC. This allows the system to be read by smartphones and have a higher data rate, although the range is still limited. This facilitates the use of the Aquabit device in

multiple application scenarios allowing the configuration of its capabilities in the field and allows limited (slow) data download.

The system combines multiple physical sensors and an internal real-time clock to provide a detailed characterisation of the point in the farm site being monitored. The sensors integrated were: movement via an IMU with 6 degrees of freedom; temperature and depth via a pressure sensor with direct interface with the water; and light using a RGB clear colour sensor with an IR filter to monitor the light wavelengths of interest as defined by the seaweed farmers.

All the sensors were characterised and calibrated in lab experiments. The results show that the sensors chosen were capable of accurately measuring data according to the requirements established. Therefore, the device can be used to monitor environmental factors in a specific place in an aquaculture site and the user can be sure that the data for each parameter is co-located and correlated with each other.

The enclosure developed was 3D printed due to the cheaper cost of development and production than other prototype development methods. The 3D printing process, however, does not necessarily make the plastic enclosure waterproof. To ensure the enclosure could withstand the harsh marine environment, the interior of the enclosure was filled with a waterproof polyurethane resin. The mechanical enclosure was designed to be flexible in the type of deployment. The environmental tests performed on the device showed that the enclosure was waterproof and able to sense pressure and light through the enclosure. The deployments in the marine environment also showed that the enclosure can withstand the harsh environment for days with no functional degradation.

The firmware was developed to optimise the data capture and allow for customisation of the sensors' operational parameters, such as sampling

frequency, so that the user can adapt the device for their specific monitoring application. For ease of use, a smartphone application for Android to communicate with the device via NFC to configure the device's parameters was developed.

The system was deployed in Lehanagh Pool (Bertraghboy Bay, Connemara, Ireland) with the help of the Marine Institute for a week, collecting data on water temperature, depth, light, and movement. The data collected was compared with the outputs from other sensors deployed on the farm, and the measurements are correlated.

We conclude that this newly developed system is a significant improvement over existing aquaculture commercial sensors due to its small size, flexibility, low power consumption and ease-of-use.

Future Work

Although the results shown are promising, the device has only been deployed monitoring the farm conditions while attached to artificial seaweed. Further investigation in different deployments will focus on attaching the device to real seaweed to test the adhesion to the blades and the resistance of the seaweed to any breakage caused by the device. Added to that, the impact of the device on the seaweed motion dynamics would also be worthy of further investigation but is outside of the scope for the body of this work.

Currently the system logs the sensor data to be downloaded and post-processed. A future firmware iteration for the device should incorporate embedded analytics in its microcontroller so that some preliminary data and status can be transmitted wirelessly in real-time to a receiver in the farm. This would enable the device to monitor farm conditions in real-time and empower the farm operator to make quicker decisions about the farm. The raw data

collected can be still stored in the internal memory of the system so that more computational heavy analytics can be performed at a later date.

The device, at the present moment, is recharged via the USB connector. For ease of use by the farm operators, a future improvement would be adding wireless charging capabilities so that the device could be charged without opening it up and to minimise any requirement for cable handling.

Other further improvements to the device include extending the underwater communication range and data rate by possibly adopting another technology – such as Bluetooth or acoustic communication. Although in theory low-frequency magnetic induction is the best method suited for the coastal saline environment of IMTA farms, the practical range of communication is too short. Therefore, a solution that could provide more range is using an acoustic communication system. That solution, however, would require more power and computational resources to account for the multipath and other channel problems that are present in the environment.

As for data analysis, there are current methods and experiments that use either IMU data (accelerometer and gyroscope) or pressure data to estimate the wave height and energy, but no solution which combines both for a better estimate. Future work would involve building a sensor fusion algorithm to combine both sensors into a wave height measurement.

REFERENCES

[1] N. Ridler *et al.*, 'Integrated Multi − Trophic Aquaculture (imta): A Potential Strategic Choice for Farmers', *Aquac. Econ. Manag.*, vol. 11, no. 1, pp. 99–110, Mar. 2007, doi: 10.1080/13657300701202767.

[2] T. Chopin *et al.*, 'Integrating Seaweeds into Marine Aquaculture Systems: A Key Toward Sustainability', *J. Phycol.*, vol. 37, no. 6, pp. 975–986, 2001, doi: https://doi.org/10.1046/j.1529-8817.2001.01137.x.

[3] S. B. Schroeder, C. Dupont, L. Boyer, F. Juanes, and M. Costa, 'Passive remote sensing technology for mapping bull kelp (Nereocystis luetkeana): A review of techniques and regional case study', *Glob. Ecol. Conserv.*, vol. 19, p. e00683, Jul. 2019, doi: 10.1016/j.gecco.2019.e00683.

[4] M. Bennion, J. Fisher, C. Yesson, and J. Brodie, 'Remote Sensing of Kelp (Laminariales, Ochrophyta): Monitoring Tools and Implications for Wild Harvesting', *Rev. Fish. Sci. Aquac.*, vol. 27, no. 2, pp. 127–141, Apr. 2019, doi: 10.1080/23308249.2018.1509056.

[5] L. I. N. Fan, D. U. Meirong, L. I. U. Hui, F. A. N. G. Jianguang, A. Lars, and J. I. A. N. G. Zengjie, 'A physical-biological coupled ecosystem model for integrated aquaculture of bivalve and seaweed in sanggou bay', *Ecol. Model.*, vol. 431, p. 109181, Sep. 2020, doi: 10.1016/j.ecolmodel.2020.109181.

[6] S. García-Poza *et al.*, 'The Evolution Road of Seaweed Aquaculture: Cultivation Technologies and the Industry 4.0', *Int. J. Environ. Res. Public. Health*, vol. 17, no. 18, Art. no. 18, Jan. 2020, doi: 10.3390/ijerph17186528.

[7] S. N. Evans and D. A. Abdo, 'A cost-effective technique for measuring relative water movement for studies of benthic organisms', *Mar. Freshw. Res.*, vol. 61, no. 11, pp. 1327–1335, Dec. 2010, doi: 10.1071/MF10007.

[8] C. L. Hurd, 'Water Motion, Marine Macroalgal Physiology, and Production', *J. Phycol.*, vol. 36, no. 3, pp. 453–472, 2000, doi: https://doi.org/10.1046/j.1529-8817.2000.99139.x.

[9] W. Visch, G. M. Nylund, and H. Pavia, 'Growth and biofouling in kelp aquaculture (Saccharina latissima): the effect of location and wave exposure', *J. Appl. Phycol.*, vol. 32, no. 5, pp. 3199–3209, Oct. 2020, doi: 10.1007/s10811-020-02201-5.

[10] L. Kregting, A. J. Blight, B. Elsäßer, and G. Savidge, 'The influence of water motion on the growth rate of the kelp Laminaria digitata', *J. Exp. Mar. Biol. Ecol.*, vol. 478, pp. 86–95, May 2016, doi: 10.1016/j.jembe.2016.02.006.

[11] T. Bekkby, E. Rinde, H. Gundersen, K. M. Norderhaug, J. K. Gitmark, and H. Christie, 'Length, strength and water flow: relative importance of wave and current exposure on morphology in kelp Laminaria hyperborea', *Mar. Ecol. Prog. Ser.*, vol. 506, pp. 61–70, Jun. 2014, doi: 10.3354/meps10778.

[12] M. T. Burrows, R. Harvey, and L. Robb, 'Wave exposure indices from digital coastlines and the prediction of rocky shore community structure', *Mar. Ecol. Prog. Ser.*, vol. 353, pp. 1–12, Jan. 2008, doi: 10.3354/meps07284.

[13] R. C. Focht and J. S. Shima, 'Acceleration loggers reveal fine-scale heterogeneity in wave exposure along an open coast', *Estuar. Coast. Shelf Sci.*, vol. 233, p. 106507, Feb. 2020, doi: 10.1016/j.ecss.2019.106507.

[14] T. P. Lyman, K. Elsmore, B. Gaylord, J. E. K. Byrnes, and L. P. Miller, 'Open Wave Height Logger: An open source pressure sensor data logger for wave measurement', *Limnol. Oceanogr. Methods*, vol. 18, no. 7, pp. 335–345, 2020, doi: https://doi.org/10.1002/lom3.10370.

[15] D. Kennedy, E. Cullen, R. McNulty, M. Gaffney, M. Walsh, and B. O'Flynn, 'Marine Inertial Measurement Units: Communication, Capabilities, and Challenges', *Mar. Technol. Soc. J.*, vol. 49, no. 3, pp. 56–63, May 2015, doi: 10.4031/MTSJ.49.3.12.

[16] D. Kennedy, M. Walsh, and B. O'Flynn, 'Low-cost inertial measurement of ocean waves', in *2014 IEEE Sensor Systems for a Changing Ocean (SSCO).*, Oct. 2014, pp. 1–2. doi: 10.1109/SSCO.2014.7000387.

[17] M. Lindegarth and L. Gamfeldt, 'Comparing Categorical and Continuous Ecological Analyses: Effects of "Wave Exposure" on Rocky Shores', *Ecology*, vol. 86, no. 5, pp. 1346–1357, 2005, doi: https://doi.org/10.1890/04-1168.

[18] E. B. Thorstad, A. H. Rikardsen, A. Alp, and F. Økland, 'The Use of Electronic Tags in Fish Research – An Overview of Fish Telemetry Methods', *Turk. J. Fish. Aquat. Sci.*, vol. 13, no. 5, pp. 881--896, 2013.

[19] S. J. Cooke, S. G. Hinch, M. C. Lucas, and M. Lutcavage, 'Biotelemetry and Biologging', in *Fisheries Techniques*, 3rd edition., American Fisheries Society, 2012, pp. 819–860.

[20] W. J. Gibbons and K. M. Andrews, 'PIT Tagging: Simple Technology at Its Best', *BioScience*, vol. 54, no. 5, Art. no. 5, May 2004, doi: 10.1641/0006-3568(2004)054[0447:PTSTAI]2.0.CO;2.

[21] C. L. Stevens, C. L. Hurd, and M. J. Smith, 'Field measurement of the dynamics of the bull kelp Durvillaea antarctica (Chamisso) Heriot', *J. Exp. Mar. Biol. Ecol.*, vol. 269, no. 2, pp. 147–171, Mar. 2002, doi: 10.1016/S0022-0981(02)00007-2.

[22] J. C. Mullarney and C. A. Pilditch, 'The differential response of kelp to swell and infragravity wave motion', *Limnol. Oceanogr.*, vol. 62, no. 6, pp. 2524–2537, 2017, doi: https://doi.org/10.1002/lno.10587.

[23] R. Wilson, P. Reuter, and M. Wahl, 'Muscling in on mussels: new insights into bivalve behaviour using vertebrate remote-sensing technology', *Mar. Biol.*, vol. 147, no. 5, pp. 1165–1172, Sep. 2005, doi: 10.1007/s00227-005-0021-6.

[24] X. Che, I. Wells, G. Dickers, P. Kear, and X. Gong, 'Re-evaluation of RF electromagnetic communication in underwater sensor networks', *IEEE Commun. Mag.*, vol. 48, no. 12, Art. no. 12, Dec. 2010, doi: 10.1109/MCOM.2010.5673085.

[25] C. M. G. Gussen, P. S. R. Diniz, M. L. R. Campos, W. A. Martins, F. M. Costa, and J. N. Gois, 'A Survey of Underwater Wireless Communication Technologies', *J. Commun. Inf. Syst.*, vol. 31, no. 1, pp. 242–255, 2016, doi: 10.14209/jcis.2016.22.

[26] L. Lambo, Z. Shengli, and C. Jun-Hong, 'Prospects and problems of wireless communication for underwater sensor networks', *Wirel. Commun. Mob. Comput.*, vol. 8, no. 8, Art. no. 8, Oct. 2008, doi: 10.1002/wcm.654.

[27] M. C. Domingo, 'An overview of the internet of underwater things', *J. Netw. Comput. Appl.*, vol. 35, no. 6, Art. no. 6, Nov. 2012, doi: 10.1016/j.jnca.2012.07.012.

[28] I. F. Akyildiz, D. Pompili, and T. Melodia, 'Underwater acoustic sensor networks: research challenges', *Ad Hoc Netw.*, vol. 3, no. 3, pp. 257–279, May 2005, doi: 10.1016/j.adhoc.2005.01.004.

[29] G. Benelli and A. Pozzebo, 'RFID Under Water: Technical Issues and Applications', in *Radio Frequency Identification from System to Applications*, M. I. B. Reaz, Ed. InTech, 2013. doi: 10.5772/53934.

[30] 'Biomark PIT Tag Antennas', *Biomark - Specialists in Identification Solutions*. https://www.biomark.com/pit-tag-antennas/ (accessed Jun. 02, 2021).

[31] E. B. Thorstad, A. H. Rikardsen, A. Alp, and F. Økland, 'The Use of Electronic Tags in Fish Research – An Overview of Fish Telemetry Methods', *Turk. J. Fish. Aquat. Sci.*, vol. 13, no. 5, Art. no. 5, 2013.

[32] E. L. C. Shepard *et al.*, 'Derivation of body motion via appropriate smoothing of acceleration data', *Aquat. Biol.*, vol. 4, no. 3, Art. no. 3, Dec. 2008, doi: 10.3354/ab00104.

[33] L. R. Brewster *et al.*, 'Development and application of a machine learning algorithm for classification of elasmobranch behaviour from accelerometry data', *Mar. Biol.*, vol. 165, no. 4, Art. no. 4, Mar. 2018, doi: 10.1007/s00227-018-3318-y.

[34] M. Mohammadi, A. Al-Fuqaha, S. Sorour, and M. Guizani, 'Deep Learning for IoT Big Data and Streaming Analytics: A Survey', *IEEE Commun. Surv. Tutor.*, vol. 20, no. 4, Art. no. 4, Fourthquarter 2018, doi: 10.1109/COMST.2018.2844341.

[35] F. Broell, 'Accelerometry: the key to measuring size-at-age and activity in fish', Thesis, 2016. Accessed: Sep. 21, 2018. [Online]. Available: https://DalSpace.library.dal.ca/xmlui/handle/10222/70838

[36] D. D. Brown, R. Kays, M. Wikelski, R. Wilson, and A. P. Klimley, 'Observing the unwatchable through acceleration logging of animal behavior', *Anim. Biotelemetry*, vol. 1, no. 1, Art. no. 1, Dec. 2013, doi: 10.1186/2050-3385-1-20.

[37] R. Nathan, O. Spiegel, S. Fortmann-Roe, R. Harel, M. Wikelski, and W. M. Getz, 'Using tri-axial acceleration data to identify behavioral modes of free-ranging animals: general concepts and tools illustrated for griffon vultures', *J. Exp. Biol.*, vol. 215, no. 6, Art. no. 6, Mar. 2012, doi: 10.1242/jeb.058602.

[38] E. L. C. Shepard *et al.*, 'Identification of animal movement patterns using tri-axial accelerometry', *Endanger. Species Res.*, vol. 10, pp. 47–60, Mar. 2008, doi: 10.3354/esr00084.

[39] *FAO Yearbook. Fishery and Aquaculture Statistics 2018/FAO annuaire. Statistiques des pêches et de l'aquaculture 2018/FAO anuario. Estadísticas de pesca y acuicultura 2018*. FAO, 2020. doi: 10.4060/cb1213t.

[40] T. Chopin and A. G. J. Tacon, 'Importance of Seaweeds and Extractive Species in Global Aquaculture Production', *Rev. Fish. Sci. Aquac.*, vol. 0, no. 0, pp. 1–10, Sep. 2020, doi: 10.1080/23308249.2020.1810626.

[41] M. Føre *et al.*, 'Precision fish farming: A new framework to improve production in aquaculture', *Biosyst. Eng.*, vol. 173, pp. 176–193, Sep. 2018, doi: 10.1016/j.biosystemseng.2017.10.014.

[42] J. Fang, J. Zhang, T. Xiao, D. Huang, and S. Liu, 'Integrated multi-trophic aquaculture (IMTA) in Sanggou Bay, China', *Aquac. Environ. Interact.*, vol. 8, pp. 201–205, Apr. 2016, doi: 10.3354/aei00179.

[43] 'IMPAQT Project'. https://impaqtproject.eu/about-impaqt/ (accessed Sep. 01, 2020).

[44] 'Can integrated multi-trophic aquaculture (IMTA) make an IMPAQT in Europe?' https://thefishsite.com/articles/can-integrated-multi-trophic-aquaculture-imta-make-an-impaqt-in-europe (accessed Sep. 10, 2020).

[45] F. O'Donncha and J. Grant, 'Precision Aquaculture', *IEEE Internet Things Mag.*, vol. 2, no. 4, pp. 26–30, Dec. 2019, doi: 10.1109/IOTM.0001.1900033.

[46] B. M. Roque, J. K. Salwen, R. Kinley, and E. Kebreab, 'Inclusion of Asparagopsis armata in lactating dairy cows' diet reduces enteric methane emission by over 50 percent', *J. Clean. Prod.*, vol. 234, pp. 132–138, Oct. 2019, doi: 10.1016/j.jclepro.2019.06.193.

[47] C. M. Duarte, J. Wu, X. Xiao, A. Bruhn, and D. Krause-Jensen, 'Can Seaweed Farming Play a Role in Climate Change Mitigation and Adaptation?', *Front. Mar. Sci.*, vol. 4, 2017, doi: 10.3389/fmars.2017.00100.

[48] M. Mac Monagail and L. Morrison, 'The seaweed resources of Ireland: a twenty-first century perspective', *J. Appl. Phycol.*, pp. 1–14, 2020.

[49] BIM, 'The Business of Seafood 2020', Ireland Seafood Development Agency, Mar. 2021.

[50] J. K. Kim *et al.*, 'Seaweed aquaculture: cultivation technologies, challenges and its ecosystem services', *ALGAE*, vol. 32, no. 1, pp. 1–13, Mar. 2017, doi: 10.4490/algae.2017.32.3.3.

[51] P. D. Kerrison, M. S. Stanley, M. D. Edwards, K. D. Black, and A. D. Hughes, 'The cultivation of European kelp for bioenergy: Site and species selection', *Biomass Bioenergy*, vol. 80, pp. 229–242, Sep. 2015, doi: 10.1016/j.biombioe.2015.04.035.

[52] A. Bruhn *et al.*, 'Impact of environmental conditions on biomass yield, quality, and bio-mitigation capacity of Saccharina latissima', *Aquac. Environ. Interact.*, vol. 8, pp. 619–636, Nov. 2016, doi: 10.3354/aei00200.

[53] O. J. Broch and D. Slagstad, 'Modelling seasonal growth and composition of the kelp Saccharina latissima', *J. Appl. Phycol.*, vol. 24, no. 4, pp. 759–776, Aug. 2012, doi: 10.1007/s10811-011-9695-y.

[54] A. B. Dauda, A. Ajadi, A. S. Tola-Fabunmi, and A. O. Akinwole, 'Waste production in aquaculture: Sources, components and managements in different culture systems', *Aquac. Fish.*, vol. 4, no. 3, pp. 81–88, May 2019, doi: 10.1016/j.aaf.2018.10.002.

[55] A. Neori *et al.*, 'Integrated aquaculture: rationale, evolution and state of the art emphasizing seaweed biofiltration in modern mariculture', *Aquaculture*, vol. 231, no. 1, pp. 361–391, Mar. 2004, doi: 10.1016/j.aquaculture.2003.11.015.

[56] G. K. Reid *et al.*, 'Performance measures and models for open-water integrated multi-trophic aquaculture', *Rev. Aquac.*, vol. 12, no. 1, pp. 47–75, 2020, doi: https://doi.org/10.1111/raq.12304.

[57] J. T. O. Kirk, *Light and Photosynthesis in Aquatic Ecosystems*. Cambridge University Press, 1994.

[58] M. Ottinger, K. Clauss, and C. Kuenzer, 'Aquaculture: Relevance, distribution, impacts and spatial assessments – A review', *Ocean Coast. Manag.*, vol. 119, pp. 244–266, Jan. 2016, doi: 10.1016/j.ocecoaman.2015.10.015.

[59] C. Meneghesso *et al.*, 'Remotely-sensed L4 SST underestimates the thermal fingerprint of coastal upwelling', *Remote Sens. Environ.*, vol. 237, p. 111588, Feb. 2020, doi: 10.1016/j.rse.2019.111588.

[60] H.-J. Woo and K.-A. Park, 'Inter-Comparisons of Daily Sea Surface Temperatures and In-Situ Temperatures in the Coastal Regions', *Remote Sens.*, vol. 12, no. 10, Art. no. 10, Jan. 2020, doi: 10.3390/rs12101592.

[61] R. J. W. Brewin *et al.*, 'Evaluating Operational AVHRR Sea Surface Temperature Data at the Coastline Using Benthic Temperature Loggers', *Remote Sens.*, vol. 10, no. 6, Art. no. 6, Jun. 2018, doi: 10.3390/rs10060925.

[62] 'LI-COR Biosciences - Impacting Lives Through Science'. https://www.licor.com/env/products/light/quantum_underwater (accessed Jun. 02, 2021).

[63] 'HOBO Pendant Temperature/Light Data Logger 64K'. https://www.onsetcomp.com/products/data-loggers/ua-002-64 (accessed Jun. 17, 2021).

[64] R. Judge, F. Choi, and B. Helmuth, 'Recent Advances in Data Logging for Intertidal Ecology', *Front. Ecol. Evol.*, vol. 6, 2018, doi: 10.3389/fevo.2018.00213.

[65] 'iButton - iButton Devices - One Wire | Maxim Integrated'. https://www.maximintegrated.com/en/products/ibutton-one-wire/ibutton.html (accessed Jun. 22, 2021).

[66] 'TidbiT v2 Temperature Data Logger - UTBI-001'. https://www.onsetcomp.com/products/data-loggers/utbi-001 (accessed Jun. 22, 2021).

[67] P. Knight, C. Bird, A. Sinclair, J. Higham, and A. Plater, 'Testing an "IoT" Tide Gauge Network for Coastal Monitoring', *IoT*, vol. 2, no. 1, Art. no. 1, Mar. 2021, doi: 10.3390/iot2010002.

[68] P. A. Beddows and E. K. Mallon, 'Cave Pearl Data Logger: A Flexible Arduino-Based Logging Platform for Long-Term Monitoring in Harsh Environments', *Sensors*, vol. 18, no. 2, Art. no. 2, Feb. 2018, doi: 10.3390/s18020530.

[69] M. L. Boller and E. Carrington, 'In situ measurements of hydrodynamic forces imposed on Chondrus crispus Stackhouse', *J. Exp. Mar. Biol. Ecol.*, vol. 337, no. 2, pp. 159–170, Oct. 2006, doi: 10.1016/j.jembe.2006.06.011.

[70] 'Datawell > Buoys'. https://www.datawell.nl/Products/Buoys.aspx (accessed Mar. 06, 2021).

[71] X. Che, I. Wells, G. Dickers, P. Kear, and X. Gong, 'Re-evaluation of RF electromagnetic communication in underwater sensor networks', *IEEE Commun. Mag.*, vol. 48, no. 12, pp. 143–151, Dec. 2010, doi: 10.1109/MCOM.2010.5673085.

[72] M. C. Domingo, 'Magnetic Induction for Underwater Wireless Communication Networks', *IEEE Trans. Antennas Propag.*, vol. 60, no. 6, Art. no. 6, Jun. 2012, doi: 10.1109/TAP.2012.2194670.

[73] K. Finkenzeller, *RFID Handbook: fundamentals and applications in contactless smart cards, radio frequency identification and near-field communication*. Hoboken, N.J.: Wiley, 2014.

[74] J. Heidemann, Wei Ye, J. Wills, A. Syed, and Yuan Li, 'Research challenges and applications for underwater sensor networking', in *IEEE Wireless Communications and Networking Conference, 2006. WCNC 2006.*, Las Vegas, NV, USA, 2006, pp. 228–235. doi: 10.1109/WCNC.2006.1683469.

[75] Y. Li, S. Wang, C. Jin, Y. Zhang, and T. Jiang, 'A Survey of Underwater Magnetic Induction Communications: Fundamental Issues, Recent Advances, and Challenges', *IEEE Commun. Surv. Tutor.*, vol. 21, no. 3, Art. no. 3, thirdquarter 2019, doi: 10.1109/COMST.2019.2897610.

[76] A. Pozzebon, 'Bringing near field communication under water: short range data exchange in fresh and salt water', in *2015 International EURASIP Workshop on RFID Technology (EURFID)*, Oct. 2015, pp. 152–156. doi: 10.1109/EURFID.2015.7332401.

[77] D. Bertoni, G. Sarti, G. Benelli, A. Pozzebon, and G. Raguseo, 'Radio Frequency Identification (RFID) technology applied to the definition of underwater and subaerial coarse sediment movement', *Sediment. Geol.*, vol. 228, no. 3, Art. no. 3, Jul. 2010, doi: 10.1016/j.sedgeo.2010.04.007.

[78] I. F. Akyildiz, P. Wang, and Z. Sun, 'Realizing underwater communication through magnetic induction', *IEEE Commun. Mag.*, vol. 53, no. 11, pp. 42–48, Nov. 2015, doi: 10.1109/MCOM.2015.7321970.

[79] B. Gulbahar and O. B. Akan, 'A Communication Theoretical Modeling and Analysis of Underwater Magneto-Inductive Wireless Channels', *IEEE Trans. Wirel. Commun.*, vol. 11, no. 9, pp. 3326–3334, Sep. 2012, doi: 10.1109/TWC.2012.070912.111943.

[80] Z. Sun and I. F. Akyildiz, 'Magnetic Induction Communications for Wireless Underground Sensor Networks', *IEEE Trans. Antennas Propag.*, vol. 58, no. 7, pp. 2426–2435, Jul. 2010, doi: 10.1109/TAP.2010.2048858.

[81] U. Azad, H. C. Jing, and Y. E. Wang, 'Link Budget and Capacity Performance of Inductively Coupled Resonant Loops', *IEEE Trans. Antennas Propag.*, vol. 60, no. 5, pp. 2453–2461, May 2012, doi: 10.1109/TAP.2012.2189696.

[82] H. Nguyen, J. I. Agbinya, and J. Devlin, 'Channel Characterisation and Link Budget of MIMO Configuration in Near Field Magnetic Communication', *Int. J. Electron. Telecommun.*, vol. 59, no. 3, pp. 255–262, Sep. 2013, doi: 10.2478/eletel-2013-0030.

[83] D. R. Gawade *et al.*, 'A battery-less NFC sensor transponder for museum artefact monitoring - a review of NFC sensor technology and a proposed solution', in *SENSORCOM 2019*, Nice, France, Oct. 2019, pp. 89–96. Accessed: Sep. 01, 2020. [Online]. Available: https://cora.ucc.ie/handle/10468/9634

[84] 'ISO/IEC 18000-2:2009 Information technology — Radio frequency identification for item management — Part 2: Parameters for air interface communications below 135 kHz'. [Online]. Available: https://www.iso.org/standard/46146.html

[85] 'ISO/IEC 18000-3:2010 Information technology — Radio frequency identification for item management — Part 3: Parameters for air interface communications at 13.56 MHz'. [Online]. Available: https://www.iso.org/standard/53424.html

[86] 'ISO/IEC 15693-1:2010 Identification cards — Contactless integrated circuit cards — Vicinity cards — Part 1: Physical characteristics'. [Online]. Available: https://www.iso.org/standard/39694.html

[87] 'ISO/IEC 14443-1:2018 Cards and security devices for personal identification — Contactless proximity objects — Part 1: Physical characteristics'. [Online]. Available: https://www.iso.org/standard/73596.html

[88] NFC Forum, 'NFC Forum Tag Type Technical Specifications'. [Online]. Available: http://www.nfc-forum.org/specs/spec-list/#tagtypes

[89] E. C. M. Association, *ECMA340–Near Field Communication Interface and Protocol (NFCIP-1)*. Genf, 2004.

[90] P. Haigh, M. Hayes, D. R. Gawade, and B. O'Flynn, 'Towards autonomous smart sensing systems', in *2020 IEEE International Instrumentation and Measurement Technology Conference (I2MTC)*, 2020, pp. 1–6.

[91] Texas Instrument, 'Antenna Design Guide for the TRF79xxA'. Accessed: Aug. 01, 2020. [Online]. Available: http://www.ti.com/lit/an/sloa241b/sloa241b.pdf

[92] C. A. Balanis, *Advanced engineering electromagnetics*, 2nd ed. Hoboken, N.J: John Wiley & Sons, 2012.

[93] E. E. Kriezis, T. D. Tsiboukis, S. M. Panas, and J. A. Tegopoulos, 'Eddy currents: theory and applications', *Proc. IEEE*, vol. 80, no. 10, pp. 1559–1589, Oct. 1992, doi: 10.1109/5.168666.

[94] P. Fofanoff and R. C. Millard Jr, 'UNESCO, Algorithms for computation of fundamental properties of seawater, UNSESCO Tech. Pap', *Mar. Sci.*, no. 44, p. 55.

[95] R. Somaraju and J. Trumpf, 'Frequency, Temperature and Salinity Variation of the Permittivity of Seawater', *IEEE Trans. Antennas Propag.*, vol. 54, no. 11, Art. no. 11, Nov. 2006, doi: 10.1109/TAP.2006.884290.

[96] P. J. W. Debye, *Polar molecules*. Chemical Catalog Company, Incorporated, 1929.

[97] D. R. Lide, 'Handbook of Chemistry and Physics, CRC Press', *Boca Raton FL*, vol. 1, no. 993, p. 1, 1993.

[98] J. B. Hasted, S. K. Husain, F. A. M. Frescura, and J. R. Birch, 'The temperature variation of the near millimetre wavelength optical constants of water', *Infrared Phys.*, vol. 27, no. 1, pp. 11–15, 1987.

[99] A. P. Stogryn, H. T. Bull, K. Rubayi, and S. Iravanchy, 'The microwave permittivity of sea and fresh water', *GenCorp Aeroj. Azusa CA*, 1995.

[100] D. G. Archer and P. Wang, 'The dielectric constant of water and Debye-Hückel limiting law slopes', *J. Phys. Chem. Ref. Data*, vol. 19, no. 2, pp. 371–411, 1990.

[101] H. J. Liebe, G. A. Hufford, and T. Manabe, 'A model for the complex permittivity of water at frequencies below 1 THz', *Int. J. Infrared Millim. Waves*, vol. 12, no. 7, pp. 659–675, 1991.

[102] T. Meissner and F. J. Wentz, 'The complex dielectric constant of pure and sea water from microwave satellite observations', *IEEE Trans. Geosci. Remote Sens.*, vol. 42, no. 9, pp. 1836–1849, 2004.

[103] L. Klein and C. Swift, 'An improved model for the dielectric constant of sea water at microwave frequencies', *IEEE Trans. Antennas Propag.*, vol. 25, no. 1, pp. 104–111, 1977.

[104] A. Stogryn, 'Equations for calculating the dielectric constant of saline water (correspondence)', *IEEE Trans. Microw. Theory Tech.*, vol. 19, no. 8, pp. 733–736, 1971.

[105] 'Recommendation ITU-R P.527-5'. International Telecommunication Union, 2019. Accessed: Aug. 01, 2020. [Online]. Available: https://www.itu.int/rec/R-REC-P.527-5-201908-I/en

[106] C. Uribe and W. Grote, 'Radio Communication Model for Underwater WSN', in *2009 3rd International Conference on New Technologies, Mobility and Security*, Dec. 2009, pp. 1–5. doi: 10.1109/NTMS.2009.5384789.

[107] C. A. Balanis, *Antenna theory: analysis and design*, 3rd ed. Hoboken, NJ: John Wiley, 2005.
[108] H. Lehpamer, *RFID design principles*, 2nd ed. Boston: Artech House, 2012.
[109] H. Guo, Z. Sun, and P. Wang, 'Channel Modeling of MI Underwater Communication Using Tri-Directional Coil Antenna', in *2015 IEEE Global Communications Conference (GLOBECOM)*, Dec. 2015, pp. 1–6. doi: 10.1109/GLOCOM.2015.7417399.
[110] Z. Sun, I. F. Akyildiz, S. Kisseleff, and W. Gerstacker, 'Increasing the Capacity of Magnetic Induction Communications in RF-Challenged Environments', *IEEE Trans. Commun.*, vol. 61, no. 9, pp. 3943–3952, Sep. 2013, doi: 10.1109/TCOMM.2013.071813.120600.
[111] R. Want, 'RFID Explained: A Primer on Radio Frequency Identification Technologies', *Synth. Lect. Mob. Pervasive Comput.*, vol. 1, no. 1, Art. no. 1, Jan. 2006, doi: 10.2200/S00040ED1V01200607MPC001.
[112] K. V. S. Rao and P. V. Nikitin, 'Theory and measurement of backscattering from RFID tags', *IEEE Antennas Propag. Mag.*, vol. 48, no. 6, pp. 212–218, Dec. 2006, doi: 10.1109/MAP.2006.323323.
[113] 'VNA master MS20xxC technical data sheet', manual, Aug. 2019.
[114] '100 Series EMC Probes - Datasheet', Beehive Electronics, 100C, 2005.
[115] 'HDX RFID Reader System – Microreader RI-STU-MRD2', manual SCBU049, Aug. 2012.
[116] 'Pepper C1 user manual', manual SKU000395, Sep. 2019.
[117] G. D. Durgin, 'ECE 3065 notes', TESSAL - Georgia Institute of Technology, manual.
[118] R. G. Wetzel, *Limnology: Lake and River Ecosystems*. Gulf Professional Publishing, 2001.
[119] 'Salinity', *Wikipedia*. Jun. 11, 2021. Accessed: Jul. 04, 2021. [Online]. Available: https://en.wikipedia.org/w/index.php?title=Salinity&oldid=1028075446
[120] A. Shaw, A. I. Al-Shamma'a, S. R. Wylie, and D. Toal, 'Experimental investigations of electromagnetic wave propagation in seawater', in *2006 european microwave conference*, 2006, pp. 572–575.
[121] 'TMS37157 Datasheet', Texas Instruments, Nov. 2009.
[122] 'An interview to discover IMTA´ Site in Ireland: Lehanagh Pool – IMPAQT'. https://impaqtproject.eu/an-interview-to-discover-imta-site-in-ireland-lehanagh-pool/ (accessed Jul. 04, 2021).
[123] K. Aslanidis and A. Frantzke, 'TMS37157 Passive Low-Frequency Interface IC Performance With Neosid Antennas', Texas Instruments, SWRA382A, Apr. 2013.
[124] 'Neosid', *Neosid*. https://neosid.de/en/ (accessed Jun. 02, 2021).
[125] 'STM32 Arm Cortex MCUs - 32-bit Microcontrollers - STMicroelectronics'. https://www.st.com/en/microcontrollers-microprocessors/stm32-32-bit-arm-cortex-mcus.html (accessed Jul. 04, 2021).
[126] 'Biomark PIT Tags', *Biomark - Specialists in Identification Solutions*. https://www.biomark.com/pit-tags/ (accessed Jun. 02, 2021).
[127] 'Animal Heart Rate Activity Data Logger'. https://www.star-oddi.com/products/archival-tags/animal-heart-rate-activity-logger (accessed Sep. 20, 2021).
[128] 'MCFT3 VHF Radio Transmitter Series | LotekLotek', *Lotek |*, Oct. 26, 2017. https://www.lotek.com/products/mcft3-series/ (accessed Sep. 20, 2021).
[129] 'BQ25100 datasheet | TI.com'. Accessed: May 27, 2021. [Online]. Available: https://www.ti.com/document-viewer/BQ25100/datasheet
[130] 'TPS7A02 datasheet | TI.com'. Accessed: May 27, 2021. [Online]. Available: https://www.ti.com/document-viewer/TPS7A02/datasheet
[131] 'LTC2955 Datasheet and Product Info | Analog Devices'. Accessed: May 27, 2021. [Online]. Available: https://www.analog.com/en/products/ltc2955.html#

[132] 'LSM6DSOX - iNEMO inertial module with Machine Learning Core, Finite State Machine and advanced Digital Functions. Ultra-low power for battery operated IoT, Gaming, Wearable and Personal Electronics. - STMicroelectronics'. Accessed: May 27, 2021. [Online]. Available: https://www.st.com/en/mems-and-sensors/lsm6dsox.html

[133] '0-30 Bar Digital Pressure Sensor | MS5837'. Accessed: May 27, 2021. [Online]. Available: https://www.te.com/usa-en/product-CAT-BLPS0017.html

[134] 'Photosynthetically Active Radiation: Measurement and Modeling', in *SpringerReference*, Berlin/Heidelberg: Springer-Verlag, 2011. doi: 10.1007/SpringerReference_310766.

[135] 'TCS34725 Color Sensor – Color Light-To-Digital Converter | ams'. Accessed: May 27, 2021. [Online]. Available: https://ams.com/TCS34725

[136] J. Rajendran, W. D. Leon-Salas, X. Fan, Y. Zhang, M. A. Vizcardo, and M. Postigo, 'On the Development of a Low-Cost Photosynthetically Active Radiation (PAR) Sensor', in *2020 IEEE International Symposium on Circuits and Systems (ISCAS)*, Oct. 2020, pp. 1–5. doi: 10.1109/ISCAS45731.2020.9181220.

[137] 'STM32L4R5/S5 - STMicroelectronics'. Accessed: May 27, 2021. [Online]. Available: https://www.st.com/en/microcontrollers-microprocessors/stm32l4r5-s5.html

[138] 'EEMBC - CPU/MCU Performance Benchmark - CoreMark'. https://www.eembc.org/coremark/scores.php (accessed May 27, 2021).

[139] 'EEMBC - CPU/MCU Energy Benchmark - ULPMark'. https://www.eembc.org/ulpmark/ulp-cp/scores.php (accessed May 27, 2021).

[140] 'MT29F8G01ADAFD12-IT'. Accessed: May 27, 2021. [Online]. Available: https://www.micron.com/products/nand-flash/serial-nand/part-catalog/mt29f8g01adafd12-it

[141] 'TPS22901 data sheet, product information and support | TI.com'. Accessed: May 27, 2021. [Online]. Available: https://www.ti.com/product/TPS22901

[142] STMicroelectronics, 'ST25DV04K- Datasheet'. 2018. Accessed: Aug. 01, 2020. [Online]. Available: https://www.st.com/resource/en/datasheet/st25dv04k.pdf

[143] 'AYF530265T | Y5B/Y5BW(0.5mm pitch) | Automation Controls | Industrial Devices | Panasonic'. https://www3.panasonic.biz/ac/e/search_num/index.jsp?c=detail&part_no=AYF530265T&medium_g_cd=12&small_g_cd=123&series_cd=1316 (accessed Jun. 02, 2021).

[144] 'ECS Circuits LTD - Ireland's leading supplier of PCB | PCB Fabrication', *ECS Circuits LTD*. https://ecscircuits.ie/products/pcb-fabrication/ (accessed Jun. 02, 2021).

[145] R. A. Serway, *Principles of physics*. Fort Worth : Saunders College Pub., 1998. Accessed: Jul. 04, 2021. [Online]. Available: http://archive.org/details/principlesofphys00serw

[146] *NFC Antenna eDesignSuite - STMicroelectronics*. Accessed: May 27, 2021. [Online]. Available: https://eds.st.com/antenna/

[147] STMicroelectronics, 'AN2866 - How to design a 13.56 MHz customized antenna for ST25 NFC / RFID Tags'. Dec. 2020. [Online]. Available: https://www.st.com/resource/en/application_note/cd00221490-how-to-design-a-13-56-mhz-customized-antenna-for-st25-nfc-rfid-tags-stmicroelectronics.pdf

[148] 'Form 3: Industrial-Quality Desktop SLA 3D Printer', *Formlabs*. https://formlabs.com/3d-printers/form-3/ (accessed Jul. 22, 2021).

[149] Formlabs, 'FLDUCL02 - Durable Resin Technical Datasheet'. [Online]. Available: https://formlabs-media.formlabs.com/datasheets/1801084-TDS-ENUS-0P.pdf

[150] 'Universal Serial Bus 2.0 Specification', USB Implementers Forum, Apr. 2000. [Online]. Available: https://www.usb.org/documents

[151] 'STSW-ST25SDK001 - Software Development Kit for ST25 Tags and Dynamic Tags - STMicroelectronics'. https://www.st.com/en/embedded-software/stsw-st25sdk001.html (accessed May 31, 2021).

[152] 'PyUSB'. https://pyusb.github.io/pyusb/ (accessed May 31, 2021).
[153] 'UM1734 - STM32Cube™ USB device library user manual'. STMicroelectronics, Feb. 2019. [Online]. Available: https://www.st.com/resource/en/user_manual/dm00108129-stm32cube-usb-device-library-stmicroelectronics.pdf
[154] 'Prime^{x} 13 - Specs', *OptiTrack*. http://optitrack.com/cameras/primex-13/specs.html (accessed May 31, 2021).
[155] 'Motive - Optical motion capture software', *OptiTrack*. http://www.optitrack.com/software/motive/index.html (accessed May 20, 2021).
[156] 'Calibration - NaturalPoint Product Documentation Ver 2.2'. https://v22.wiki.optitrack.com/index.php?title=Calibration (accessed May 20, 2021).
[157] 'MATLAB - MathWorks'. https://www.mathworks.com/products/matlab.html (accessed May 31, 2021).
[158] A. Kim and M. F. Golnaraghi, 'Initial calibration of an inertial measurement unit using an optical position tracking system', in *PLANS 2004. Position Location and Navigation Symposium (IEEE Cat. No.04CH37556)*, Apr. 2004, pp. 96–101. doi: 10.1109/PLANS.2004.1308980.
[159] Y.-H. Kim and H.-D. Ha, 'Design of interface circuits with electrical battery models', *IEEE Trans. Ind. Electron.*, vol. 44, no. 1, pp. 81–86, Feb. 1997, doi: 10.1109/41.557502.
[160] Keysight Technologies, 'Emulate the Battery for More Realistic Mobile Device Test Results'. [Online]. Available: https://www.keysight.com/ie/en/assets/7018-07426/technical-overviews/5990-9651.pdf
[161] J. D. Figurski, D. Malone, J. R. Lacy, and M. Denny, 'An inexpensive instrument for measuring wave exposure and water velocity', *Limnol. Oceanogr. Methods*, vol. 9, no. 5, pp. 204–214, 2011, doi: 10.4319/lom.2011.9.204.
[162] H. Gundersen, E. Rinde, T. Bekkby, K. Hancke, J. K. Gitmark, and H. Christie, 'Variation in Population Structure and Standing Stocks of Kelp Along Multiple Environmental Gradients and Implications for Ecosystem Services', *Front. Mar. Sci.*, vol. 8, p. 578629, Apr. 2021, doi: 10.3389/fmars.2021.578629.
[163] 'Historical Data - Met Éireann - The Irish Meteorological Service'. https://www.met.ie/climate/available-data/historical-data (accessed Jul. 17, 2021).
[164] L. H. Holthuijsen, 'Waves in Oceanic and Coastal Waters', p. 405.
[165] C. T. Bishop and M. A. Donelan, 'Measuring waves with pressure transducers', *Coast. Eng.*, vol. 11, no. 4, pp. 309–328, Nov. 1987, doi: 10.1016/0378-3839(87)90031-7.
[166] L. C. Bender, N. L. Guinasso, J. N. Walpert, and S. D. Howden, 'A Comparison of Methods for Determining Significant Wave Heights—Applied to a 3-m Discus Buoy during Hurricane Katrina', *J. Atmospheric Ocean. Technol.*, vol. 27, no. 6, pp. 1012–1028, Jun. 2010, doi: 10.1175/2010JTECHO724.1.
[167] B. Friedland, 'Analysis Strapdown Navigation Using Quaternions', *IEEE Trans. Aerosp. Electron. Syst.*, vol. AES-14, no. 5, pp. 764–768, Sep. 1978, doi: 10.1109/TAES.1978.308627.

APPENDIX I - SCHEMATICS

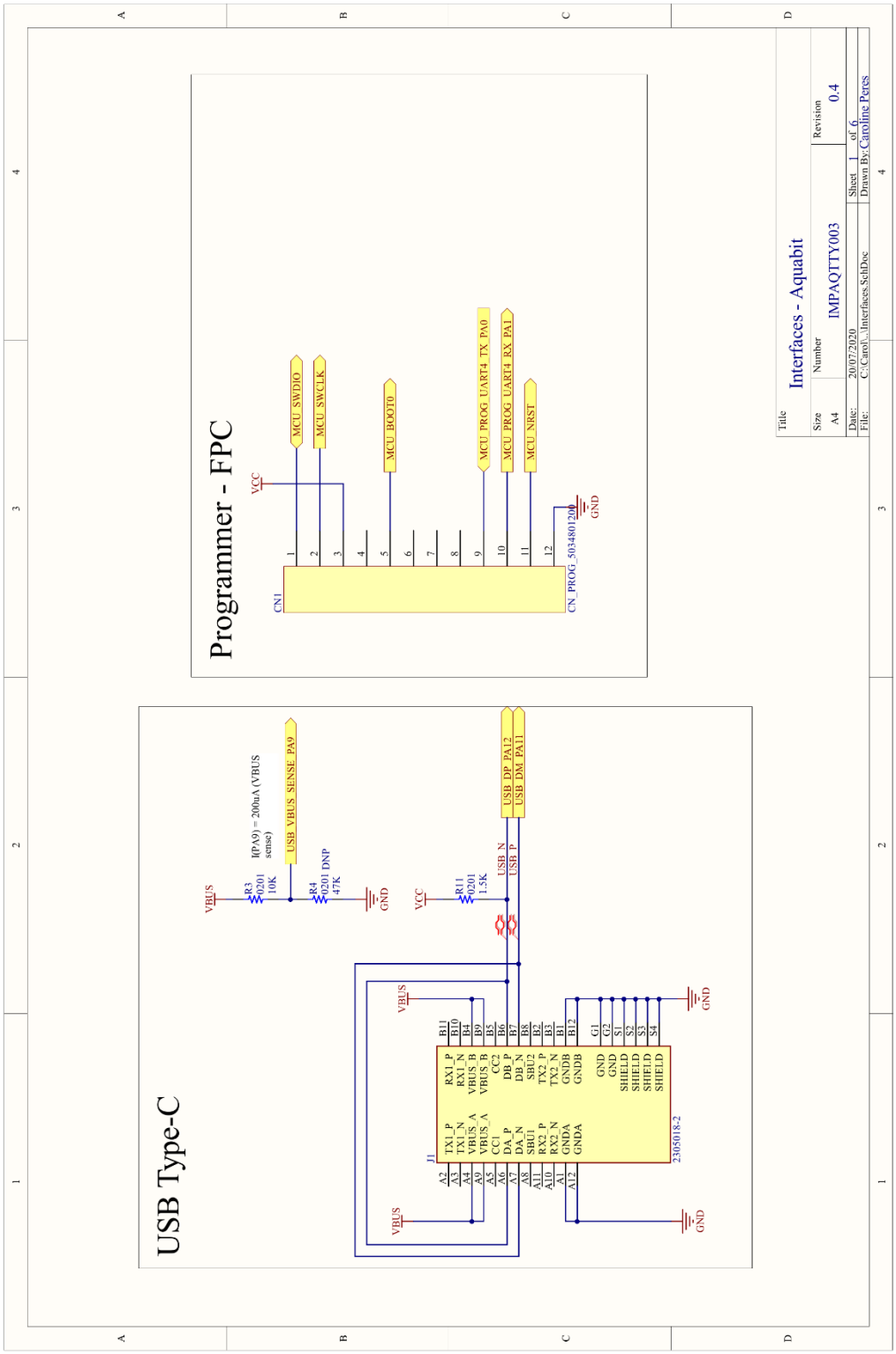

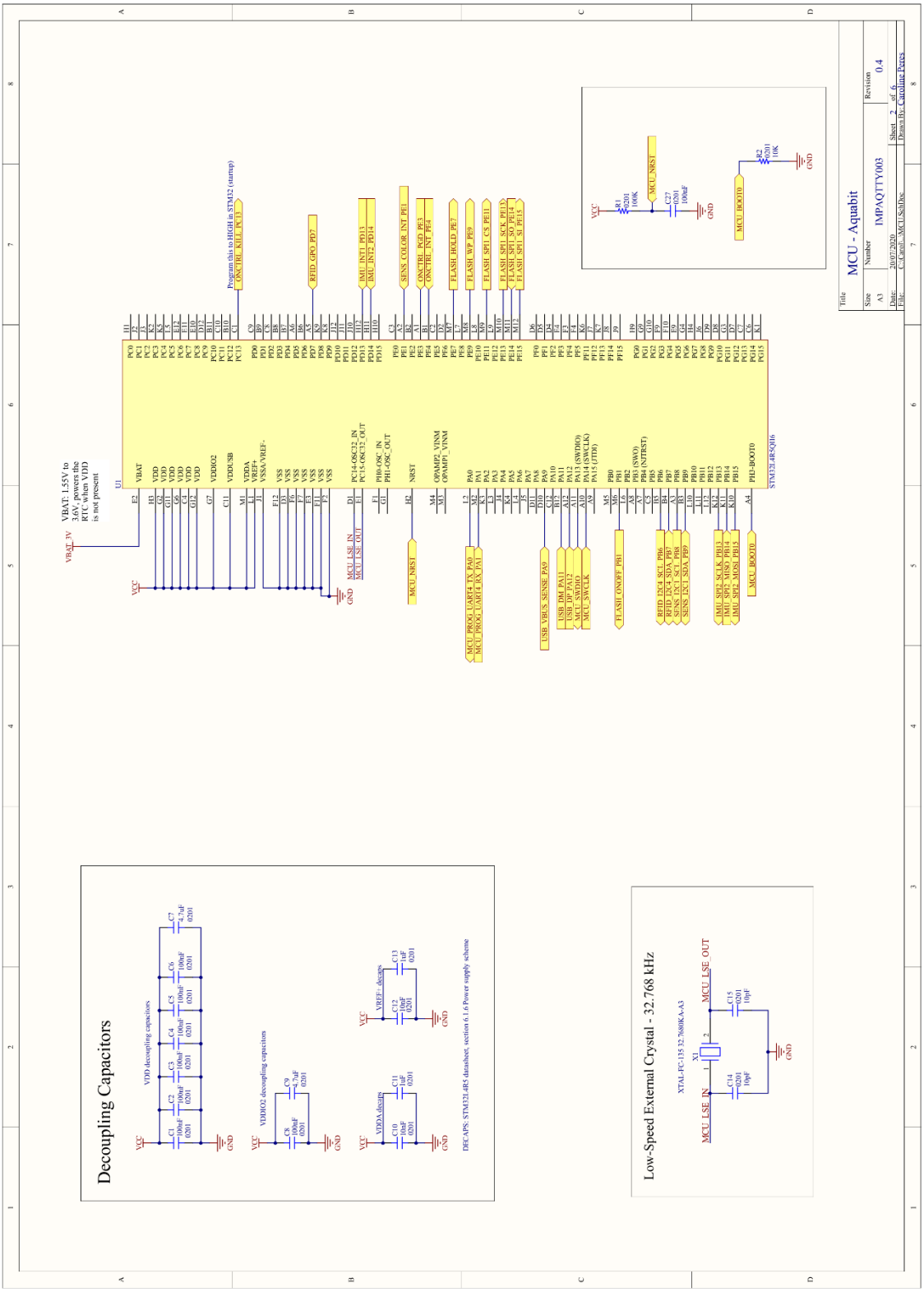
Decoupling Capacitors
VDD decoupling capacitors
VDDIO2 decoupling capacitors
VDDA decaps
VREF+ decaps
DECAPS: STM32L4R5 datasheet, section 6.1.6 Power supply scheme
Low-Speed External Crystal - 32.768 kHz
XTAL-FC-135 32.768KA-A3
MCU - Aquabit
IMPAQTTY003
Revision 0.4
Sheet 2 of 6
Drawn By: Caroline Peres
20/07/2020
STM32L4R5QI6
VBAT: 1.55V to 3.6V, powers the RTC when VDD is not present
Program this to HIGH in STM32 (startup)
RFID_GPO_PD7
IMU_INT1_PD13
IMU_INT2_PD14
SENS_COLOR_INT_PE1
ONCTRL_PGD_PE3
ONCTRL_INT_PE4
FLASH_HOLD_PE7
FLASH_WP_PE9
FLASH_SPI1_CS_PE11
FLASH_SPI1_SCK_PE13
FLASH_SPI1_SO_PE14
FLASH_SPI1_SI_PE15
MCU_NRST
MCU_BOOT0
MCU_LSE_IN
MCU_LSE_OUT
MCU_PROG_UART4_TX_PA0
MCU_PROG_UART4_RX_PA1
USB_VBUS_SENSE_PA9
USB_DM_PA11
USB_DP_PA12
MCU_SWDIO
MCU_SWCLK
FLASH_ONOFF_PB1
RFID_I2C4_SCL_PB6
RFID_I2C4_SDA_PB7
SENS_I2C1_SCL_PB8
SENS_I2C1_SDA_PB9
IMU_SPI2_SCLK_PB13
IMU_SPI2_MISO_PB14
IMU_SPI2_MOSI_PB15

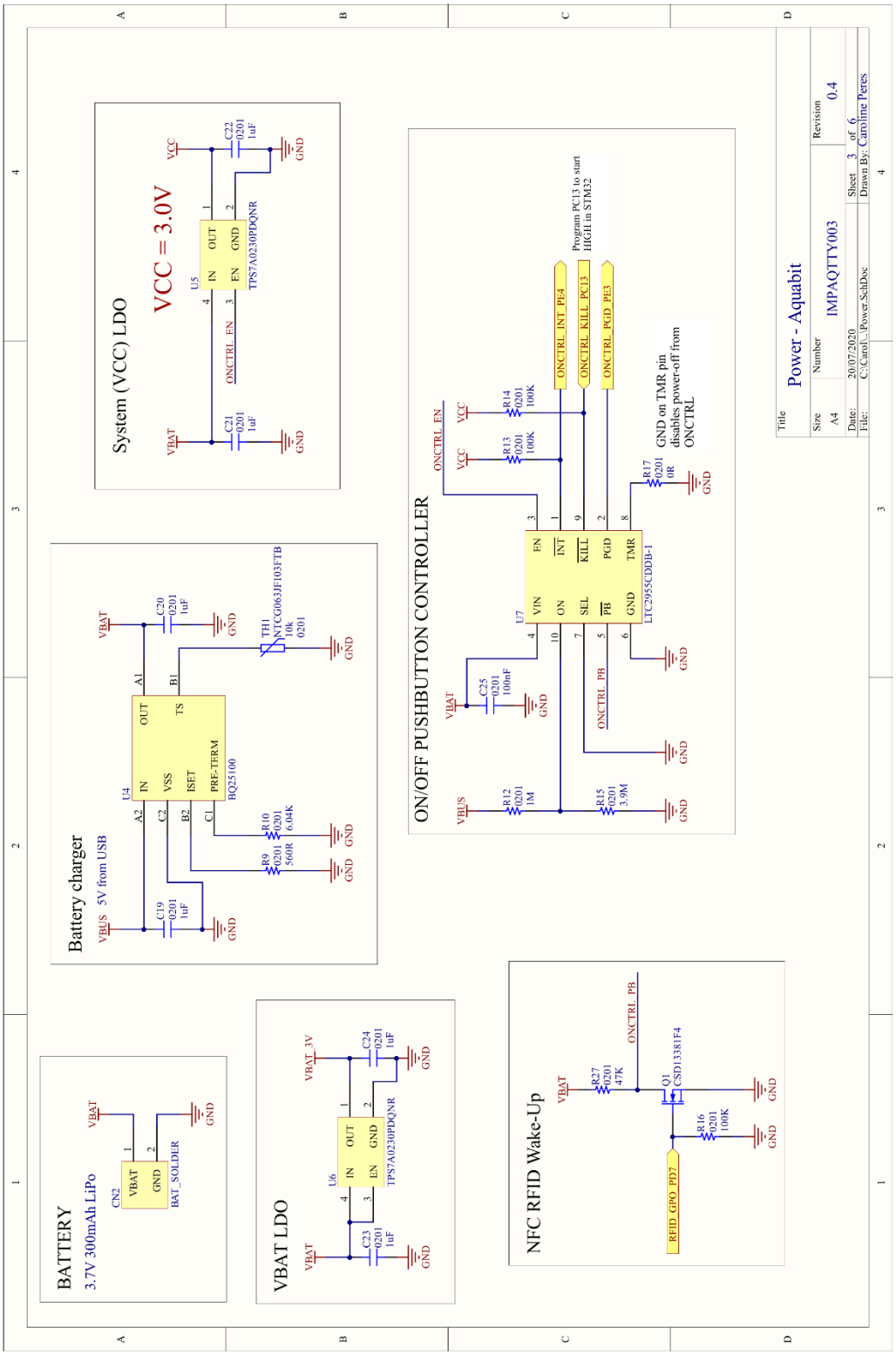
System (VCC) LDO
VCC = 3.0V
TPS7A0230PDQNR
Battery charger
5V from USB
BQ25100
ON/OFF PUSHBUTTON CONTROLLER
LTC2955CDDB-1
GND on TMR pin disables power-off from ONCTRL
Program PC13 to start HIGH in STM32
BATTERY
3.7V 300mAh LiPo
BAT_SOLDER
VBAT LDO
NFC RFID Wake-Up
CSD13381F4
Power - Aquabit
IMPAQTTY003
Revision 0.4
Sheet 3 of 6
Drawn By: Caroline Peres

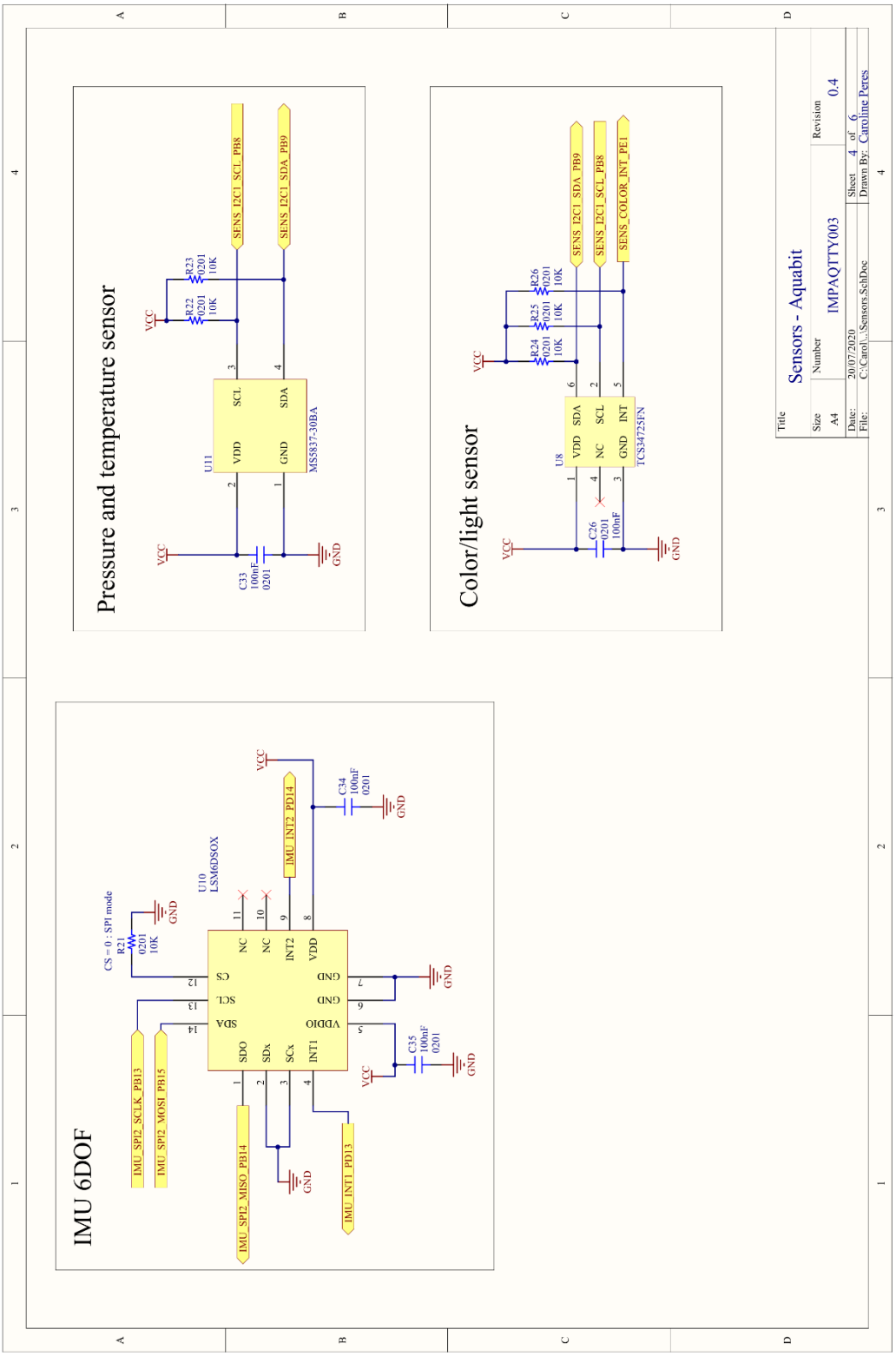
Pressure and temperature sensor
SENS_I2C1_SCL_PB8
SENS_I2C1_SDA_PB9
R23 0201 10K
R22 0201 10K
VCC
U11
SCL
SDA
VDD
GND
MS5837-30BA
C33 100nF 0201
GND
Color/light sensor
SENS_I2C1_SDA_PB9
SENS_I2C1_SCL_PB8
SENS_COLOR_INT_PE1
R26 0201 10K
R25 0201 10K
R24 0201 10K
U8
VDD
SDA
NC
SCL
GND
INT
TCS34725FN
C26 0201 100nF
IMU 6DOF
U10
LSM6DSOX
CS = 0 : SPI mode
R21 0201 10K
IMU_SPI2_SCLK_PB13
IMU_SPI2_MOSI_PB15
IMU_SPI2_MISO_PB14
IMU_INT2_PD14
IMU_INT1_PD13
C34 100nF 0201
C35 100nF 0201
NC
INT2
VDD
GND
VDDIO
INT1
SDO
SDx
SCx
CS
SCL
SDA
Title
Sensors - Aquabit
Size
A4
Number
IMPAQTTY003
Revision
0.4
Date:
20/07/2020
File:
C:\Carol\...\Sensors.SchDoc
Sheet 4 of 6
Drawn By: Caroline Peres

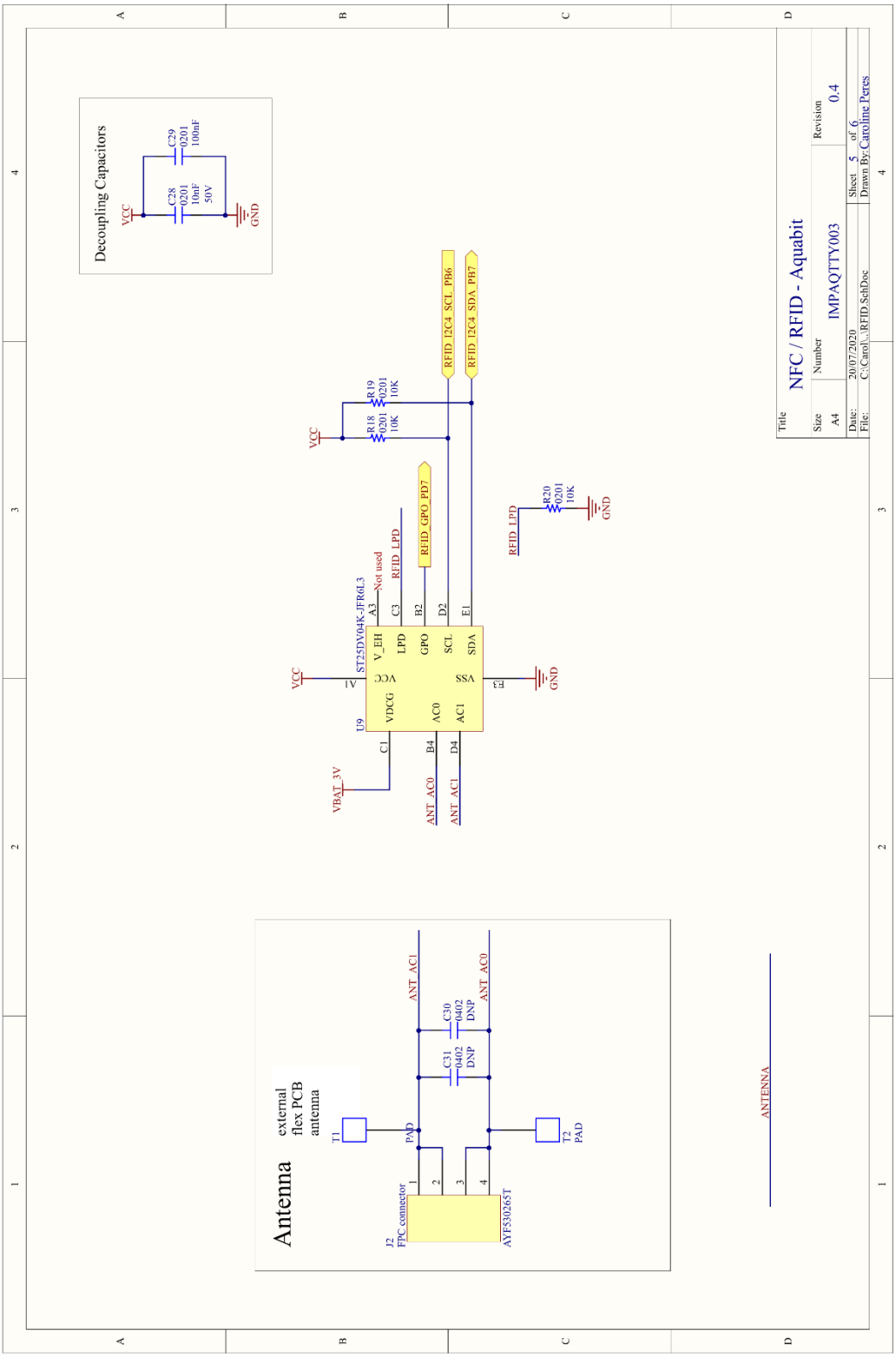
Decoupling Capacitors
C29 0201 100nF
C28 0201 10nF 50V
VCC
GND
Antenna
external flex PCB antenna
T1 PAD
T2 PAD
J2 FPC_connector
AYF530265T
C30 0402 DNP
C31 0402 DNP
ANT_AC1
ANT_AC0
ANTENNA
U9 ST25DV04K-JFR6J3
VCC
VSS
VDCG
V_EH
LPD
GPO
SCL
SDA
A3 Not used
C3 RFID_LPD
B2 RFID_GPO_PD7
D2 RFID_I2C4_SCL_PB6
E1 RFID_I2C4_SDA_PB7
C1 VBAT_3V
B4 ANT_AC0
D4 ANT_AC1
R18 0201 10K
R19 0201 10K
R20 0201 10K
RFID_LPD
Title NFC / RFID - Aquabit
Size A4
Number IMPAQTTY003
Revision 0.4
Date: 20/07/2020
File: C:\Caro\...\RFID.SchDoc
Sheet 5 of 6
Drawn By: Caroline Peres

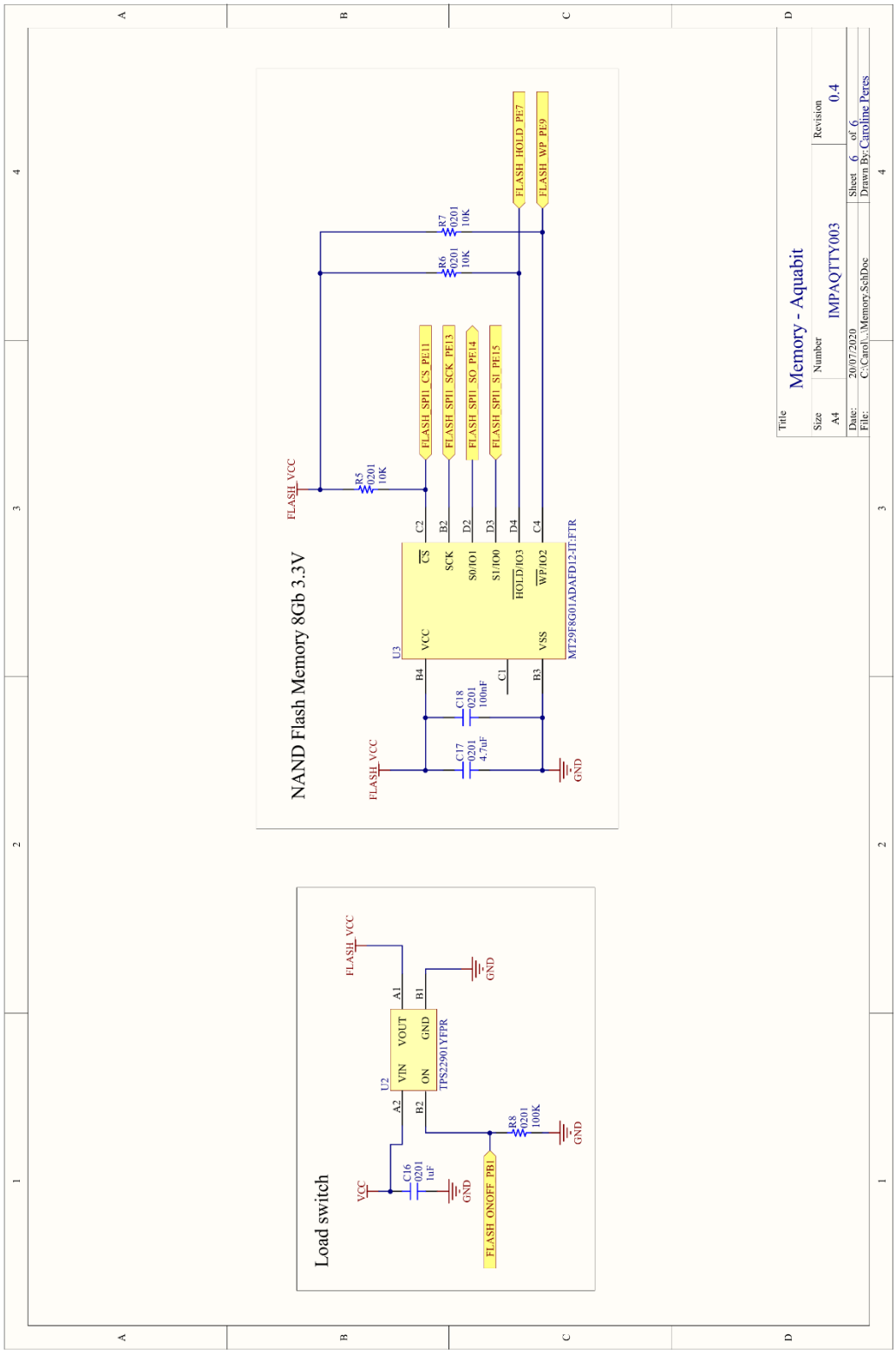
NAND Flash Memory 8Gb 3.3V
FLASH_VCC
R5 0201 10K
R6 0201 10K
R7 0201 10K
FLASH_SPI1_CS_PE11
FLASH_SPI1_SCK_PE13
FLASH_SPI1_SO_PE14
FLASH_SPI1_SI_PE15
FLASH_HOLD_PE7
FLASH_WP_PE9
U3
MT29F8G01ADAFD12-IT:FTR
C18 0201 100nF
C17 0201 4.7uF
C1
GND
Load switch
U2
TPS22901YFPR
VIN
VOUT
ON
GND
C16 0201 1uF
R8 0201 100K
FLASH_ONOFF_PB1
VCC
Title
Memory - Aquabit
Size
A4
Number
IMPAQTTY003
Revision
0.4
Date:
20/07/2020
Sheet 6 of 6
File:
C:\Carol\...\Memory.SchDoc
Drawn By: Caroline Peres